UNIVERSITY OF CALIFORNIA, SAN DIEGO

Computational Free-surface Fluid-structure Interaction with Applications on Offshore Wind and Tidal Energy

A Dissertation submitted in partial satisfaction of the
requirements for the degree
Doctor of Philosophy

in

Structural Engineering with a Specialization in Computational Science

by

Jinhui Yan

Committee in charge:

Professor Yuri Bazilevs, Chair
Professor David Benson
Professor Jiun-Shyan Chen
Professor Kenneth Loh
Professor Sutanu Sarkar

2016

The Dissertation of Jinhui Yan is approved, and it is acceptable in quality and form for publication on microfilm and electronically:

_____

_____

_____

_____

_____

Chair

University of California, San Diego

2016

DEDICATION

To Jingyi Li

EPIGRAPH

Stop thinking, and end your problems.

—Lao Tzu

TABLE OF CONTENTS

LIST OF FIGURES

LIST OF TABLES

ACKNOWLEDGEMENTS

First of all, I want to bring my deepest gratitude to my supervisor Professor Yuri Bazilevs and his research group. Yuri is a gracious, enthusiastic and illuminative mentor. He generously admitted me into UCSD and supervised my Ph.D. study with enormous patience, support and understanding. Yuri′s vast knowledge in mechanics, mathematics, numerical methods and research insights have inspired the entire path of my research. When I look back to my Ph.D. study, there are so many examples which can prove what an excellent advisor Yuri has been that I can't list all of them due to the limited space. In one word, my supervisor is my academic role model and sets the target I will pursue in the future. Yuri's research group is also a fantastic family. Every person in our group is easy-going and willing to help each other, even though some members have already left. I am so glad to be immersed in such a friendly and relaxed atmosphere. I thank all these members, Prof. Ming-chen Hsu, Prof. Ido Akkerman, Prof. Xiaowei Deng, Prof. Artem Korobenko, and younger members Mr. Georgios Moutsanidis and Mr. Marco Pigazzini.

Secondly, I want to thank my qualification, candidacy and thesis committee members, Professor David Benson, Professor Jiun-Shyan Chen, Professor Kenneth J. Loh, Professor Alison Marsden and Professor Sutanu Sarkar for their suggestions for my research and dissertation. The committee also taught me many courses which are very important for my research. Professor David Benson taught me finite element methods, Professor Jiun-Shyan Chen taught me mesh-free methods, Professor Alison Marsden taught me the numerical methods and Professor Sutanu Sarkar taught me the turbulence modeling. Particularly, I would like to thank Professor David Benson for his support for my career development and sharing me his time during his last busy days at San Diego.

At last, I want to express my appreciation to my parents, my sister, my girlfriend and her parents for their unconditional love and encouragement.

Chapter 2, Chapter 3 and Chapter 4, in part, are a reprint of the materials as it appears in : "Computational free-surface fluid-structure interaction with applications on offshore floating wind turbines" (with A. Korobenko, X. Deng, Y. Bazilevs) *Computers and Fluids*, 2016 and "Free-surface flow modeling and simulation of horizontal-axis tidal-stream

turbines" (with X. Deng, A. Korobenko, Y. Bazilevs) *Computers and Fluids*, 2016. The dissertation author is the primary investigator and author of these papers.

Chapter 5 and Chapter 6, in part, are a reprint of the materials as it appears in : " Experimental and numerical FSI study of compliant hydrofoils" (with B. Augier, A. Korobenko, J. Czarnowski, G. Ketterman, Y. Bazilevs) *Computational Mechanics*, 2016, " FSI modeling of a propulsion system based on compliant hydrofoils in a tandem configuration" (with B. Augier, A. Korobenko, J. Czarnowski, G. Ketterman, Y. Bazilevs) *Computers and Fluids*, 2016 and "Computational free-surface fluid-structure interaction with applications on offshore floating wind turbines" (with A. Korobenko, X. Deng, Y. Bazilevs) *Computers and Fluids*, 2016. The dissertation author is the primary investigator and author of these papers.

VITA

2009	B. S. in Mechanical Engineering, Wuhan University
2012	M. S. in Engineering Mechanics, Peking University
2016	Ph. D. in Structural Engineering, University of California, San Diego

PUBLICATIONS

J. Yan, Y. Bazilevs, A. Korobenko, AE Tejada-Martinez, R. Golshan, " A new variational multiscale formulation for stratified incompressible turbulent flows", *Computers and Fluids*, 2016.

Y. Bazilevs, X. Deng, A. Korobenko, J. Yan. "Fluid-structure interaction modeling for fatigue-damage prediction in full-scale wind-turbine blades", *Journal of Applied Mechanics*, 2016.

T. Opstal, J. Yan, C. Coley, J. Evans, T. Kvamsdal, Y. Bazilevs, " Isogeometric divergence-conforming variational multiscale formulation of incompressible turbulent flows", *Computer Methods in Applied Mechanics and Engineering*, 2016.

J. Yan, X. Deng, A. Korobenko, Y. Bazilevs, "Free-surface flow modeling and simulation of horizontal-axis tidal-stream turbines", *Computers and Fluids*, 2016.

J. Yan, A. Korobenko, X. Deng, Y. Bazilevs, " Computational free-surface fluid-structure interaction with applications on offshore floating wind turbines", *Computers and Fluids*, 2016.

J. Yan, B. Augier, A. Korobenko , J. Czarnowski , G. Keterman , Y. Bazilevs, " FSI modeling of a propulsion system based on compliant hydrofoils in a tandem configuration", *Computers and Fluids*, 2015.

Y. Bazilevs, A. Korobenko, J. Yan, A. Pal, S.M.I.Gohari, S. Sarkar, " ALE-VMS formulation for stratified turbulent incompressible flows with applications", *Mathematical Models and Methods in Applied Science*, 2015.

B. Augier, J. Yan, A. Korobenko, J. Czarnowski, G. Ketterman, Y. Bazilevs, " Experimental and numerical FSI study of compliant hydrofoils", *Computational Mechanics*, 2014.

Y. Bazilevs, J. Yan, M. Stadler, S. Sarkar, " Computation of the flow over a sphere at Re= 3700: A comparison of uniform and turbulent inflow conditions", *Journal of Applied Mechanics*, 2014.

X. Deng, A. Korobenko, J. Yan, Y. Bazilevs, " Isogeometric analysis of continuum damage in rotation-free composite shells", *Computer Methods in Applied Mechanics and Engineering*, 2014.

Y. Bazilevs, A. Korobenko, X. Deng, J. Yan, M. Kinzel, J.O. Dabiri, " FSI modeling of vertical-axis wind turbines", *Journal of Applied Mechanics*, 2014.

Y.Bazilevs, A. Korobenko, X. Deng, J. Yan, " Novel structural modeling and mesh moving techniques for advanced FSI simulation of wind turbines", *International Journal for Numerical Methods in Engineering*, 2014.

J. Liu, J. Yan, S. Lo, " A new insertion sequence for incremental Delaunay triangulation", *Acta Mechanica Sinica*, 2013.

ABSTRACT OF THE DISSERTATION

Computational Free-surface Fluid-structure Interaction with Applications on Offshore Wind and Tidal Energy

by

Jinhui Yan

Doctor of Philosophy in Structural Engineering with a Specialization in Computational Science

University of California, San Diego, 2016

Professor Yuri Bazilevs, Chair

Offshore wind and tides are massive sources of sustainable energy. Simulation-based design has the potential for groundbreaking achievements of offshore energy harvesting structures, such as offshore floating wind turbines and tidal stream turbines. There are many engineering challenges associated with the mechanics of these energy harvesting devices, both on the structural mechanics and fluid mechanics sides, which make the analysis and modeling of these machines quite difficult, especially in harsh ocean environment. This dissertation will focus on the efforts to address some of these challenges through advanced free-surface fluid-structure interaction (free-surface FSI) simulations. In this dissertation, a novel computational free-surface FSI framework using level-set method, finite element

and isogeometric analysis is developed. Considering geometry modeling, aerodynamics, hydrodynamics, free-surface and structural mechanics simultaneously, this formulation enables the simulations of the interaction between free-surface flows and large scale offshore structures with great efficiency, accuracy and robustness. This framework has been applied on a wide range of challenging problems in civil, marine/ocean and mechanical engineering, such as ocean waves, offshore floating wind turbines, tidal energy and bio-inspired aquatic sports equipment.

Chapter 1

Introduction

Offshore renewable resources such as offshore wind and tides are indigenous, clean, and inexhaustible. Offshore energies also play a very important role in marine economy. It is an emerging and booming industry, with strong capability to create jobs and renew the industrial fabric of our regions. From the wind side, according to the prediction from National Renewable Energy Laboratory (NREL) in 2010, offshore wind could produce electricity for almost 39 million households by 2020 [82]. The amount could grow even faster beyond 2020, as offshore wind turbine technology advances. Nowadays, the current trend in offshore wind turbines is to go from land-based to deep-water floating-based designs. Compared with land-based offshore wind turbines, the floating-based offshore wind turbines have the following advantages. a) The wind blows more strongly and consistently, thus more energy can be generated by the offshore floating wind turbines. b) The size of the offshore floating wind turbines is not limited by land transportation, provided the turbines can be assembled along the coastline and safely towed to their operating locations. c) The visual and sound impact of the wind turbine on people's everyday life can be avoided since the floating wind turbines are installed a long distance away from the shore. d) Vast, open sea space is available.

Tidal energy is a another type of sustainable energy. Compared with other forms of renewable energy such as solar energy that heavily rely on the weather, which is constantly changing, tidal energy are increasingly being recognized as a resource to be exploited for

more predictable generation of electrical power. Recently, a large number of technologies have been developed to convert the energy available within tidal currents into electrical power [117, 87, 60, 103, 90]. Among them, horizontal-axis tidal stream turbines (HATTs) are perhaps the most mature and promising technologies. Several companies have been working on implementing their HATTs technology in real-life, including the twin-rotor SeaGen from Marine Current Turbine that is currently undergoing testing off the coast of Northern Ireland [1], and the single rotor turbine from Verdant Power that has been operating successfully in the East River near New York City [2, 57, 49, 99]

According to the report from NREL, the U.S. offshore energy potential ranks second in the world, only after China. We believe that, in order to better exploit the offshore wind and tidal energy, significant resources in the development of offshore floating wind turbines and tidal turbines must be invested. With fast development of computing hardwares and numerical techniques, computational analysis is becoming more and more important in the engineering design process, because experiments are very expensive and sometimes impossible to be performed, especially in harsh ocean environment. We also believe leading-edge computational technologies for wind and tidal energy development, which includes advanced fluid-structure interaction simulations, will be essential in meeting this goal.

However, the current practice in offshore floating wind turbines and tidal stream turbines makes use of either steady (time-independent) or lumped-parameter aerodynamics and hydrodynamics models that are coupled with scaled and simplified turbine structure models. These models are simple to implement and easy to execute, which makes them attractive, especially they are routinely used as part of the design cycle. However, due to the complex nature of operation environment, where the offshore floating wind turbines and tidal turbines are subjected to high Reynolds number turbulent wind flow and violent sea waves, also due to the 3D complex geometry and composite material distribution of the structures, these simplified models are unable to represent the response of the structures to the time-dependent, harsh multiphysics phenomenon. It is precisely these extreme events that cause failures and reduce the life cycle of floating wind turbines and tidal turbines, leading to premature maintenance and repair, as a result, to increased cost of wind and tidal

energy.

In this dissertation, we introduce a paradigm shift in offshore energy modeling and simulation by developing a 3D, complex geometry, time-dependent, multi-scale, multi-physics, computational free-surface fluid-structure interaction framework. To model the free-surface flows, the level set method [114, 113, 4, 3, 5, 86] is adopted to track the evolution of air-water interface. The aerodynamics and hydrodynamics are governed by an unified two-fluid incompressible Navier-Stokes, in which fluid density and viscosity are evaluated by the assistance of Heaviside function based on the value of level set function. The finite element based Arbitrary Lagrangian Eulerian Variational Multi-scale (ALE-VMS) formulation is employed to discretize the free-surface flow equations. In order to handle the high Reynolds number turbulent flows in large scale engineering CFD and FSI calculations, weakly enforcement essential boundary conditions (weak BCs) [32, 38, 39, 59] are adopted at the fluid-structure interface. ALE-VMS may be viewed as an extension of the residual-based variational multi-scale (RBVMS) turbulence model [17, 16] to moving domains using the ALE technique, while the weak BCs relax the boundary layers resolution requirement in large spatial engineering applications without losing solution accuracy on meshes of reasonable size. ALE-VMS in conjunction with weak BCs has been successfully employed for many chanllenging CFD and FSI problems, such as stratified flows [37, 165], the aerodynamics simulations [24, 66, 74, 68, 92] and FSI simulations of wind turbines [26, 31, 72, 95, 34], spacecraft parachutes [148, 132, 134, 131, 136, 139, 145, 156] and cardiovascular fluid mechanics and FSI [107, 29, 30, 71, 104, 124, 126, 160, 167, 133, 137, 144]. To better capture the evolution of air-water interface, two additional level-set techniques, called re-distancing and mass balancing are proposed. Re-distancing process re-initialize the level set field to satisfy the signed distance property, which is favorable for the sharp interface topological change, while mass balancing insure the global mass conservation during the simulations.

In many engineering applications, structural components are usually in relative motion, like spinning rotor and nonspinning tower and nacelle in wind turbines and tidal turbines, or the front hydrofoil and back hydrofoil of the Kayak propulsion system which are rotating in opposite directions. In order to simulate the flows around the components in

relative motions and capture the interaction between them, a sliding interface technique is proposed. In sliding interface technique, the fluid domain is divided into subdomains, which contains different structural components and move in a way that accommodate the motions of these components. These subdomains do not overlap, sharing a sliding interface between them. The sliding interface is allowed to be in any shape. The compatibilities of fluid solutions is enforced in weakly by this so-called sliding interface technique. The sliding interface technique was originally developed in [33] in the context of Isogeometric Analysis (IGA) [75, 52] for computing flows about rotating components and has been applied on many CFD and FSI computations. In this dissertation, the sliding interface technique is extended for free-surface flows. In this dissertation, a novel level-set re-distancing procedure that is compatible with the sliding-interface technique is also developed.

The structural mechanics equations are solved using Isogeometric Analysis (IGA) [52, 75]. Since its conception, IGA has been widely used in many areas of computational mechanics, engineering and sciences, showing improved performance over the standard Finite Element Method (FEM) [115, 35, 20, 53, 21, 163, 162, 55]. We also note that for most of structures of offshore energy harvesting devices are essential thin shells, beams and cables. Thus, the structural mechanics are governed by the isogeometric rotation-free shell, beam/cable formulation with the aid of the bending strip method [88], which is proposed to handle multi-patch discretization. The shell, beam/cable formulations are discretized using Isogeometric Analysis (IGA) with nonuniform rational B-spline (NURBS) [52, 75] and make use of only displacement degrees of freedom. Using IGA for structural modeling presents a good combination of efficiency, since no rotational degrees-of-freedom are employed, accuracy, since NURBS are a higher-order accurate discretization technique [42], and robustness. The latter refers to the fact that higher-order continuity of NURBS induces smooth deformation of the structural surface, which in turn, translates to smooth deformation of the fluid mechanics mesh at the fluid-structure interface, and, as a result, leads to better quality of boundary-layer discretization near moving surfaces.

Mesh motion is handled by solving the elastostatic equations with jacobian-based stiffening. Augmented Lagranigan approach is utilized to derive the couple problems for free-

surface FSI. Because of the using of IGA for structure and FEM for fluid, the free-surface FSI formulation presented in this paper assumes non-matching discretization at fluid-structure interface [31]. Non-matching discretizations at the fluid-structure interface require the use of interpolation or project of kinematic and traction data between the nonmatching surface meshes.

To handle the added mass effect, a quasi-direct coupling FSI solution strategy [40] is developed to solve the discrete FSI equations at each nonlinear iteration within a time step. The quasi-direct coupling approach is a strongly coupled FSI technique where, at the level of Newton iterations, the increments of unknowns of FSI equations are solved by two sequential blocks. The first block, also called by physics block, which includes fluid, level set and structure, is simultaneously solved by flexible GMRES (FGMRES) [118] with matrix-free technique. The second block, the mesh block, is solved by Conjugate Gradient solver [64] with left hand matrix and right hand vector assembled with the most updated solutions from the physics block. To the best knowledge of us, it is the most robust coupled FSI solution strategy while maintaining great efficiency for marine engineering simulations.

The dissertation is outlined as follows. In Chapter 2, we present the formulation of the free-surface flow. The strong form governing equations of free-surface flow using level set method and two-fluid Navier Stokes equations are presented in Chapter 2.1. In Chapter 2.2, the discrete formulations of free-surface flows at the space-discrete level, including ALE-VMS and weakly enforcement of essential boundary conditions, are shown. Two additional techniques of the level set field, re-distancing and mass balancing, are also described in this section. The sliding interface technique for Navier-Stokes and level set is presented in Chapter 2.2.5. The re-distancing procedure compatible with sliding interface is shown in Chapter 2.2.6.

In Chapter 3, we present the applications of the formulation of free-surface flow on two engineering problems. The free-surface formulation is first validated on the benchmark problem of solitary wave impacting a rigid and fixed platform, which is shown in Chapter 3.1. Then free-surface simulations of horizontal axis tidal stream turbines are performed in Chapter 3.2. Computational results are compared against experimental results obtained

by other researchers. The free-surface effect on tidal stream turbine performance is also investigated.

In Chapter 4, we present the formulation of structural mechanics. The strong form and weak form equations of structural mechanics are given in Chapter 4.1. Then, the isogeometric rotation-free shell, beam/cable formulation is shown in Chapter 4.3 and Chapter 4.2.

In Chapter 5, we present the free-surface FSI formulation. The angmented Lagrangian approach, which we utilize to derive the coupled free-surface FSI formulation, is presented in Chapter 5.1. Then, the time integration algorithm and coupling strategies are presented in Chapter 5.2 and Chapter 5.3 respectively.

In Chapter 6, we present the applications of the proposed free-surface FSI formulation on a bio-inspired engineering problem and a wind energy problem. The FSI studies of compliant hydrofoils for Kayak propulsion system from Hobbie Cat company are presented in Chapter 6.1. Both single foil configuration and double foils in tandem configuration are investigated. Simulations results match very well with field test data from the Hobbie Cat company. The formulation is currently being used by the company in their design and optimization process. The free-surface FSI simulations of OC3-Hywind floating wind turbines subjected to Airy waves and waves generated by numerical wave tank are presented in Chapter 6.2.2 and Chapter 6.2.3.

In Chapter 7, we draw conclusions.

Chapter 2

Free surface flows

2.1 Governing equations of free-surface flows

In this section, the governing differential equations of free-surface flows on a moving domain are summarized. Let $\Omega_t \in \mathbb{R}^d$ $(d = 2, 3)$ denote the combined air-water domain at time t and let Γ_t denote its boundary. The domain Ω_t is decomposed into the water subdomain and air subdomain, denoted by Ω_t^w and Ω_t^a, respectively. Γ_t^{aw} denotes the interface between the air subdomain and water subdomain. See Figure. 2.1 for an illustration.

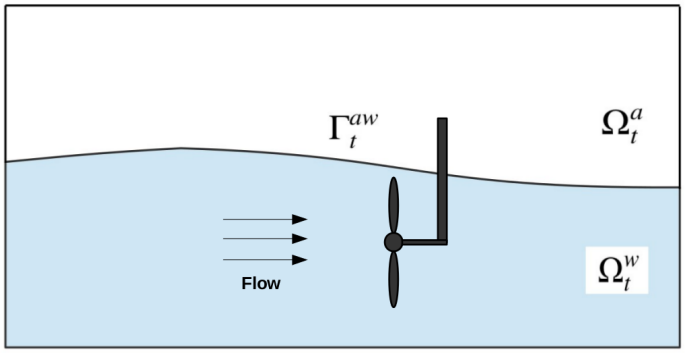

Figure 2.1: The fluid spatial domain with two different types of fluids

In present work, the level set method is adopted to capture the air-water interface [44, 114, 113, 4, 3, 5, 86, 166]. For this, we introduce a scalar function $\phi(\mathbf{x}, t)$ and define the water subdomain, air subdomain and the air-water interface as

$$\Omega_t^a = \{\mathbf{x} | \phi(\mathbf{x}, t) < 0, \forall \mathbf{x} \in \Omega_t\} \tag{2.1}$$

$$\Omega_t^w = \{\mathbf{x} | \phi(\mathbf{x}, t) > 0, \forall \mathbf{x} \in \Omega_t\} \tag{2.2}$$

$$\Gamma_t^{aw} = \{\mathbf{x} | \phi(\mathbf{x}, t) = 0, \forall \mathbf{x} \in \Omega_t\} \tag{2.3}$$

To distinguish air subdomain, water subdomain, each point of the two-fluid air-water medium will be assigned the corresponding values to the fluid density ρ and viscosity μ, which are assumed to be computed as

$$\rho = \rho_w H(\phi) + \rho_a (1 - H(\phi)) \tag{2.4}$$

$$\mu = \mu_w H(\phi) + \mu_a (1 - H(\phi)) \tag{2.5}$$

where $H(\phi)$ is the Heaviside function defined by Eq. 2.6, ρ_a and ρ_w are the densities of air and water, respectively, μ_a and μ_w are the viscosities of air and water, respectively.

$$H(\phi) = \begin{cases} 0 & \text{if } \phi \leq 0 \\ 1/2 & \text{if } \phi = 0 \\ 1 & \text{if } \phi > 0 \end{cases} \tag{2.6}$$

With the fluid material properties given, the two-fluid Navier-Stokes equations of incompressible flow in the Arbitrary Lagrangian-Eulerian (ALE) description can be written as

$$\rho \left(\left. \frac{\partial \boldsymbol{u}}{\partial t} \right|_{\hat{x}} + (\boldsymbol{u} - \hat{\boldsymbol{u}}) \cdot \boldsymbol{\nabla}_x \boldsymbol{u} - \boldsymbol{f} \right) - \boldsymbol{\nabla}_x \cdot \boldsymbol{\sigma} = \mathbf{0} \tag{2.7}$$

$$\boldsymbol{\nabla}_x \cdot \boldsymbol{u} = 0 \tag{2.8}$$

where the fluid Cauchy stress, $\boldsymbol{\sigma}$, is defined as

$$\boldsymbol{\sigma}(\boldsymbol{u}, p) = -p\boldsymbol{I} + 2\mu\boldsymbol{\nabla}_x^s\boldsymbol{u} \tag{2.9}$$

$\boldsymbol{u}$ and p are the fluid velocity and pressure, $\boldsymbol{f}$ is the body force per unit fluid mass, $\hat{\boldsymbol{u}}$ is the velocity of the fluid domain, and $\boldsymbol{\nabla}_x^s$ is the symmetric gradient operator, defined as

$$\boldsymbol{\nabla}_x^s\boldsymbol{u} = \frac{\boldsymbol{\nabla}_x\boldsymbol{u} + (\boldsymbol{\nabla}_x\boldsymbol{u})^T}{2} \tag{2.10}$$

The air-water interface is assumed to move with the fluid material particles, which is modeled by means of an additional convection equation of the level set ϕ in the ALE description as

$$\left.\frac{\partial\phi}{\partial t}\right|_{\hat{x}} + (\boldsymbol{u} - \hat{\boldsymbol{u}}) \cdot \boldsymbol{\nabla}_x\phi = 0 \tag{2.11}$$

In the above equations, the partial time derivatives are taken with respect to a referential coordinate $\hat{x}$ held fixed. The space derivatives are taken with respect to the current configuration spatial coordinates denoted by x. The fluid domain velocity is assumed to be completely independent of the velocity of the fluid material particles, which gives the freedom to choose appropriate mesh motion techniques that are suitable for the problems. The above equations, with the associated initial and boundary conditions, constitute a formulation of free-surface flow on a moving domain at continuous level.

2.2 Discrete formulation of free-surface flows

2.2.1 ALE-VMS

In order to handle the high Reynolds number two-fluid flows, the Arbitrary Lagrangian-Eulerian Variational Multi-scale (ALE-VMS) formulation [28, 127], which has been applied

to a variety of challenging CFD and FSI problems [93, 164, 7, 36, 37, 34], is adopted to discretize the Navier-Stokes and level set equations.

Let $\mathcal{V}_f^h$ denote the discrete trial function space for the velocity-pressure-level set triple $\{\boldsymbol{u}^h, p^h, \phi^h\}$ and let $\mathcal{W}_f^h$ be the discrete testing function space for the linear momentum, continuity and level set equations $\{\mathbf{w}^h, q^h, \eta^h\}$. The ALE-VMS formulation is stated as follows: Find $\{\boldsymbol{u}^h, p^h, \phi^h\} \in \mathcal{V}_f^h$ such that $\forall \{\mathbf{w}^h, q^h, \eta^h\} \in \mathcal{W}_f^h$:

$$\boldsymbol{B}_f(\{\boldsymbol{w}^h, q^h, \eta^h\}, \{\boldsymbol{u}^h, p^h, \phi^h\}; \hat{\boldsymbol{u}}^h) = \boldsymbol{F}_f(\{\boldsymbol{w}^h, q^h, \eta^h\}) \tag{2.12}$$

where $\boldsymbol{B}_f$ and $\boldsymbol{F}_f$ are given as

$$\begin{aligned}
\boldsymbol{B}_f(\{\boldsymbol{w}^h, q^h, \eta^h\}, \{\boldsymbol{u}^h, p^h, \phi^h\}; \hat{\boldsymbol{u}}^h) &= \int_{\Omega_t} \boldsymbol{w}^h \cdot \rho \left(\left.\frac{\partial \boldsymbol{u}}{\partial t}\right|_{\hat{x}} + (\boldsymbol{u}^h - \hat{\boldsymbol{u}}^h) \cdot \boldsymbol{\nabla}_x \boldsymbol{u}^h \right) \mathrm{d}\Omega \\
&+ \int_{\Omega_t} \boldsymbol{\nabla}_x \mathbf{w}^h : \boldsymbol{\sigma}(\boldsymbol{u}^h, p^h) \, \mathrm{d}\Omega + \int_{\Omega_t^e} q^h \boldsymbol{\nabla}_x \cdot \boldsymbol{u}^h \, \mathrm{d}\Omega \\
&+ \int_{\Omega_t} \eta^h \left(\left.\frac{\partial \phi^h}{\partial t}\right|_{\hat{x}} + (\boldsymbol{u}^h - \hat{\boldsymbol{u}}^h) \cdot \boldsymbol{\nabla}_x \phi^h \right) \mathrm{d}\Omega \\
&+ \sum_{e=1}^{nel} \int_{\Omega_t^e} \tau_M \left((\boldsymbol{u}^h - \hat{\boldsymbol{u}}^h) \cdot \boldsymbol{\nabla}_x \mathbf{w}^h + \frac{\boldsymbol{\nabla}_x q^h}{\rho} \right) \cdot \mathbf{r}_M(\boldsymbol{u}^h, p^h) \, \mathrm{d}\Omega \\
&+ \sum_{e=1}^{nel} \int_{\Omega_t^e} \rho \tau_C \boldsymbol{\nabla}_x \cdot \mathbf{w}^h r_C(\boldsymbol{u}^h, p^h) \, \mathrm{d}\Omega \\
&- \sum_{e=1}^{nel} \int_{\Omega_t^e} \tau_M \mathbf{w}^h \cdot \left(\mathbf{r}_M(\boldsymbol{u}^h, p^h) \cdot \boldsymbol{\nabla}_x \boldsymbol{u}^h \right) \mathrm{d}\Omega \\
&- \sum_{e=1}^{nel} \int_{\Omega_t^e} \frac{\boldsymbol{\nabla}_x \mathbf{w}^h}{\rho} : \left(\tau_M \mathbf{r}_M(\boldsymbol{u}^h, p^h) \right) \otimes \left(\tau_M \mathbf{r}_M(\boldsymbol{u}^h, p^h) \right) \mathrm{d}\Omega \\
&+ \sum_{e=1}^{nel} \int_{\Omega_t^e} \tau_\phi (\boldsymbol{u}^h - \hat{\boldsymbol{u}}^h) \cdot \boldsymbol{\nabla}_x \eta^h r_\phi(\phi^h, \boldsymbol{u}^h) \, \mathrm{d}\Omega
\end{aligned} \tag{2.13}$$

$$\boldsymbol{F}_f(\boldsymbol{w}^h, q^h, \eta^h) = \int_{\Omega_t} \rho \boldsymbol{w}^h \cdot \boldsymbol{f}^h \, \mathrm{d}\Omega + \int_{\Gamma_t^h} \boldsymbol{w}^h \cdot \mathbf{h} \, \mathrm{d}\Gamma \tag{2.14}$$

Where Γ_h is the Neumann boundary and $\boldsymbol{h}$ is the applied traction. All the integrals in Eq. 2.12 are taken element-wise, $\mathbf{r}_M(\boldsymbol{u}^h, p^h)$ and $r_C(\boldsymbol{u}^h, p^h)$ and $r_\phi(\phi^h)$ are residuals of the fluid momentum, fluid continuity and level set convection equations at element level given as

$$\mathbf{r}_M(\boldsymbol{u}^h, p^h) = \rho \left(\left. \frac{\partial \boldsymbol{u}^h}{\partial t} \right|_{\hat{x}} + (\boldsymbol{u}^h - \hat{\boldsymbol{u}}^h) \cdot \boldsymbol{\nabla}_x \boldsymbol{u}^h - \boldsymbol{f} \right) - \boldsymbol{\nabla}_x \cdot \boldsymbol{\sigma}(\boldsymbol{u}^\mathbf{h}, \mathbf{p}^\mathbf{h}) \tag{2.15}$$

$$r_C(\boldsymbol{u}^h, p^h) = \boldsymbol{\nabla}_x \cdot \boldsymbol{u}^h \tag{2.16}$$

$$r_\phi(\phi^h, \boldsymbol{u}^h) = \left. \frac{\partial \phi^h}{\partial t} \right|_{\hat{x}} + (\boldsymbol{u}^h - \hat{\boldsymbol{u}}^h) \cdot \boldsymbol{\nabla}_x \phi^h \tag{2.17}$$

and the τ_M, τ_C , τ_ϕ are the stabilization parameters given by

$$\tau_M = \left(\frac{4}{\Delta t^2} + (\boldsymbol{u}^h - \hat{\boldsymbol{u}}^h) \cdot \mathbf{G} (\boldsymbol{u}^h - \hat{\boldsymbol{u}}^h) + C_I \left(\frac{\mu}{\rho} \right)^2 \mathbf{G} : \mathbf{G} \right)^{-1/2} \tag{2.18}$$

$$\tau_C = \frac{1}{tr(\mathbf{G}) \tau_M} \tag{2.19}$$

$$\tau_\phi = \left(\frac{4}{\Delta t^2} + (\boldsymbol{u}^h - \hat{\boldsymbol{u}}^h) \cdot \mathbf{G} (\boldsymbol{u}^h - \hat{\boldsymbol{u}}^h) \right)^{-1/2} \tag{2.20}$$

where C_I is a dimensionless positive constant derived from element-wise inverse estimate [63]. $\mathbf{G}$ is the mesh metric tensor, defined by

$$\mathbf{G} = \left(\frac{\partial \xi}{\partial \mathbf{x}} \right)^T \frac{\partial \xi}{\partial \mathbf{x}} \tag{2.21}$$

where $\frac{\partial \xi}{\partial \mathbf{x}}$ denotes the Jacobian matrix of the map between the parametric element and its physical counterpart.

2.2.2 Weak enforcement of essential BCs

In large scale engineering computations, fully resolving the boundary layers is impossible. In this case, another ingredient needed to be augmented with the ALE-VMS is the weakly enforcement of essential boundary conditions. In this section we state the formulation of the weakly enforced essential boundary conditions. This was first proposed [32] for the advection-diffusion equation and Navier-Stokes equations of incompressible flows in an effort to improve the accuracy of stabilized and multiscale formulations in the presence of unresolved boundary layers. The weak boundary condition formulation may thought of as an extension of Nitsches method [112] to the case of the Navier-Stokes equations of incompressible flow. Another interpretation of the weak boundary condition formulation is that it is a Discontinuous Galerkin method [6], where the continuity of the basis functions is enforced everywhere in the domain interior, but not at the domain boundary. The method for the weakly enforced boundary condition was further refined and studied in a set of challenging wall-bounded turbulent flows [39, 38, 16].

To account for the weak enforcement of the essential boundary conditions, we remove the essential boundary conditions from the trial and test function sets and modify the discrete variational formulation (Eq. 2.12) as: find $\{\boldsymbol{u}^h, p^h, \phi^h\} \in \mathcal{V}_f^h$ such that $\forall \{\mathbf{w}^h, q^h, \eta^h\} \in \mathcal{W}_f^h$:

$$\boldsymbol{B}_f(\{\boldsymbol{w}^h, q^h, \eta^h\}, \{\boldsymbol{u}^h, p^h, \phi^h\}; \hat{\boldsymbol{u}}^h) + \boldsymbol{B}_f^{WBC}(\{\boldsymbol{w}^h, q^h\}, \{\boldsymbol{u}^h, p^h\}; \hat{\boldsymbol{u}}^h) - \boldsymbol{F}_f(\{\boldsymbol{w}^h, q^h, \eta^h\}) = 0 \tag{2.22}$$

where $\boldsymbol{B}_f^{WBC}(\{\boldsymbol{w}^h, q^h\}, \{\boldsymbol{u}^h, p^h\}$ is given by

$$\begin{aligned}
&\boldsymbol{B}_f^{WBC}(\{\boldsymbol{w}^h, q^h\}, \{\boldsymbol{u}^h, p^h\}; \hat{\boldsymbol{u}}^h) = \qquad (2.23)\\
&- \sum_{b=1}^{n_{eb}} \int_{\Gamma_t^b \cap \Gamma_t^g} \boldsymbol{w}^h \cdot \boldsymbol{\sigma}(\boldsymbol{u}^h, p^h)\boldsymbol{n} \, \mathrm{d}\Gamma \\
&- \sum_{b=1}^{n_{eb}} \int_{\Gamma_t^b \cap \Gamma_t^g} \left(2\mu(\boldsymbol{\nabla}_x^S \boldsymbol{w}^h)\boldsymbol{n} + q^h \boldsymbol{n}\right) \cdot (\boldsymbol{u}^h - \mathbf{g}^h) \, \mathrm{d}\Gamma \\
&- \sum_{b=1}^{n_{eb}} \int_{\Gamma_t^b \cap (\Gamma_t^g)^-} \boldsymbol{w}^h \cdot \rho(\boldsymbol{u}^h \cdot \boldsymbol{n})(\boldsymbol{u}^h - \mathbf{g}^h) \, \mathrm{d}\Gamma \\
&+ \sum_{b=1}^{n_{eb}} \int_{\Gamma_t^b \cap \Gamma_t^g} \tau_B \boldsymbol{w}^h \cdot (\boldsymbol{u}^h - \mathbf{g}^h) \, \mathrm{d}\Gamma \qquad (2.24)
\end{aligned}$$

where $\mathbf{g}^h$ is the prescribed velocity on Γ_t^g. The Γ_t^g is decomposed into n_{eb} surfaces denoted with Γ_t^b, $(\Gamma_t^g)^-$ denotes the inflow part of Γ_t^g:

$$(\Gamma_t^g)^- = \left\{ \mathbf{x} \,\middle|\, \boldsymbol{u}^h \cdot \boldsymbol{n} < 0, \forall \mathbf{x} \in \Omega^t \right\} \qquad (2.25)$$

τ_B is a small parameter that ensures boundary stability. For a thorough derivation and discussion of the weakly enforcement of essential boundary conditions, the readers are referred to [38]

2.2.3 Additional level set techniques: Re-distancing

In discrete setting, the fluid density and viscosity are computed as

$$\rho = \rho_w H_\epsilon(\phi) + \rho_a(1 - H_\epsilon(\phi)) \qquad (2.26)$$

$$\mu = \mu_w H_\epsilon(\phi) + \mu_a(1 - H_\epsilon(\phi)) \qquad (2.27)$$

where the $H_\epsilon(\phi)$ is the regularized version of Heaviside function, namely:

$$H_\epsilon(\phi) = \begin{cases} 0 & \text{if } \phi < -\epsilon \\ \frac{1}{2}\left(1 + \frac{\phi}{\epsilon} + \frac{1}{\pi} sin\left(\frac{\phi\pi}{\epsilon}\right)\right) & \text{if } |\phi| \leq \epsilon \\ 1 & \text{if } \phi > \epsilon \end{cases} \tag{2.28}$$

where ϵ, assumed to scale with the local mesh size, defines the interface width between the air subdomain and water subdomain. As mesh is refined, $\epsilon \to 0$.

While the regularized Heaviside function in Eq. 2.28 gives a smooth transition from zero to unity within a small band of elements around the interface, and is numerically more favorable to the sharp discontinuity, this regularization places a requirement on the level-set field ϕ^h to satisfy the so-called signed-distance property in the transition layer between the two fluids. For this, we define an additional field, ϕ_d^h, which satisfies the Eikonal equation, namely,

$$\left\|\boldsymbol{\nabla}_x \phi_d^h\right\| = 1 \text{ in } \Omega_t \tag{2.29}$$

subject to the constraint that the interface defined by the zero level set of ϕ^h is preserved, namely,

$$\phi_d^h = \phi^h = 0 \text{ on } \Gamma_t^{aw} \tag{2.30}$$

In order to satisfy Eq. 2.29 and Eq. 2.30, we make the Eikonal equation pseudo-time-dependent (we denote pseudo-time by $\tilde{t}$), discretize it using a VMS technique, and add a suitably-constructed penalty term to enforce the interior constraint on ϕ_d^h given by Eq. 2.30. The resulting semi-discrete form of the governing equations may be stated as: given $\phi(x,t)^h$, find ϕ_d^h, such that $\forall \eta_d^h$:

$$\boldsymbol{B}_{re}(\eta_d^h, \phi_d^h) - \boldsymbol{F}_{re}(\eta_d^h) = 0 \tag{2.31}$$

where

$$\boldsymbol{B}_{re}(\eta_d^h, \phi_d^h) = \int_{\Omega_t} \eta_d^h \left(\frac{\partial \phi_d^h}{\partial \tilde{t}} + \mathbf{a} \cdot \boldsymbol{\nabla}_x \phi_d^h \right) \mathrm{d}\Omega + \int_{\Omega_t} \tau_{\phi_d} \mathbf{a} \cdot \boldsymbol{\nabla}_x \eta_d^h \left(\frac{\partial \phi_d^h}{\partial \tilde{t}} + \mathbf{a} \cdot \boldsymbol{\nabla}_x \phi_d^h \right) \mathrm{d}\Omega \quad (2.32)$$

$$\boldsymbol{F}_{re}(\eta_d^h) = \int_{\Omega_t} \eta_d^h S_\epsilon(\phi^h) \, \mathrm{d}\Omega + \int_{\Omega_t} \tau_{\phi_d} S_\epsilon(\phi^h) \mathbf{a} \cdot \boldsymbol{\nabla}_x \eta_d^h \, \mathrm{d}\Omega \quad (2.33)$$

where $S_\epsilon(\phi^h) = 2H_\epsilon(\phi^h) - 1$ is the regularized sign function, $\mathbf{a} = S_\epsilon(\phi^h) \boldsymbol{\nabla}_x \phi_d^h \Big/ \left\| \boldsymbol{\nabla}_x \phi_d^h \right\|$ is an effective "convective" velocity, and τ_{ϕ_d} is the stabilized parameter, given by

$$\tau_{\phi_d} = \left(\frac{4}{\Delta t^2} + \mathbf{a} \cdot \mathbf{G}\mathbf{a} \right)^{-1/2} \quad (2.34)$$

The choice of the pseudo-time step is based on the convective CFL for the Eikonal equation, and is computed as

$$\Delta \tilde{t} = 2\gamma \min_{\mathbf{x} \in \Omega_t} \left(S_\epsilon(\phi^h) \frac{\boldsymbol{\nabla}_x \phi_d^h}{\left\| \boldsymbol{\nabla}_x \phi_d^h \right\|} \cdot \mathbf{G} S_\epsilon(\phi^h) \frac{\boldsymbol{\nabla}_x \phi_d^h}{\left\| \boldsymbol{\nabla}_x \phi_d^h \right\|} \right)^{-1/2} \quad (2.35)$$

where $\gamma = 1$ corresponds to the CFL unit. To ensure the constraint, the following term is added to the left handed to Eq. 2.31

$$\int_{\Omega_t} \eta_d^h \lambda_{pen} \frac{dH_\epsilon(\phi^h)}{d\phi^h} (\phi_d^h - \phi^h) \, \mathrm{d}\Omega \quad (2.36)$$

where λ_{pen} is the penalty parameter. It is important to note that $\frac{dH_\epsilon(\phi^h)}{d\phi^h}$ is only nonzero in a band of elements around the air-water interface, and thus the penalty term is only active near the air-water interface, which is the desired construction. Also note that the presence of $\frac{dH_\epsilon(\phi^h)}{d\phi^h}$ produces the correct scaling of the penalty term and makes the penalty parameter λ_{pen} independent of the mesh size.

$\phi_d = \phi$ at $\tilde{t} = 0$. At each time step, Eq. 2.31 is integrated in pseudo-time, which gives a new level set field ϕ_d with the signed distance property and zero level set coincident with that of ϕ. After this re-distancing process is done, we set $\phi = \phi_d$ at the end of the time step.

2.2.4 Additional level set techniques: Mass balancing

Both convection and re-distancing of the level set may result in the loss or gain of the total fluid mass. The amount of mass deficit depends on many factors. One is more likely to significantly upset the mass balance on a coarse problem mesh than on a fine problem mesh. Significant mass loss or gain may also occur when the discrete equations are integrated for a long time period. In this case, seemingly minor mass errors for a given time step may compound into a large mass error at the end of the computation. As a result, a mass correction procedure is necessary. As a result, the mass balance procedure is proposed. We make use of the basic global mass balancing law, which reads

$$\frac{d}{dt}\int_{\Omega_t}\rho \,\mathrm{d}\Omega = \int_{\Gamma_t}\rho(\boldsymbol{u}-\hat{\boldsymbol{u}})\cdot\boldsymbol{n}\,\mathrm{d}\Gamma \tag{2.37}$$

We integrate Eq. 2.37 in time over the time interval (t_n, t_{n+1}) and approximate the term corresponding to the boundary integral using midpoint to obtain:

$$\frac{\int_{\Omega_t^{n+1}}\rho_{n+1}\,\mathrm{d}\Omega - \int_{\Omega_t^{n}}\rho_n\,\mathrm{d}\Omega}{\Delta t} = \int_{\Gamma_t^{n+1/2}}\frac{\rho_{n+1}+\rho_n}{2}(\boldsymbol{u}^h_{n+1/2}-\hat{\boldsymbol{u}}_{n+1/2})\cdot\boldsymbol{n}_{n+1/2}\,\mathrm{d}\Gamma \tag{2.38}$$

where $\rho_{n+1} = \rho((\phi_d^h)_{n+1} + \phi')$ and $\rho_n = \rho((\phi_d^h)_n)$. Eq. 2.38 is a time discrete version of the global mass balance law. Note we perturb the re-distanced level set function ϕ^h_{n+1} by a global constant ϕ' in order to ensure the mass balance at t_{n+1}. Eq. 2.38 is satisfied for the regularized fluid density ρ evaluated by Eq. 2.26. This procedure ensures the global mass balance at every time step. To achieve mass balance at local sense, the method in [86] can be employed. After the re-distancing and mass balance procedure is finished, the level set function is updated by

$$\phi^h = \phi^h_d + \phi' \tag{2.39}$$

2.2.5 Sliding interface technique for ALE-VMS

In many engineering CFD and FSI simulations of realistic engineering machines, we are facing the challenging of how to handle the flows around mechanical components in relative motions. Let's use horizontal axis wind turbine as an example. In order to simulate the full tidal stream turbine configuration, which includes the rotating tidal turbine rotor and the stationary nacelle and tower, we consider an approach that utilizes a moving subdomain, which encloses the entire rotating rotor, and a stationary subdomain that contains the rest of the tidal turbine (See Fig 2.2). The subdomain contains the rotor rotates with it. The two domains are in relative motion and share a sliding cylindrical interface. The meshes on each side of the interface are nonmatching and can slide with respect to each other due to the relative motion of the enclosed structures. The compatibility conditions of velocity, level set and traction are enforced at the sliding interface, namely,

$$\boldsymbol{u}_{s1} = \boldsymbol{u}_{s2} \tag{2.40}$$

$$\phi_{s1} = \phi_{s1} \tag{2.41}$$

$$(-p_{s1}\boldsymbol{I} + 2\mu\boldsymbol{\nabla}^s\boldsymbol{u}_{s1})\boldsymbol{n}_{s1} = (-p_{s2}\boldsymbol{I} + 2\mu\boldsymbol{\nabla}^s\boldsymbol{u}_{s2})\boldsymbol{n}_{s2} \tag{2.42}$$

where all quantities with subscripts $s1$ and $s2$ refer to the two sliding subdomains, respectively, and $\boldsymbol{n}_{s1}$ and $\boldsymbol{n}_{s2}$ are the corresponding outward normal vectors.

Compatibility conditions given by the above Eqs. 2.40- 2.42 are enforced weakly in the framework of the sliding-interface technique. Using sliding interface technique, we add the following terms to the ALE-VMS formulation given by Eq.2.12. Finally, we get the following formulation for free-surface flows, namely, find $\{\boldsymbol{u}^h, p^h, \phi^h\} \in \mathcal{V}_f^h$ such that

$\forall\{\mathbf{w}^h, q^h, \eta^h\} \in \mathcal{W}_f^h$:

$$
\begin{aligned}
&\boldsymbol{B}_f(\{\boldsymbol{w}^h, q^h, \eta^h\}, \{\boldsymbol{u}^h, p^h, \phi^h\}; \hat{\boldsymbol{u}}^h) + \boldsymbol{B}_f^{WBC}(\{\boldsymbol{w}^h, q^h\}, \{\boldsymbol{u}^h, p^h\}; \hat{\boldsymbol{u}}^h) - \boldsymbol{F}_f(\{\boldsymbol{w}^h, q^h, \eta^h\}) \\
&- \sum_{b=1}^{Neb} \int_{\Gamma_t^b \cap \Gamma_t^{SI}} \frac{1}{2}(\mathbf{w}_{s1}^h - \mathbf{w}_{s2}^h) \cdot (\boldsymbol{\sigma}_{s1}\mathbf{n}_{s1} - \boldsymbol{\sigma}_{s2}\mathbf{n}_{s2})\, \mathrm{d}\Gamma \\
&- \sum_{b=1}^{Neb} \int_{\Gamma_t^b \cap \Gamma_t^{SI}} \frac{1}{2}(\delta\boldsymbol{\sigma}_{s1}\mathbf{n}_{s1} - \delta\boldsymbol{\sigma}_{s2}\mathbf{n}_{s2}) \cdot (\mathbf{u}_{s1}^h - \mathbf{u}_{s2}^h)\, \mathrm{d}\Gamma \\
&- \sum_{b=1}^{Neb} \int_{\Gamma_t^b \cap \Gamma_t^{SI}} \mathbf{w}_{s1}^h \cdot \rho \left[(\mathbf{u}_{s1}^h - \hat{\mathbf{u}}_{s1}^h) \cdot \mathbf{n}_{s1}\right]_- (\mathbf{u}_{s1}^h - \mathbf{u}_{s2}^h)\, \mathrm{d}\Gamma \\
&- \sum_{b=1}^{Neb} \int_{\Gamma_t^b \cap \Gamma_t^{SI}} \mathbf{w}_{s2}^h \cdot \rho \left[(\mathbf{u}_{s2}^h - \hat{\mathbf{u}}_{s2}^h) \cdot \mathbf{n}_{s1}\right]_- (\mathbf{u}_{s2}^h - \mathbf{u}_{s1}^h)\, \mathrm{d}\Gamma \\
&+ \sum_{b=1}^{Neb} \int_{\Gamma_t^b \cap \Gamma_t^{SI}} \frac{C_I^B \mu}{h_n}(\mathbf{w}_{s1}^h - \mathbf{w}_{s2}^h) \cdot (\mathbf{u}_{s1}^h - \mathbf{u}_{s2}^h)\, \mathrm{d}\Gamma \\
&- \sum_{b=1}^{Neb} \int_{\Gamma_t^b \cap \Gamma_t^{SI}} \eta_{s1}^h \left[(\mathbf{u}_{s1}^h - \hat{\mathbf{u}}_{s1}^h) \cdot \mathbf{n}_{s1}\right]_- (\phi_{s1}^h - \phi_{s2}^h)\, \mathrm{d}\Gamma \\
&- \sum_{b=1}^{Neb} \int_{\Gamma_t^b \cap \Gamma_t^{SI}} \eta_{s2}^h \left[(\mathbf{u}_{s2}^h - \hat{\mathbf{u}}_{s2}^h) \cdot \mathbf{n}_{s2}\right]_- (\phi_{s2}^h - \phi_{s1}^h)\, \mathrm{d}\Gamma = 0
\end{aligned}
\tag{2.43}
$$

where Γ_t^{SI} is the sliding interface, $\delta\boldsymbol{\sigma}$ is the variation of fluid Cauchy stress tensor, given by $\delta\boldsymbol{\sigma} = 2\mu\boldsymbol{\nabla}(\mathbf{w}^h)\mathbf{n} + q^h\mathbf{n}$, $[Q]_-$ denotes the negative part part of Q, which is, $[Q]_- = Q$ if $Q < 0$ and $[Q]_- = 0$ if $Q > 0$. h_n is the element length, C_I^B is small scalar to ensure stability. The sliding interface formulation may be also seen as a Discontinuous Galerkin method, where the continuity of the basis function is enforced everywhere in the interior of the two subdomains, but not at the sliding interface between them. The significance of each term is explained in detail in [33].

Such a procedure was originally developed in [33] in the context of Isogeometric Analysis (IGA) [75, 52] for computing flows about rotating components. The sliding-interface coupling was successfully applied on various challenging problem including offshore wind turbines [73, 94, 93, 34], hydraulic arresting gear [161] and Kayak propulsion [164]. For sliding interfaces in the space–time context, see the recent work in [143, 141].

Remark. Although the sliding interface is a cylinder in the application of tidal stream

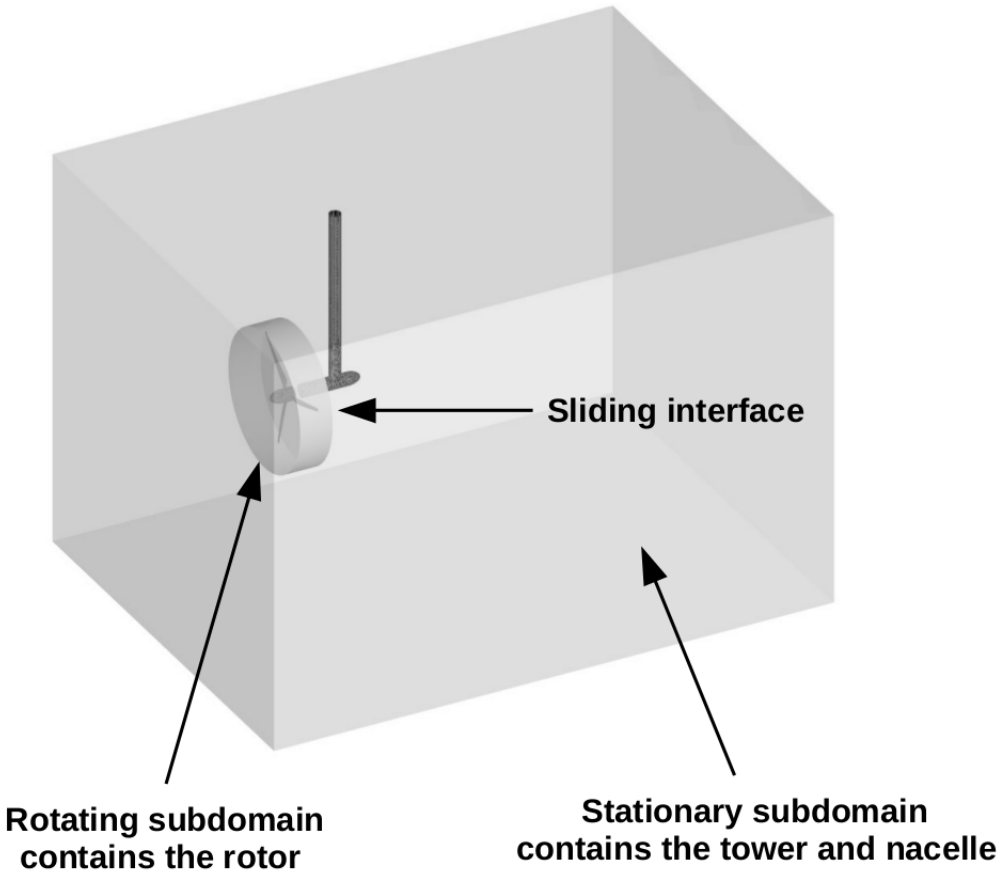

Figure 2.2: Fluid mechanics domain and sliding interface

turbines, the sliding interface technique allows any shape of the sliding interface, which will be seen in the application of Kayak propulsion using hydrofoils in tandem configuration in Chapter 6.1.4

Remark. Alternatively to the sliding-interface approach, the Shear-Slip Mesh Update Method [149, 45, 46] and its more general versions [150, 151] may also be used to handle objects in relative motion. A recently developed set of space-time (ST) methods can serve as a third alternative in dealing with objects in relative motion. The components of this set include the ST/NURBS mesh update method [140, 125], ST interface tracking with topology change [138], and ST computation technique with continuous representation in time [135].

2.2.6 Sliding interface technique for re-distancing

In presence of relative motions between components, sliding interface technique is also applied on re-distancing. The resulting semi-discrete form of re-distancing can be stated as: given ϕ, find ϕ^d, such that $\forall \eta$:

$$\begin{aligned}
&\boldsymbol{B}_{re}(\eta_d^h, \phi_d^h) - \boldsymbol{F}_{re}(\eta_d^h) \\
&- \sum_{b=1}^{Neb} \int_{\Gamma_t^{SI}} \eta_{s1} \left[\mathbf{a}_{s1} \cdot \mathbf{n}_s 1\right]_- (\phi_{s1} - \phi_{s2}) \, \mathrm{d}\Gamma \\
&- \sum_{b=1}^{Neb} \int_{\Gamma_t^{SI}} \eta_{s2} \left[\mathbf{a}_{s2} \cdot \mathbf{n}_s 2\right]_- (\phi_{s2} - \phi_{s1}) \, \mathrm{d}\Gamma = 0
\end{aligned} \tag{2.44}$$

The third line and fourth line of Eq. 2.44 come from the application of sliding interface technique on Eikonal equation. $[\mathbf{a} \cdot \mathbf{n}]_-$ denotes the inflow part with respect to the "effective" velocity $\mathbf{a}$.

Remark While level set convection is performed inside the Newton-iteration loop, level-set re-distancing is performed once per time step at the end of the multi-corrector stage. This is done from considerations of computational efficiency.

2.3 Acknowledgement

This chapter, in part, is a reprint of the materials as they appear in : “Computational free-surface fluid-structure interaction with applications on offshore floating wind turbines” (with A. Korobenko, X. Deng, Y. Bazilevs) *Computers and Fluids*, 2016. The dissertation author is the primary investigator and author of this paper.

Chapter 3

Applications: Free-surface simulations

In this chapter, we show two engineering applications of the proposed free-surface flow formulation. In Section 3.1, we solve the well-known CFD benchmark problem of solitary wave hitting a rigid and fixed cubic platform, which is a pure free-surface flow without sliding interface. The problem is solved on a fixed mesh and is used to validate the free-surface flow formulation. In Section 3.2, the free-surface formulation with sliding interface techniques on free-surface flows and re-distancing is applied on horizontal tidal stream turbines. The free-surface effect on tidal turbine performance subjected to different inflow conditions is investigated.

3.1 Solitary wave impacting a fixed and rigid platform

3.1.1 Computational setup

In this section, we perform the simulation of solitary wave pass a fixed, rigid platform, and compare the results with experimental data from [58]. The experimental setup including the piston-based wave generator and wave tank is depicted in Figure 3.1. The data from this experiment is often used to validate free-surface software for marine and offshore engineering applications, which we also do here.

The solitary wave may be derived from potential flow theory. A thorough derivation

may be found in [119]. In present work, a so-called second order solitary wave is adopted, with the analytical description given as

$$\phi = d\left[\epsilon \operatorname{sech}(q)^2 - \frac{3}{4}\epsilon^2 \operatorname{sech}(q)^2 \tanh(q)^2)\right] \tag{3.1}$$

$$u = \sqrt{gd}\left\{(\epsilon \operatorname{sech}(q)^2 + \epsilon^2 \operatorname{sech}(q)^2\left[\frac{1}{4} - \operatorname{sech}(q)^2 - \frac{3}{4}\left(\frac{s}{d}\right)^2 (2 - 3\operatorname{sech}(q)^2)\right]\right\} \tag{3.2}$$

$$v = 0 \tag{3.3}$$

$$w = \sqrt{gd}\epsilon\sqrt{3\epsilon}\left(\frac{s}{d}\right)\operatorname{sech}(q)^2 \tanh(q)\left\{1 - \epsilon\left[\frac{3}{8} + 2\operatorname{sech}(q)^2 + \frac{1}{2}\left(\frac{s}{d}\right)^2 (1 - 3\operatorname{sech}(q)^2)\right]\right\} \tag{3.4}$$

where g is the gravity acceleration magnitude, (u, v, w) is the fluid velocity vector, ϕ is the wave elevation, d is the still water depth, H is the wave height, $\epsilon = \frac{H}{d}$, $c = \sqrt{gd}\left(1 + \frac{1}{2}\epsilon - \frac{3}{20}\epsilon^2\right)$ is the wave speed, $q = \frac{\sqrt{3\epsilon}}{2d}\left(1 - \frac{5}{8}\epsilon\right)(x - ct)$, $s = z + d$, and z is the distance from the still water in normal direction. The air-water interface in the hydrostatic configuration is assumed to be located at $z = 0$. The wave condition in this simulation is chosen as follows: $d = 0.234696$ m, $\epsilon = \frac{H}{d} = 0.42$, and zero clearance between the bottom of the platform and still water level.

The computational domain of the problem is defined as follows. The computational domain is a box with the dimensions of 10 m $\times$ 1 m $\times$ 2 m. A refined box is created to better capture the air-water interface evolution. The top and bottom surface of the refined box are 0.15 m above and below the still wave. The platform is a box with the dimensions of 1.524 m $\times$ 0.4 m $\times$ 0.3 m. The front surface is located at 5 m away from the inlet boundary, and the bottom surface is coincident with the still water level. A snapshot of the mesh is shown in Figure 3.2 and the mesh statistics are given in Table 6.7 and Table 3.2.

Zero wind speed is assumed in air domain. The solitary wave profile with the above parameters is initialized in the water domain. The wave peak is 3 m away from the front face the platform, as shown in Figure 3.3. After initialization, Navier-Stokes and level set equations are advanced with in time with $\Delta t = 0.0005s$. The boundary conditions are specified as follows: No penetration boundary conditions are set at the inlet, lateral, top and

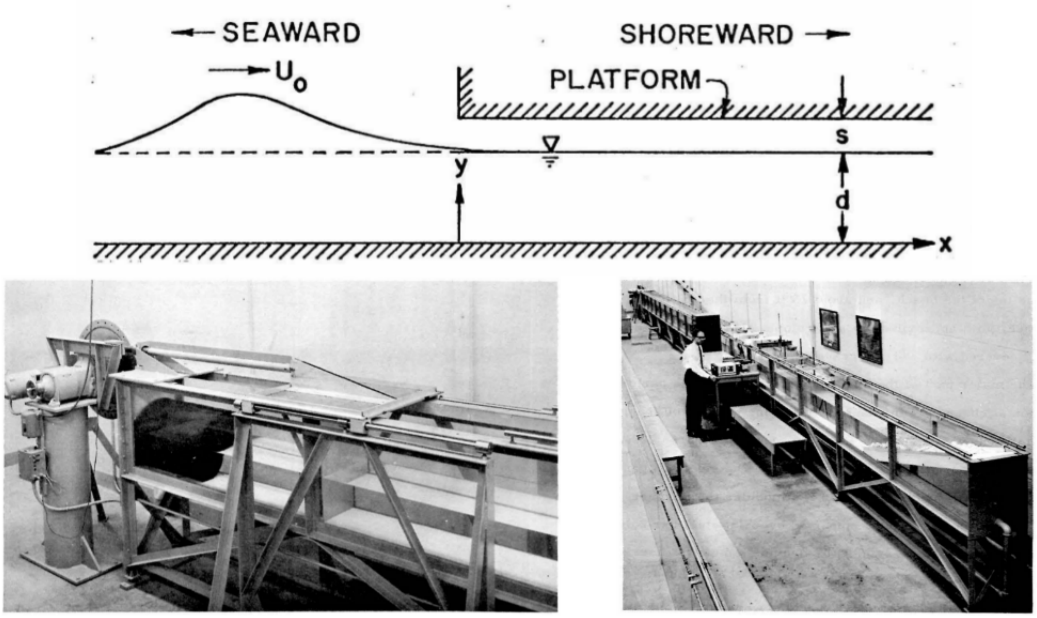

Figure 3.1: Experimental setup of solitary wave hitting a cubic platform [58]

Table 3.1: Number of nodes and elements

	Num. of nodes	Num. of elements
Mesh	2,939,731	16,995,741

bottom surfaces. Traction boundary conditions consistent with the hydrostatic pressure are applied at the outlet. Weak no-slip boundary conditions are imposed on the platform surface. The simulation is run until the wave fully passed the platform.

3.1.2 Numerical results

Figure 3.4 shows the deformed free-surface colored by the flow speed as the solitary wave is passing the platform, showing the qualitative behavior of the flow. Figure 3.5 shows the location of the two pressure sensors installed to record the experimental pressure time history as the wave passes the platform. In Figure.3.6, normalized pressure time history produced in the computation in plotted together with the experimental data. The two quantities are in close agreement, giving us some confidence to proceed with more complex simulations presented in the sequel.

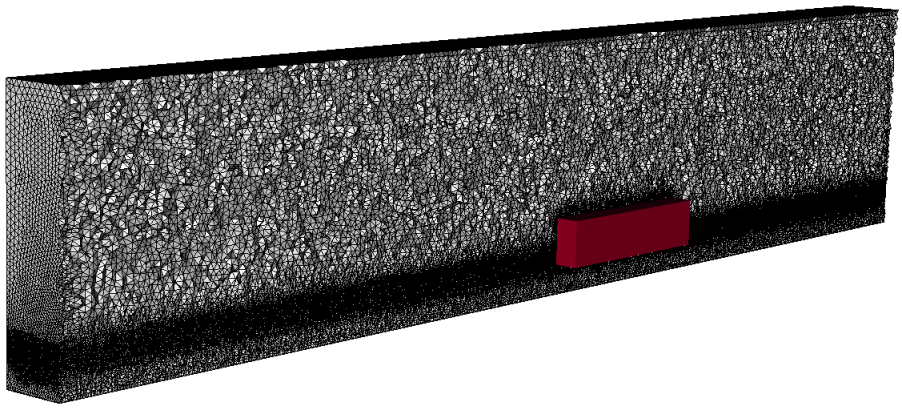

Figure 3.2: Computational domain of solitary wave hitting a cubic platform

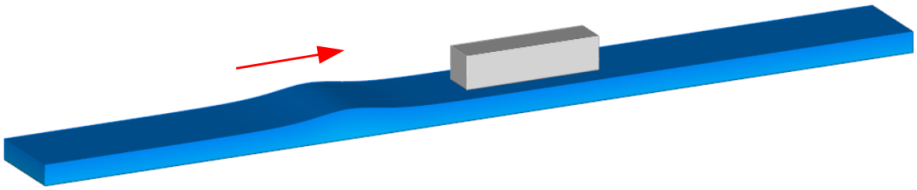

Figure 3.3: Computational setup of solitary wave hitting a cubic platform

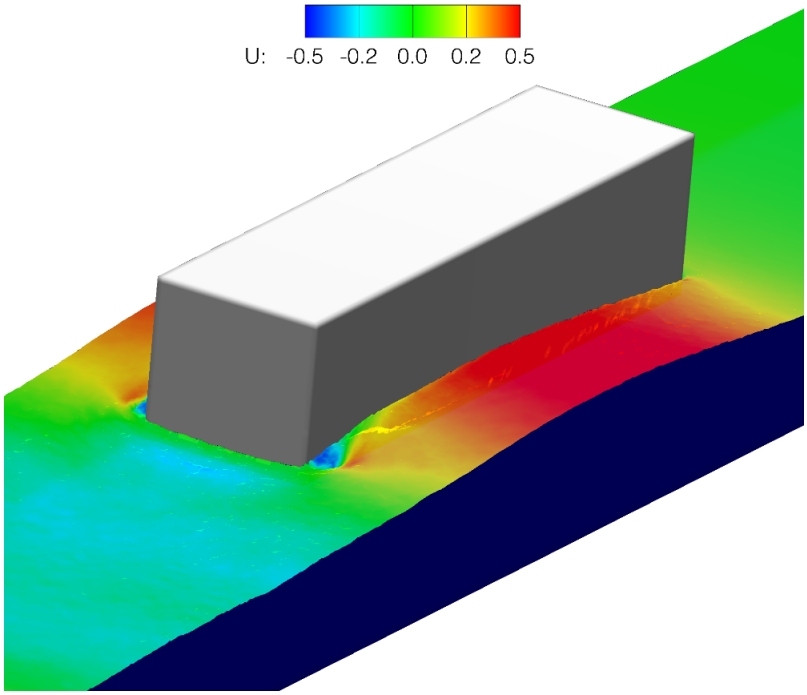

Figure 3.4: Snapshot of free-surface colored by flow speed in (m/s)

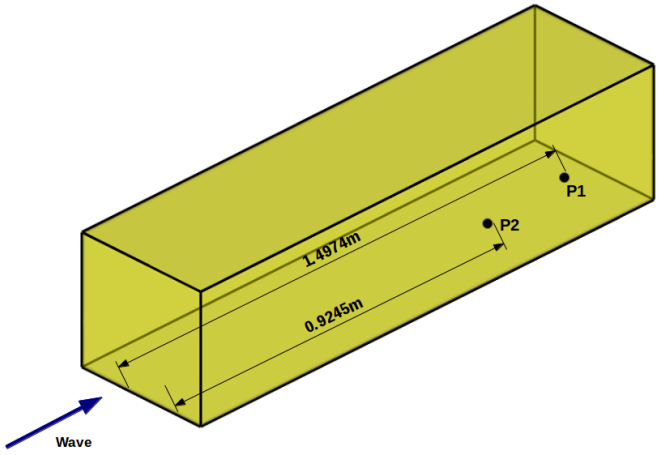

Figure 3.5: Location of two sensors

Table 3.2: Element length

Top surface	Bottom surface	Refine box	Platform
0.05 m	0.024 m	0.012m	0.012 m

3.2 Free-surface simulations of horizontal axis tidal stream turbines

Current research on horizontal axis tidal stream turbines (HATTs) is focused on increasing the effectiveness of power generation, reducing the environmental impacts, and designing the tidal turbine farms. Among these areas, improving the power generation performance is of the first priority and attracts the most attention. Numerous computational and experimental approaches have been proposed to accurately predict the hydrodynamic performance of tidal stream turbines [13, 14, 15, 10, 11]. HATTs use the same mechanical principles as horizontal-axis wind turbines. Although a lot of technologies can be borrowed from wind energy industry, there are a number of fundamental differences between wind turbines and tidal stream turbines. These differences include different fluid properties, free-surface effect and the possible occurrence of cavitation.

Traditionally, reduced order numerical techniques, such as the vortex element method and the blade element momentum method, have been used to predict the performance of tidal

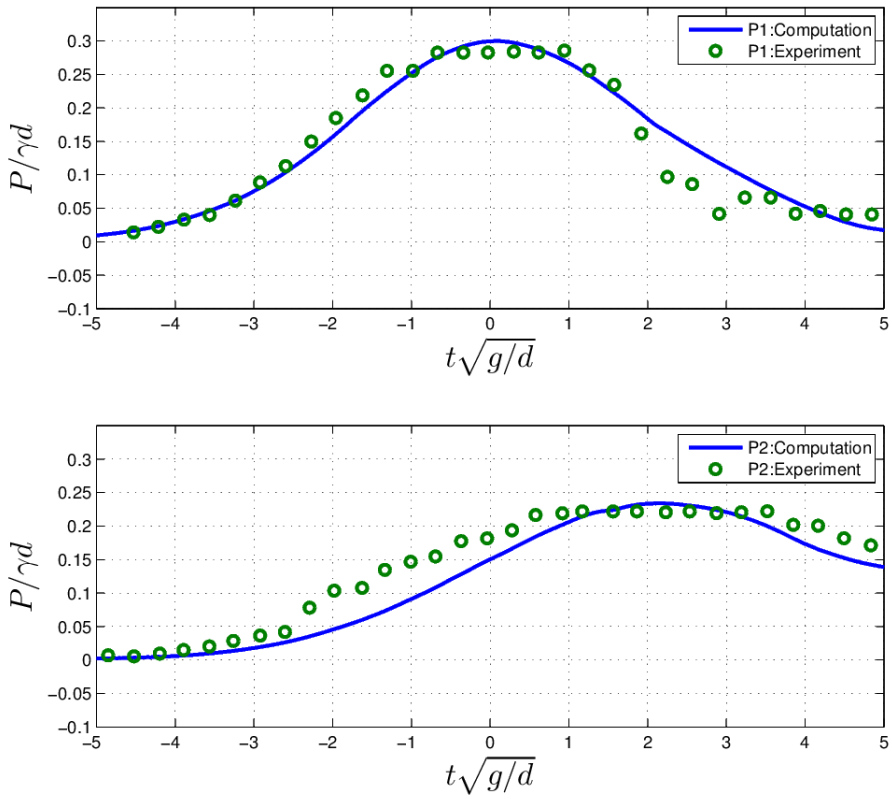

Figure 3.6: Time history of normalized pressure, where γ is water weight

stream turbines [100, 12, 102, 106, 108]. Although results from these numerical simulations were shown to be in good agreement with experimental measurements, the aforementioned methods rely on empirical correlations and may not be suitable for a wide range of operating conditions. Furthermore, due to the computational challenges involved, only a few of these numerical simulations consider the free-surface effect, as shown in the experimental studies of [9, 8], which can significantly affect the performance of tidal stream turbines. Finally, the analyses presented focused on the rotor only, without taking into account the other turbine components, such as the tower and nacelle.

In this section, the proposed computational free-surface flow framework is adopted to perform 3D, time-dependent free-surface simulations of HATTs, aiming to investigate the free-surface effect on the performance of tidal stream turbines. In order to account for presence of tower and nacelle thus enabling simulations of the so called "full machine", the sliding interface technique in Navier-Stokes, level set and re-distancing are activated in the simulations.

In the next sections, the geometry modeling of the tidal turbine is introduced first. Then pure hydrodynamics simulation and free-surface simulations of the tidal stream turbine subjected to uniform flow and Airy waves with different tip immersions are performed.

3.2.1 Tidal turbine geometry

The tidal turbine rotor used in current simulations is taken from from [9], which is a three-blade design with 20° hub pitch angle. The turbine rotor is widely used for validation of numerical methods for tidal energy, largely because of the availability of experimental data characterizing its hydrodynamic performance in the presence of the free surface [9, 8]. The rotor consists of three blades with diameter D = 0.8 m. There are 17 stations along each blade and are interpolated from 2D coordinated-based data from NACA 63-812, NACA 63-815, NACA 63-818, NACA 63-821 and NACA 63-824. To form a 3D twisted blade, these NACA profiles are given different chord, thickness and pitch angle, much like is done in the case of wind-turbine blades [23, 27, 147, 128, 142]. The detailed characteristics are listed in Table 3.3. The CAD model of the whole rotor with 3 blades is shown in Fig 3.7.

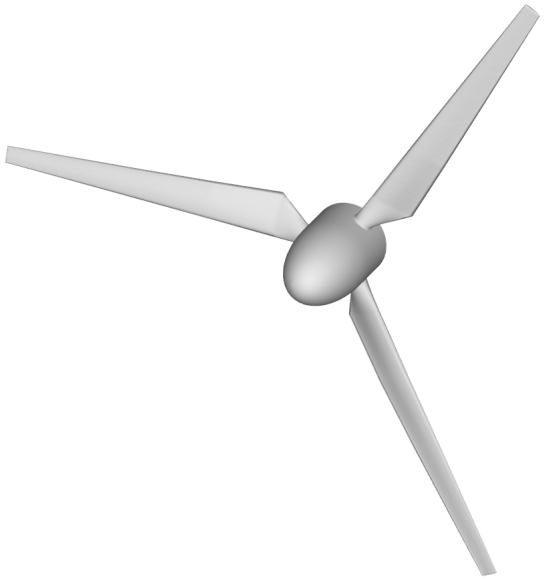

Figure 3.7: Turbine rotor with 3 blades with 20° hub pitch angle

Table 3.3: Blade profile specifications

r/R	Radius (mm)	c/R	Pitch angle (deg)	t/c (%)
0.2	80	0.125	20	24
0.25	100	0.1203	17.1	22.5
0.3	120	0.1156	14.5	20.7
0.35	140	0.1109	12.6	19.5
0.4	160	0.1063	11.1	18.7
0.45	180	0.1016	9.9	18.1
0.5	200	0.0969	8.9	17.6
0.55	220	0.0922	8.1	17.1
0.6	240	0.0875	7.4	16.6
0.65	260	0.0828	6.9	16.1
0.7	280	0.0781	6.5	15.6
0.75	300	0.0734	6.2	15.1
0.8	320	0.0688	5.9	14.6
0.85	340	0.0641	5.6	14.1
0.9	360	0.0594	5.4	13.6
0.95	380	0.0547	5.2	13.1
1.0	400	0.05	5	12.6

3.2.2 Uniform inflow condition

For uniform inflow conditions, we perform both pure hydrodynamics simulations and free-surface simulations. In the context of present work, pure hydrodynamics simulation means the whole tidal turbine is fully immersed into the water domain and free-surface effect is neglected. The computational domain of the pure hydrodynamics simulation is a box with dimensions 4.35 m $\times$ 2.8 m $\times$ 2.64 m. A refined cylinder with length of 2 m and radius of 0.5 m is designed to capture the turbulent wake generated by the turbine. As shown in Fig 3.8, the domain is divided into two subdomains separated by a cylinder-shaped sliding interface, the surface mesh of which is shown Fig 3.9. The volume mesh makes use of triangular prisms in the rotor boundary layers and tetrahedra elsewhere. The planar cut of the three dimensional mesh is shown in Fig 3.8. The mesh statistics and element length employed in pure hydrodynamics simulation are summarized in Table 3.4 and Table 3.5.

The computational domain of the free-surface simulations is also a box with dimensions 6.6 m $\times$ 2.8 m $\times$ 4.14 m. The sliding interfaces and refined cylinder for capturing wake are taken from the pure hydrodynamics simulation mesh and employed here again. In addition, as shown in Fig. 3.10, another refined box is built around the still water level to better resolve the free-surface evolution. The mesh statistics and element length employed in free-surface simulations are summarized in Table 3.6 and Table 3.7.

Boundary conditions in the computations are specified as follows. For the pure hydrodynamics simulation, uniform inflow velocity is imposed strongly at the inlet; The outlet is open to the hydrostatic-pressure boundary conditions; No-penetration boundary condition is applied on the remaining outer surfaces of the computational domain. For the free-surface simulations, zero wind velocity is applied strongly on the air portion of the inlet, while the desired uniform flow velocity is applied strongly on the water portion of the inlet; the level-set field is also prescribed strongly on the inlet boundary as a linear function of the vertical coordinate. The zero of this function defines the location of the air-water interface; The top and outlet surfaces are open to the hydrostatic-pressure boundary conditions; No-penetration boundary condition is applied on the lateral and bottom outer surfaces of the computational domain. Backflow stabilization [22, 110] is employed on

all surfaces where normal velocity is left unspecified. For both pure hydrodynamics and free-surface simulations, the weak enforcement of essential boundary conditions are adopted at the fluid-turbine interface. All the computations are carried out in a parallel computing environment. The mesh is partitioned into 256 subdomains using METIS [84], and each subdomain is assigned to a computing core. The time step is set to 1×10^{-4} s.

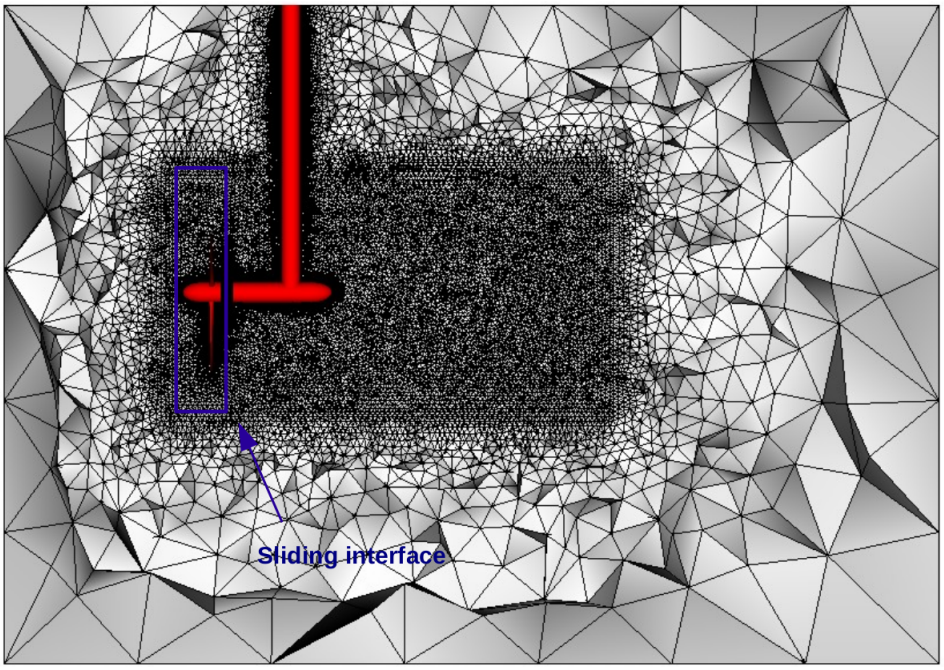

Figure 3.8: A 2D cut of the computational domain at y = 0 to show the mesh quality used in pure hydrodynamics simulation. The mesh is refined in the inner region for better flow resolution near the tidal stream turbine

Table 3.4: Mesh statistics of pure hydrodynamics simulations

Num. of nodes	Num. of elements
709,143	3,660,467

Table 3.5: Element length employed for pure hydrodynamics simulations (in m)

Outer box	Refined box for wake	Turbine
0.5	0.02	0.0001

For uniform inflow conditions, the operation parameters are set as follows. Angular rotational speed is set to Ω =28.1250 rad/s and mean inflow water speed is set to U_0 =1.5

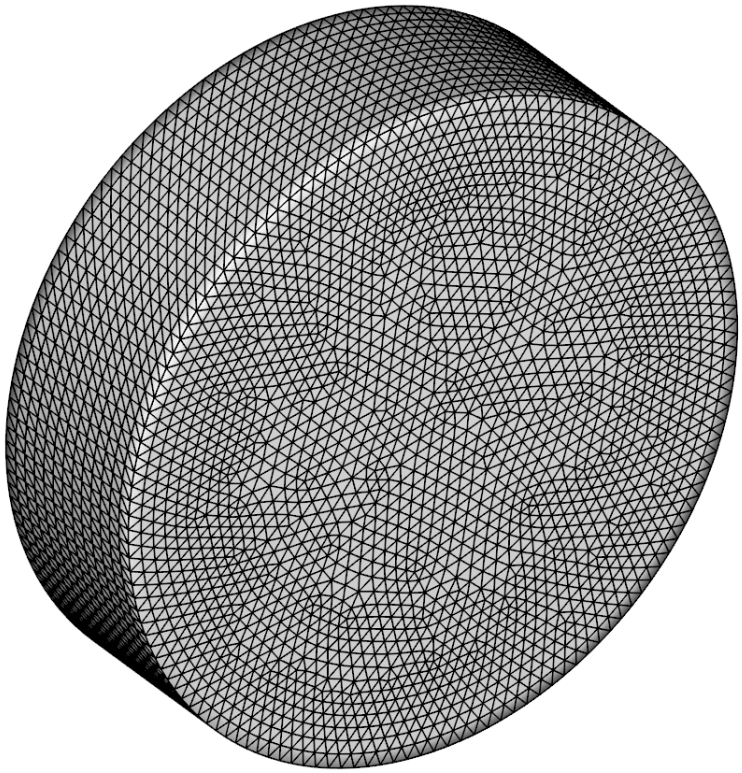

Figure 3.9: Triangular mesh of the sliding interface

Table 3.6: Mesh statistics of free-surface simulations

Num. of nodes	Num. of elements
1,339,891	7,389,215

Table 3.7: Element length employed for free-surface simulations (in m)

Outer box	Refined box for wake	Refined box for free-surface	Turbine
0.5	0.02	0.03	0.0001

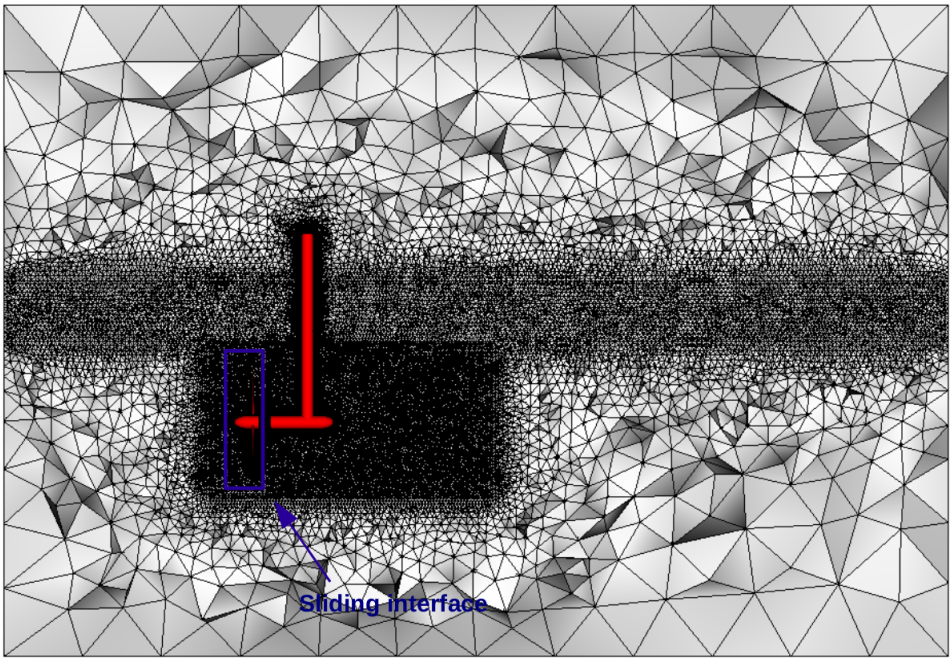

Figure 3.10: A 2D cut of the computational domain at y = 0 to show the mesh quality used in free-surface simulations. Two refined regions are built to better capture the turbulent wake and free-surface evolution

m/s. For uniform inflow conditions, we perform one pure hydrodynamics simulation and two free-simulations with deep tip immersion of $0.55D$ and shallow tip immersion of $0.19D$. An illustration of the computational set-up can be found in Fig 3.11.

Through the simulations, we measured the thrust coefficient C_T and power coefficient C_P, which are given by

$$C_T = \frac{4F}{0.5\rho_w \pi D^2 {U_0}^2} \tag{3.5}$$

and

$$C_P = \frac{4T\Omega}{0.5\rho_w \pi D^2 {U_0}^3} \tag{3.6}$$

where F and T are the thrust and torque respectively. The time history of C_T and C_P compared with experimental data from [9] is shown in Fig 3.12.

The predicted C_T and C_P from free-surface simulations agree with the experimental

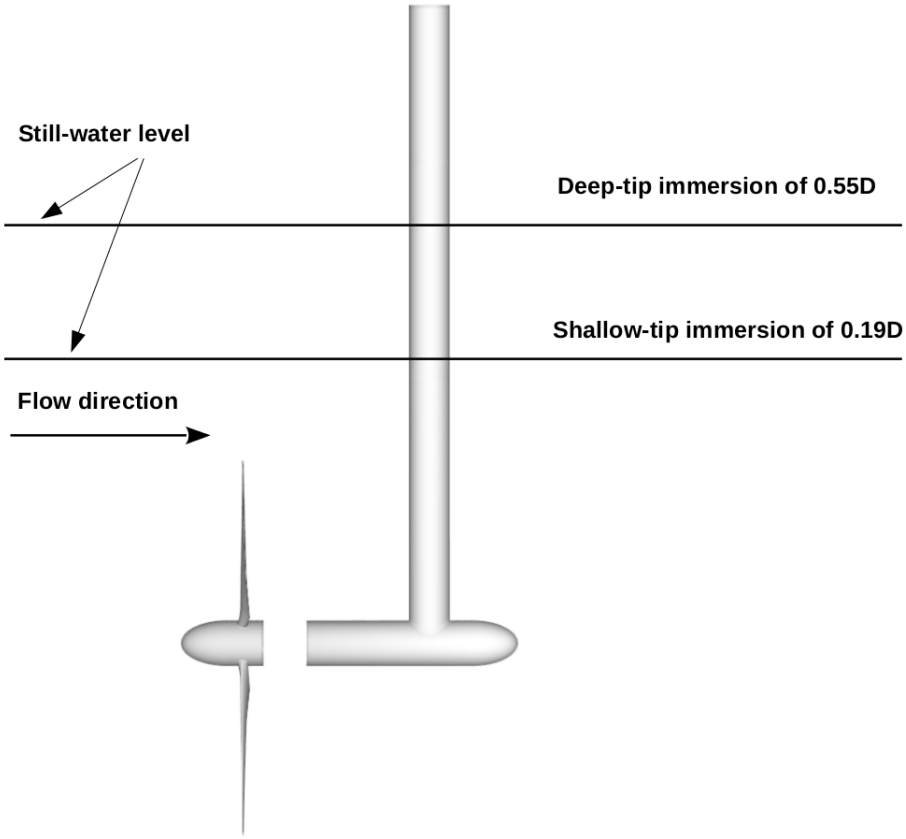

Figure 3.11: Computational set-up

data excellently for both shallow tip immersion case and deep tip immersion case. One important trend, which is observed in the experiment [9] and reproduced in the current computations, is that the C_T and C_P are higher in deep immersion case than those in shallow tip immersion case. We can also see the values of C_T and C_P produced by pure hydrodynamics simulation are close to the free-surface simulation results of deep tip immersion but are bigger than free-surface results of shallow tip immersion, which means the tidal stream turbine barely feel the presence of free-surface in the case of deep tip immersion, while the presence of free-surface significantly reduce the thrust and power coefficients in the case of shallow tip immersion. The results indicate that the free-surface effect is non-negligible for the shallow-tip immersion case.

Fig 3.13 (left) shows the velocity magnitude contour of planar cut for the pure hydrodynamics simulation case, while Fig 3.13 (right) shows the vorticity isosurfaces colored by velocity magnitude. It is noted that the solution fields are quite continuous across the sliding interfaces, which indicates that the sliding-interface technique is successful for the present application.

Fig 3.14 shows the flow filed with vorticity isocontours and air-water interface, colored by the velocity magnitude, for both deep- and shallow-tip immersion free-surface simulations. In both deep tip immersion and shallow tip immersion cases, the air-water interfaces experiences strong topological changes after the flow impacts the tower. We also observed that, in the wake of the tower, shallow tip immersion case generated much deeper dent right behind the tower than deep tip immersion case did, which is not surprising, because interaction between free-surface and turbine is much stronger in shallow tip immersion case, resulting in more deformation of the air-water interface. This observation also explains the more pronounced free-surface effect on the thrust and power coefficients in that case.

3.2.3 Airy wave inflow condition

In this section, the performance of the same tidal stream turbine subjected to regular wave inflow condition is investigated. The simulations presented in this section are outside of the range of experimental data for the tidal turbine considered, and show the versatility of

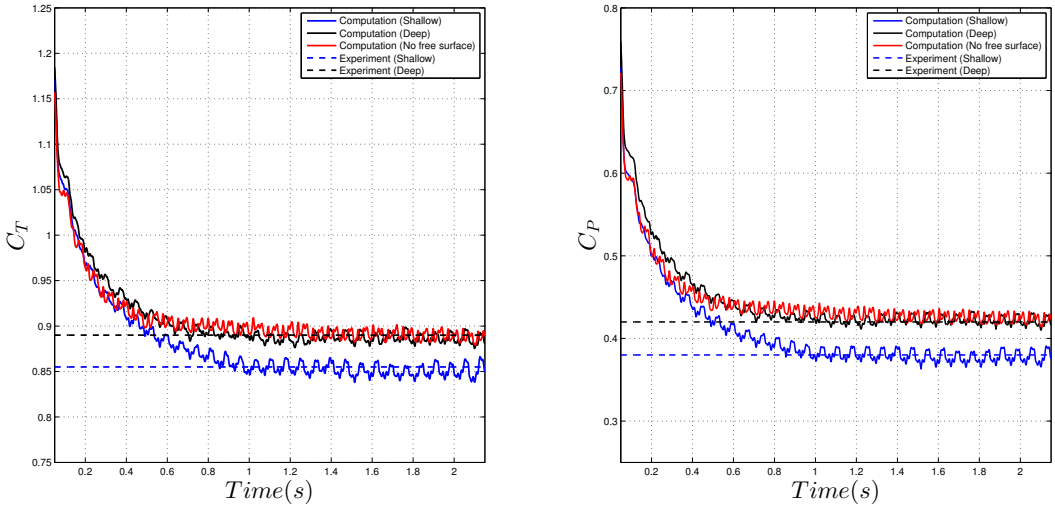

Figure 3.12: Time history of thrust and power coefficients for uniform inflow conditions

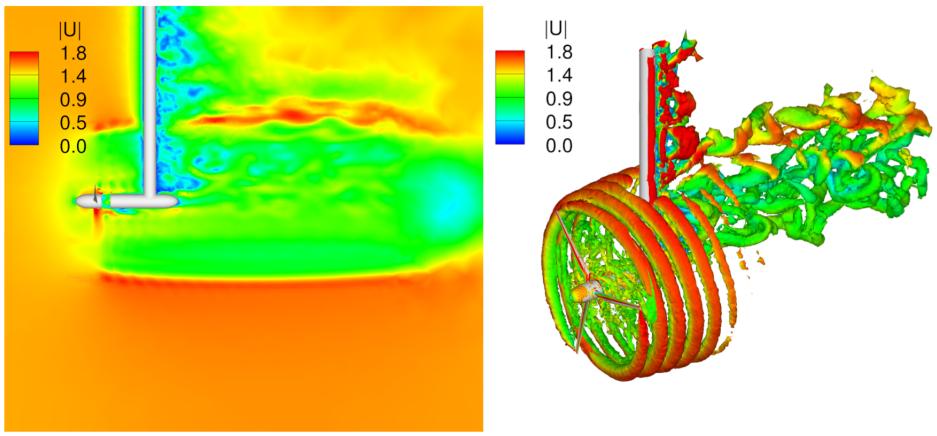

Figure 3.13: Pure hydrodynamics simulation. Left: Velocity field at a planar cut. Right: Vorticity contour colored by velocity magnitude (in m/s)

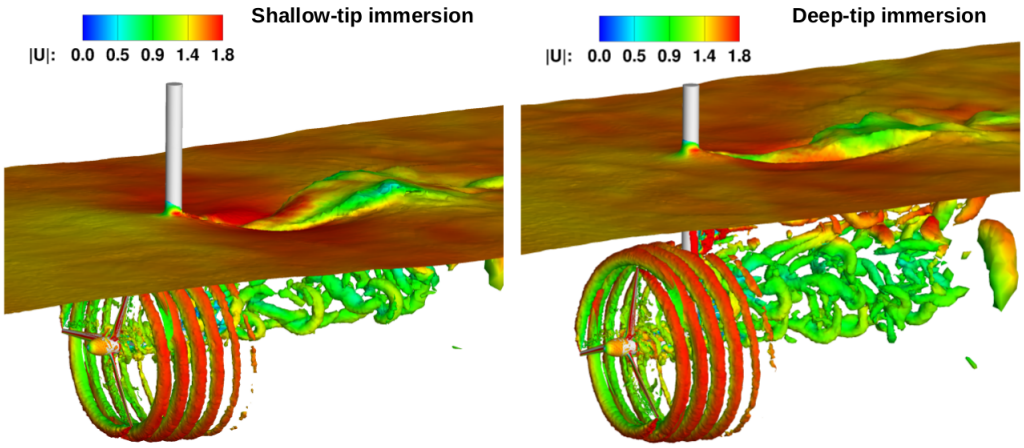

Figure 3.14: Snapshots of air-water interface and underwater vorticity colored by velocity magnitude (in m/s) of free-surface simulation. Shallow tip immersion (left). Deep tip immersion (right)

the free-surface flow framework employed. In order to generate the waves, we make use of Airy wave theory, which may be derived using potential flow theory, and specified as follows: Given the wave amplitude A, wave length L, mean flow speed U_0 and water depth h, we compute wavenumber $k = \frac{2\pi}{L}$ and wave phase speed $\omega = \sqrt{gk\tanh(kh)} + kU_0$. With these definitions, the Airy wave profile is given by

$$\phi = A\cos(kx - \omega t) + h - z \tag{3.7}$$

$$u = \frac{wA}{\sinh(kh)}\cosh(kz)\cos(kx - \omega t) + U_0 \tag{3.8}$$

$$v = 0 \tag{3.9}$$

$$w = \frac{wA}{\sinh(kh)}\sinh(kz)\sin(kx - \omega t) \tag{3.10}$$

where (u, v, w) is the velocity field and U_0 is the mean flow speed. Based on the theory, velocity fluctuation is higher close to the free-surface, and the Airy wave gradually reduce to uniform flow profile with depth (See Figure 3.15 for the structure of Airy wave). In current simulations, we set $U_0 = 1.5$ m/s, $H = 0.085$ m and $L = 2.4$ m. The corresponding

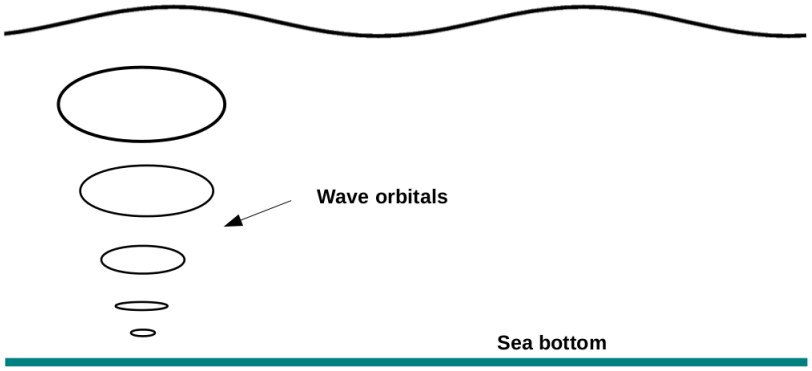

Figure 3.15: Fluid motion of Airy wave

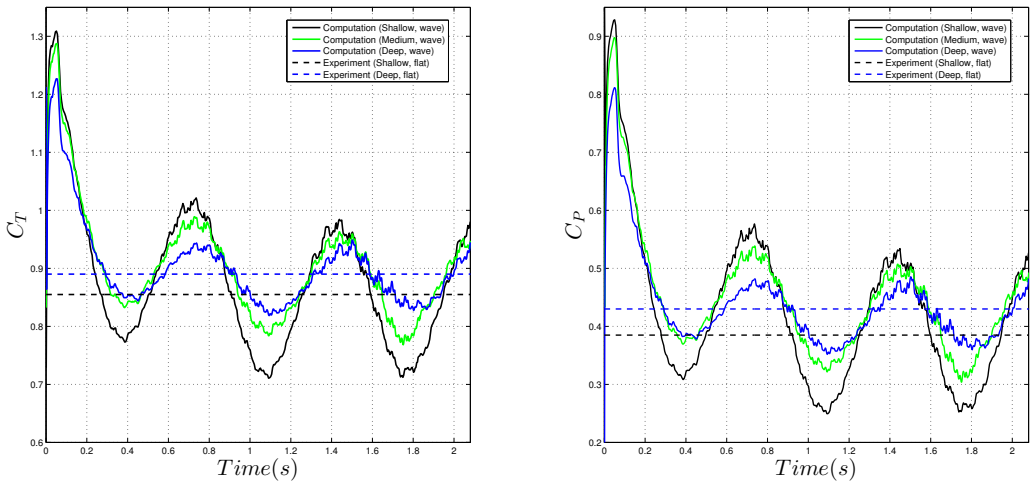

Figure 3.16: Time history of thrust and power coefficients of Airy wave conditions

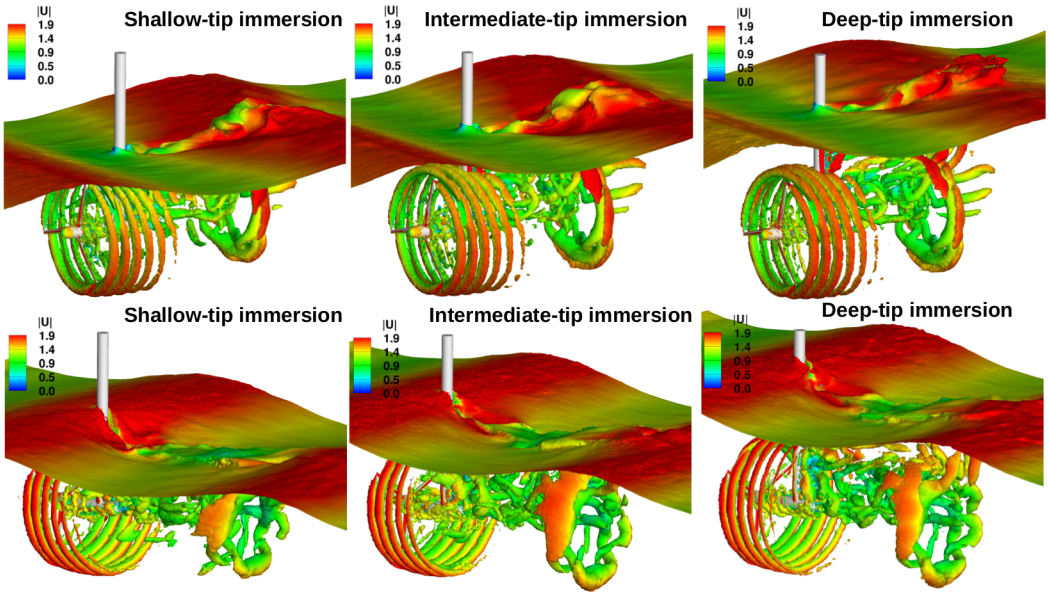

Figure 3.17: Snapshots of free-surface and vorticity colored by velocity magnitude (in m/s) of free-surface simulations with Airy wave inflow conditions

wave period $T = \frac{2\pi}{\omega}$ is 0.6985 s. The angular rotational speed is also set to $\Omega = 28.1250$ rad/s. The wave profile with the parameters given above is strongly imposed at the inlet. The problem domain, mesh, time-step size, and remaining boundary conditions are the same as in the previous section.

Three free-surface simulations with the deep tip immersion of 0.55D, shallow tip immersion of 0.19D and medium-tip immersion of 0.37D are performed. The time history of C_T and C_P are plotted in Fig 3.16. The experimental results of flat inflow conditions are also plotted as references. Because the turbine is now subjected to wave action, the thrust and power coefficients exhibit time-periodic behavior that is consistent with the wave frequency. Due to the structure of Airy waves, we observe higher-amplitude fluctuation of $\overline{C}_T$ and $\overline{C}_P$ as the turbine is placed closer to the water surface. The averaged $\overline{C}_T$ and $\overline{C}_P$ based on fully developed flow stage are listed in Table 3.8. We see higher maximum values and higher fluctuation of C_T and C_P as the turbine are placed closer to the Airy wave surface. However, the averaged values, $\overline{C}_T$ and $\overline{C}_P$, decrease as the turbine is placed closer to the free-surface, which is consistent with previous uniform inflow simulations. As can be seen, the average values of medium tip immersion case and deep tip immersion case are very

close which suggests the existence of a minimum immersion depth at which HATTs will operate to their full potential.

Table 3.8: $\overline{C}_T$ and $\overline{C}_P$ of free-surface simulations subjected to Airy wave inflow conditions

Cases	$\overline{C}_T$	$\overline{C}_P$
Shallow tip immersion	0.8513	0.3919
Medium tip immersion	0.8741	0.4141
Deep tip immersion	0.8794	0.4144

Fig 3.17 shows the flow field with vorticity isosurfaces and the air-water interface colored by velocity magnitude for the three immersion cases, illustrating the complexity of the underlying hydrodynamics and motivating the use of advanced free-surface modeling for the present application.

3.3 Summary

The proposed computational free-surface flow framework that enables 3D, time-dependent free-surface simulations for real-world engineering problems. We first validated the framework with the benchmark problem of solitary wave impacting a rigid and fixed platform. Then the free-surface formulation was applied on tidal energy. The performance of horizontal axis tidal turbines subjected free-surface flows is studied. The rotor-tower interaction is handled by means of the sliding-interface formulation, while the free-surface modeling makes use of the level-set technique, which includes a so-called re-distancing step. In the present work we extend the sliding-interface methodology to include re-distancing, which enables the computation of cases where free surface crosses the sliding interface, as shown in Fig. 3.18. The presented computational free-surface flow framework was deployed on a complex-geometry HATT with rotor diameter of 0.8 m. The framework was validated for the cases of uniform flow. In particular, the simulations, without any empiricism, were able to accurately capture the effect of the free surface on the rotor hydrodynamic loading. To illustrate the versatility of the approach, additional computations were carried out where

the HATT was subjected to more realistic Airy wave action. These computations revealed the presence of a minimum immersion depth for optimal operation.

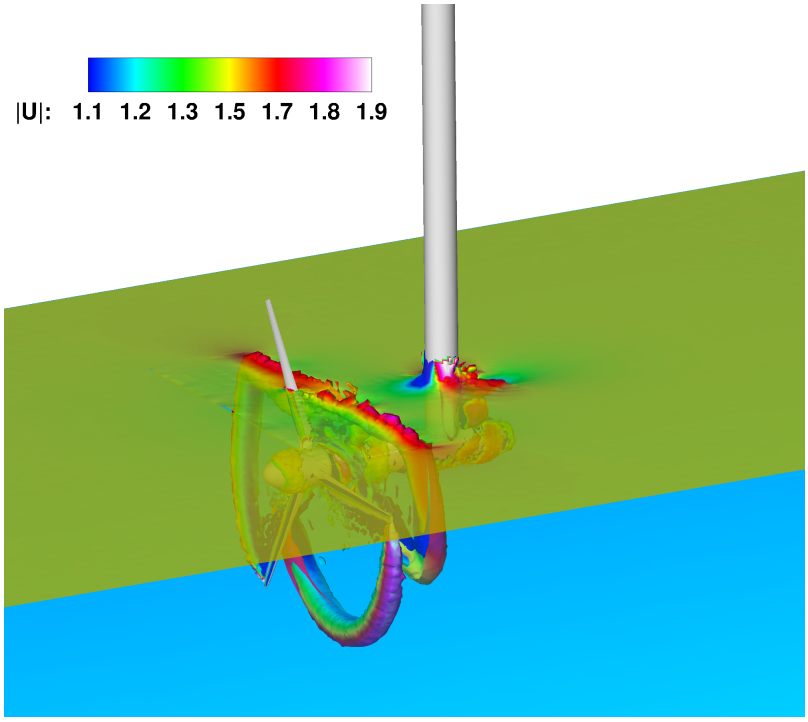

Figure 3.18: Illustration of a scenario in which the free surface crosses the sliding interface. HATT simulation is carried out wherein rotor blades pierce the water surface. Free surface exhibits a relatively smooth transition across the sliding interface

3.4 Acknowledgement

This chapter, in part, is a reprint of the materials as they appear in : "Computational free-surface fluid-structure interaction with applications on offshore floating wind turbines" (with A. Korobenko, X. Deng, Y. Bazilevs) *Computers and Fluids*, 2016 and "Free-surface flow modeling and simulation of horizontal-axis tidal-stream turbines" (with X. Deng, A. Korobenko, Y. Bazilevs) *Computers and Fluids*, 2016. The dissertation author is the primary investigator and author of these papers.

Chapter 4

Structural mechanics

4.1 Governing equations of structural mechanics

The governing equations of structural mechanics written in the Lagrangian frame [47] consist of the local balance of linear momentum, and are given by

$$\rho_2 \left(\frac{\mathrm{d}^2 \boldsymbol{d}}{\mathrm{d}t^2} - \boldsymbol{f}_2 \right) - \boldsymbol{\nabla} \cdot \boldsymbol{\sigma}_2 = \mathbf{0} \tag{4.1}$$

where ρ_2 is the structural density, $\boldsymbol{f}_2$ is the structural body force per unit mass, $\boldsymbol{\sigma}_2$ is the structural Cauchy stress, and $\boldsymbol{d}$ is the unknown structural displacement vector. Eq. 4.1 is the strong form governing equations of structural mechanics. The variational (weak) form and the dicretization using IGA will be introduced next.

For structural mechanics, we use the principle of virtual work as the starting point to derive the variational (weak) form of the structural mechanics. Let $\mathcal{V}_s^h$ and $\mathcal{W}_s^h$ denote the discrete trial and test function sets for the structural mechanics problem. The weak form of structural mechanics reads: find $\boldsymbol{d}^h \in \mathcal{V}_s^h$, such that $\forall \mathbf{w}_s^h \in \mathcal{W}_s^h$,

$$\int_{\Omega_0^s} \boldsymbol{w}_s^h \cdot \rho_s \left(\frac{d^2 \boldsymbol{d}^h}{dt^2} - \mathbf{f}_s \right) \mathrm{d}\Omega + \int_{\Omega_0^s} \delta \boldsymbol{E}^h : \boldsymbol{S}^h \, \mathrm{d}\Omega - \int_{\Gamma_0^s} \boldsymbol{w}_s^h \cdot (\Pi^h \mathbf{t}_f^h) \, \mathrm{d}\Gamma = 0 \tag{4.2}$$

where Ω_0^s is the structure domain in the reference configuration, $\boldsymbol{d}^h$ is the structural dis-

placement, ρ_s is the structural density, $\boldsymbol{E}^h$ is the Green-Lagrangian strain tensor, $\delta\boldsymbol{E}^h$ is the corresponding variation, $\boldsymbol{S}$ is the second Piola-Kirchhoff stress, $\mathbf{f}_s$ is the structural body force per unit structural mass, $\boldsymbol{t}_f$ is the discrete fluid traction, Π^h is a L^2 projection operator onto the space spanned by the basis functions of the structural mechanics problem restricted to the fluid-structure interface. $\boldsymbol{S}$ is defined as a St. Venant-Kirchhoff material model, namely, $\boldsymbol{S}(\boldsymbol{E}) = \boldsymbol{C} : \boldsymbol{E}$, where $\boldsymbol{C}$ is the a fourth tensor of elastic moduli that is independent of the state of deformation. The above formulation is simplified by using the kinematic assumptions of isogeometric rotation-free shell developed in [89] and beam/cable developed in [115]. As a result, we obtain the following two variational formulations for shell and beam/cable.

4.2 Isogeometric rotation-free shell formulation

In the case of shells, the 3D continuum description is reduced to that of the shell mid-surface, and the transverse normal stress is neglected. Furthermore, the Kirchhoff-Love theory assumes that the shell director remains normal to its middle surface during the deformation, which implies that the transverse shear strains are zero. As a result, only in-plane stress and strain components are considered. Let $\alpha = 1, 2$ and $\beta = 1, 2$ denote their components. Let Γ_0^s and Γ_t^s denote the shell mid-surface in the reference and deformed configurations, respectively. Furthermore, let h_{th} denote the shell thickness and $\xi_3 \in [-\frac{h_{th}}{2}, \frac{h_{th}}{2}]$ denote the through-thickness coordinate.

We make use of the following standard shell kinematic quantities and relationships (see [88, 89])

$$E_{\alpha\beta} = \varepsilon_{\alpha\beta} + \xi_3 \kappa_{\alpha\beta} \tag{4.3}$$

$$\varepsilon_{\alpha\beta} = \frac{1}{2}(\boldsymbol{g}_\alpha \cdot \boldsymbol{g}_\beta - \boldsymbol{G}_\alpha \cdot \boldsymbol{G}_\beta) \tag{4.4}$$

$$\kappa_{\alpha\beta} = -\frac{\partial \boldsymbol{g}_\alpha}{\partial \xi_\beta}\boldsymbol{g}_3 - (-\frac{\partial \boldsymbol{G}_\alpha}{\partial \xi_\beta}\boldsymbol{G}_3) \tag{4.5}$$

$$\boldsymbol{g}_\alpha = \frac{\partial \boldsymbol{x}}{\partial \xi_\alpha} \tag{4.6}$$

$$\boldsymbol{G}_\alpha = \frac{\partial \boldsymbol{X}}{\partial \xi_\alpha} \tag{4.7}$$

$$\boldsymbol{g}_3 = \frac{\boldsymbol{g}_1 \times \boldsymbol{g}_2}{\|\boldsymbol{g}_1 \times \boldsymbol{g}_2\|} \tag{4.8}$$

$$\boldsymbol{G}_3 = \frac{\boldsymbol{G}_1 \times \boldsymbol{G}_2}{\|\boldsymbol{G}_1 \times \boldsymbol{G}_2\|} \tag{4.9}$$

$$\boldsymbol{G}^\alpha = (\boldsymbol{G}_\alpha \cdot \boldsymbol{G}^\beta)^{-1}\boldsymbol{G}^\beta \tag{4.10}$$

where, $E_{\alpha\beta}, \varepsilon_{\alpha\beta}$ and $\kappa_{\alpha\beta}$ are the contravariant components of the in-plane Green-Lagrange strain, membrane strain and curvature tensors, respectively. The spatial coordinates of the shell mid-surface in the current and reference configurations are $\boldsymbol{x} = \boldsymbol{x}(\xi_1, \xi_2)$ and $\boldsymbol{X} = \boldsymbol{X}(\xi_1, \xi_2)$, parameterized by ξ_1 and ξ_2. The covariant surface basis vectors in the current and reference configurations are $\boldsymbol{g}_\alpha$ and $\boldsymbol{G}_\alpha$. The unit outward normal vectors to the shell mid-surface in the current and reference configurations are $\boldsymbol{g}_3$ and $\boldsymbol{G}_3$. The contravariant surface basis vectors in the reference configuration are denoted by $\boldsymbol{G}^\alpha$.

The local Cartesian basis vectors are selected as

$$\bar{\boldsymbol{e}}_1 = \frac{\boldsymbol{G}_1}{\|\boldsymbol{G}_1\|} \tag{4.11}$$

$$\bar{\boldsymbol{e}}_2 = \frac{\boldsymbol{G}_2 - (\boldsymbol{G}_2 \cdot \bar{\boldsymbol{e}}_1)\bar{\boldsymbol{e}}_1}{\|\boldsymbol{G}_2 - (\boldsymbol{G}_2 \cdot \bar{\boldsymbol{e}}_1)\bar{\boldsymbol{e}}_1\|} \tag{4.12}$$

The local Cartesian basis vectors $\bar{\boldsymbol{e}}_\alpha$ are used in expressing a constitutive relationship for the shell. Because the local basis is orthonormal, we make no distinction between covariant and contravariant quantities, which are expressed with respect to it. With the above definitions,

we calculate the components of the Green-Lagrange strain tensor and its variation in the local coordinate system as

$$\bar{E}_{\alpha\beta} = \bar{\varepsilon}_{\alpha\beta} + \xi_3 \bar{\kappa}_{\alpha\beta} \tag{4.13}$$

$$\delta\bar{E}_{\alpha\beta} = \delta\bar{\varepsilon}_{\alpha\beta} + \xi_3 \delta\bar{\kappa}_{\alpha\beta} \tag{4.14}$$

$$\bar{\varepsilon}_{\alpha\beta} = \varepsilon_{\gamma\delta}(\boldsymbol{G}^{\gamma} \cdot \bar{\boldsymbol{e}}_{\alpha})(\boldsymbol{G}^{\delta} \cdot \bar{\boldsymbol{e}}_{\beta}) \tag{4.15}$$

$$\bar{\kappa}_{\alpha\beta} = \kappa_{\gamma\delta}(\boldsymbol{G}^{\gamma} \cdot \bar{\boldsymbol{e}}_{\alpha})(\boldsymbol{G}^{\delta} \cdot \bar{\boldsymbol{e}}_{\beta}) \tag{4.16}$$

$$\delta\bar{\varepsilon}_{\alpha\beta} = \delta\varepsilon_{\gamma\delta}(\boldsymbol{G}^{\gamma} \cdot \bar{\boldsymbol{e}}_{\alpha})(\boldsymbol{G}^{\delta} \cdot \bar{\boldsymbol{e}}_{\beta}) \tag{4.17}$$

$$\delta\bar{\kappa}_{\alpha\beta} = \delta\kappa_{\gamma\delta}(\boldsymbol{G}^{\gamma} \cdot \bar{\boldsymbol{e}}_{\alpha})(\boldsymbol{G}^{\delta} \cdot \bar{\boldsymbol{e}}_{\beta}) \tag{4.18}$$

The variations of $\delta\bar{\varepsilon}_{\alpha\beta}$ and $\delta\bar{\kappa}_{\alpha\beta}$ may be computed directly by taking the variational derivatives with respect to the displacement vector.

We define the vectors of membrane strain and curvature components in the local coordinate system as

$$\bar{\boldsymbol{\varepsilon}} = \begin{pmatrix} \varepsilon_{11} \\ \varepsilon_{22} \\ \varepsilon_{12} \end{pmatrix} \tag{4.19}$$

and

$$\bar{\boldsymbol{\kappa}} = \begin{pmatrix} \kappa_{11} \\ \kappa_{22} \\ \kappa_{12} \end{pmatrix} \tag{4.20}$$

together with a Green-Lagrange strain vector

$$\bar{\boldsymbol{E}} = \bar{\boldsymbol{\varepsilon}} + \xi_3 \bar{\boldsymbol{\kappa}} \tag{4.21}$$

We assume St. Venant-Kirchhoff materail law and write the following stress-strain relation-

ship in the local coordinate system as

$$\bar{\boldsymbol{S}} = \bar{\boldsymbol{C}}\bar{\boldsymbol{E}} \tag{4.22}$$

where $\bar{\boldsymbol{S}}$ is the vector of components of the second Piola-Kirchhoff stress tensor in the local coordinate system, and $\bar{\boldsymbol{C}}$ is a constitutive material matrix, which is symmetric. Introducing Eq. 4.21 and Eq. 4.22 into the expression of the internal virtual work in Eq. 4.2, we obtain

$$\begin{aligned}
\delta W_{int} &= \int_{\Omega_0^s} \delta\boldsymbol{E} : \boldsymbol{S}\, d\Omega \\
&= \int_{\Omega_0^s} \delta\bar{\boldsymbol{E}} \cdot \bar{\boldsymbol{S}}\, d\Omega \\
&= \int_{\Gamma_0} \left(\int_{h_{th}} \delta\bar{\boldsymbol{E}} \cdot \bar{\boldsymbol{C}}\bar{\boldsymbol{E}} \right) d\Gamma \\
&= \int_{\Gamma_0} \delta\bar{\boldsymbol{\varepsilon}} \left[\left(\int_{h_{th}} \bar{\boldsymbol{C}}\, d\xi_3 \right) \bar{\boldsymbol{\varepsilon}} + \left(\int_{h_{th}} \xi_3 \bar{\boldsymbol{C}}\, d\xi_3 \right) \bar{\boldsymbol{\kappa}} \right] d\Gamma \\
&+ \int_{\Gamma_0} \delta\bar{\boldsymbol{\kappa}} \left[\left(\int_{h_{th}} \xi_3 \bar{\boldsymbol{C}}\, d\xi_3 \right) \bar{\boldsymbol{\varepsilon}} + \left(\int_{h_{th}} \xi_3^2 \bar{\boldsymbol{C}}\, d\xi_3 \right) \bar{\boldsymbol{\kappa}} \right] d\Gamma
\end{aligned} \tag{4.23}$$

For a general orthotropic material,

$$\bar{\boldsymbol{C}}_{ort} = \begin{pmatrix} \frac{E_1}{(1-\nu_{12}\nu_{21})} & \frac{E_1\nu_{21}}{(1-\nu_{12}\nu_{21})} & 0 \\ \frac{E_2\nu_{12}}{(1-\nu_{12}\nu_{21})} & \frac{E_2}{(1-\nu_{12}\nu_{21})} & 0 \\ 0 & 0 & G_{12} \end{pmatrix} \tag{4.24}$$

where E_1 and E_2 are the Young's moduli in the directions defined by the local basis vectors, ν_{12} and ν_{21} are the Poisson's ratios, G_{12} is the shear modulus, and $\nu_{12}E_2 = \nu_{21}E_1$ to ensure the symmetry of the constitutive material matrix $\bar{\boldsymbol{C}}_{ort}$.

In the case of composite materials, we assume that the structure is composed of a set of plies, each modeled as an orthotropic material. We use the classical laminated-plane theory and homogenize the material through-thickness constitutive behavior for a given composite ply layout. Let k denote the k^{th} ply and let n be the total number of plies. We

assume each ply has the same thickness h_{th}/n. Pre-integrating through the shell thickness in Eq. 4.23, the extensional stiffness $\boldsymbol{A}$, coupling stiffness $\boldsymbol{B}$ and bending stiffness $\boldsymbol{D}$ are given by

$$\boldsymbol{A} = \int_{h_{th}} \bar{\boldsymbol{C}}\, d\xi_3 = \frac{h_{th}}{n} \sum_{k=1}^{n} \bar{\boldsymbol{C}}_k \tag{4.25}$$

$$\boldsymbol{B} = \int_{h_{th}} \xi_3 \bar{\boldsymbol{C}}\, d\xi_3 = \frac{h_{th}^2}{n^2} \sum_{k=1}^{n} \bar{\boldsymbol{C}}_k (k - \frac{n}{2} - \frac{1}{2}) \tag{4.26}$$

$$\boldsymbol{D} = \int_{h_{th}} \xi_3^2 \bar{\boldsymbol{C}}\, d\xi_3 = \frac{h_{th}^3}{n^3} \sum_{k=1}^{n} \bar{\boldsymbol{C}}_k \left((k - \frac{n}{2} - \frac{1}{2})^2 + \frac{1}{12} \right) \tag{4.27}$$

where

$$\bar{\boldsymbol{C}}_k = \boldsymbol{T}^T(\theta_k) \bar{\boldsymbol{C}}_{ort} \boldsymbol{T}(\theta_k) \tag{4.28}$$

$\boldsymbol{T}(\theta)$ is given as

$$\boldsymbol{T}(\theta) = \begin{pmatrix} cos^2(\theta) & sin^2(\theta) & sin(\theta)cos(\theta) \\ sin^2(\theta) & cos^2(\theta) & -sin(\theta)cos(\theta) \\ -2sin(\theta)cos(\theta) & 2sin(\theta)cos(\theta) & cos(2\theta) \end{pmatrix} \tag{4.29}$$

In the above equations, θ is the fiber orientation angle in each ply, Eq. 4.28 transforms $\bar{\boldsymbol{C}}_{ort}$ from the principal material coordinate for each ply, $\bar{\boldsymbol{C}}_{ort}$ is constant with each ply.

With the above definitions, the expression for the internal virtual work for a composite shell may be compactly written as

$$\delta W_{int} = \int_{\Gamma_0} \delta\bar{\boldsymbol{\varepsilon}} \cdot (\boldsymbol{A}\bar{\boldsymbol{\varepsilon}} + \boldsymbol{B}\bar{\boldsymbol{\kappa}})\ d\Gamma + \int_{\Gamma_0} \delta\bar{\boldsymbol{\kappa}} \cdot (\boldsymbol{B}\bar{\boldsymbol{\varepsilon}} + \boldsymbol{D}\bar{\boldsymbol{\kappa}})\ d\Gamma \tag{4.30}$$

The complete variational formulation of rotational free isogeometric shell can be stated as:

find the displacement of the shell middle surface $\boldsymbol{d}^h$, such that $\forall \boldsymbol{w}_s^h$,

$$\begin{aligned}
&\int_{\Gamma_t^s} \boldsymbol{w}_s^h \cdot \overline{\rho}_s h_{th} \left(\frac{d^2 \boldsymbol{d}^h}{dt^2} - \boldsymbol{f}_s \right) \mathrm{d}\Gamma \\
&+ \int_{\Gamma_0^s} \delta\, \overline{\boldsymbol{\epsilon}}^h \cdot \left(\boldsymbol{A} \overline{\boldsymbol{\epsilon}}^h + \boldsymbol{B} \overline{\boldsymbol{\kappa}}^h \right) \mathrm{d}\Gamma \\
&+ \int_{\Gamma_0^s} \delta\, \overline{\boldsymbol{\kappa}}^h \cdot \left(\boldsymbol{B} \overline{\boldsymbol{\epsilon}}^h + \boldsymbol{D} \overline{\boldsymbol{\kappa}}^h \right) \mathrm{d}\Gamma \\
&+ \int_{\Gamma_0^s} \delta\, \overline{\boldsymbol{\kappa}}^h \cdot \boldsymbol{D}_b \overline{\boldsymbol{\kappa}}^h \, \mathrm{d}\Gamma \\
&- \int_{(\Gamma_t^s)_h} \boldsymbol{w}_s^h \cdot (\Pi^h \boldsymbol{t}_f^h) \, \mathrm{d}\Gamma = 0
\end{aligned} \tag{4.31}$$

where $(\Gamma_t^s)_h$ is the shell subdomain with a prescribed traction boundary condition, and $\overline{\rho}_s$ is the through-thickness-averaged shell density given by

$$\overline{\rho}_s = \frac{1}{h_{th}} \int_{h_{th}} \rho_2 \, d\xi_3 \tag{4.32}$$

4.3 Isogeometric rotation-free beam/cable formulation

In the case of beams/cables, the 3D continuum description is reduced to that of the shell mid-curves, and the transverse normal stress is neglected. A local curvilinear coordinate system is chosen where ξ_1 is the parametric variable used to define the beam/cable middle curve. The functions $\boldsymbol{X}(\xi_1)$ and $\boldsymbol{x}(\xi_1)$ denote the coordinates of the cable/beam middle curve in the reference and deformed configuration parametrized by ξ_1, respectively. The tangent vector to the middle curve in the current and deformed configuration is given by $\boldsymbol{x}_{,\xi_1}(\xi_1)$ and $\boldsymbol{X}_{,\xi_1}(\xi_1)$ respectively. We make use of the following cable/beam kinematic quantities and

relationships

$$\boldsymbol{b}(\xi_1) = \frac{\boldsymbol{x}_{,\xi_1} \times \boldsymbol{x}_{,\xi_1\xi_1}}{\|\boldsymbol{x}_{,\xi_1} \times \boldsymbol{x}_{,\xi_1\xi_1}\|} \tag{4.33}$$

$$\boldsymbol{n}(\xi_1) = \frac{\boldsymbol{b} \times \boldsymbol{x}_{,\xi_1}}{\|\boldsymbol{b} \times \boldsymbol{x}_{,\xi_1}\|} \tag{4.34}$$

$$\boldsymbol{B}(\xi_1) = \frac{\boldsymbol{X}_{,\xi_1} \times \boldsymbol{X}_{,\xi_1\xi_1}}{\|\boldsymbol{X}_{,\xi_1} \times \boldsymbol{X}_{,\xi_1\xi_1}\|} \tag{4.35}$$

$$\boldsymbol{N}(\xi_1) = \frac{\boldsymbol{B} \times \boldsymbol{X}_{,\xi_1}}{\|\boldsymbol{B} \times \boldsymbol{X}_{,\xi_1}\|} \tag{4.36}$$

$$\boldsymbol{x}^{3D}(\xi_1, \xi_2, \xi_3) = \boldsymbol{x}(\xi_1) + \phi_1(\xi_2, \xi_3)\boldsymbol{b}(\xi_1) + \phi_2(\xi_2, \xi_3)\boldsymbol{n}(\xi_1) \tag{4.37}$$

$$\boldsymbol{X}^{3D}(\xi_1, \xi_2, \xi_3) = \boldsymbol{X}(\xi_1) + \phi_1(\xi_2, \xi_3)\boldsymbol{B}(\xi_1) + \phi_2(\xi_2, \xi_3)\boldsymbol{N}(\xi_1) \tag{4.38}$$

where $\boldsymbol{b}(\xi_1)$ and $\boldsymbol{B}(\xi_1)$ are the bi-normal vector of the middle curve in current and deformed configuration, respectively. $\boldsymbol{n}(\xi_1)$ and $\boldsymbol{N}(\xi_1)$ are the normal vector of the middle curve in current and deformed configuration, respectively. $\boldsymbol{x}^{3D}(\xi_1, \xi_2, \xi_3)$ and $\boldsymbol{X}^{3D}(\xi_1, \xi_2, \xi_3)$ describe the 3D geometry of the cable and beam, parameterized by ξ_1, ξ_2, ξ_3. Here, ξ_2 and ξ_3 are the cable cross-section parametric coordinates, and $\phi_1(\xi_2, \xi_3)$ and $\phi_2(\xi_2, \xi_3)$ are the functions that represent the cross-section parameterization. For a circular cross-section, $\phi_1(\xi_2, \xi_3) = r\xi_2 \cos(\xi_3)$ and $\phi_2(\xi_2, \xi_3) = r\xi_2 \sin(\xi_3)$, where r is the cable cross-section radius, $\xi_2 \in [0, 1]$, and $\xi_3 \in [0, 2\pi]$. With the kinematics given above, the cable cross-sections remain planar and normal to the middle curve in the deformed configuration, the main assumption of the Euler–Bernoulli beam theory.

The Green–Lagrange strain tensor $\boldsymbol{E}$ given by

$$\boldsymbol{E} = E_{\alpha\beta}\boldsymbol{G}^{\alpha} \otimes \boldsymbol{G}^{\beta} \tag{4.39}$$

where $\alpha, \beta = \{1, 2, 3\}$, summation is applied on repeated indices, and $\boldsymbol{G}^{\alpha}$ and $\boldsymbol{g}^{\alpha}$ are the contravariant basis vectors in the reference and current configuration, respectively. The

Green–Lagrange strain tensor components $E_{\alpha\beta}$ in Eq. (4.39) are given by

$$E_{\alpha\beta} = \frac{1}{2}(\boldsymbol{g}_\alpha \cdot \boldsymbol{g}_\beta - \boldsymbol{G}_\alpha \cdot \boldsymbol{G}_\beta) = \frac{1}{2}(\boldsymbol{x}^{3D}_{,\xi_\alpha} \cdot \boldsymbol{x}^{3D}_{,\xi_\beta} - \boldsymbol{X}^{3D}_{,\xi_\alpha} \cdot \boldsymbol{X}^{3D}_{,\xi_\beta}) \tag{4.40}$$

where $\boldsymbol{G}_\alpha$ and $\boldsymbol{g}_\alpha$ are the covariant basis vectors in the reference and current configuration, respectively. At this point we assume the full 3D state of strain, however, as we will see in what follows, only one of the strain components survives in this setting.

To examine the components of the Green–Lagrange strain tensor we explicitly compute the parametric derivatives of the geometrical mapping. For the current configuration we obtain

$$\boldsymbol{x}^{3D}_{,\xi_1}(\xi_1,\xi_2,\xi_3) = \boldsymbol{x}_{,\xi_1}(\xi_1) + \phi_1(\xi_2,\xi_3)\boldsymbol{b}_{,\xi_1}(\xi_1) + \phi_2(\xi_2,\xi_3)\boldsymbol{n}_{,\xi_1}(\xi_1) \tag{4.41}$$

$$\boldsymbol{x}^{3D}_{,\xi_2}(\xi_1,\xi_2,\xi_3) = \phi_{1,\xi_2}(\xi_2,\xi_3)\boldsymbol{b}(\xi_1) + \phi_{2,\xi_2}(\xi_2,\xi_3)\boldsymbol{n}(\xi_1) \tag{4.42}$$

$$\boldsymbol{x}^{3D}_{,\xi_3}(\xi_1,\xi_2,\xi_3) = \phi_{1,\xi_3}(\xi_2,\xi_3)\boldsymbol{b}(\xi_1) + \phi_{2,\xi_3}(\xi_2,\xi_3)\boldsymbol{n}(\xi_1) \tag{4.43}$$

while analogous expressions are obtained for the reference configuration parametric derivatives. Introducing these expressions into Eq. (4.40), we obtain

$$\begin{aligned} E_{11} = \frac{1}{2}\left(\boldsymbol{x}_{,\xi_1} \cdot \boldsymbol{x}_{,\xi_1} - \boldsymbol{X}_{,\xi_1} \cdot \boldsymbol{X}_{,\xi_1}\right) + \phi_1\left(\boldsymbol{x}_{,\xi_1} \cdot \boldsymbol{b}_{,\xi_1} - \boldsymbol{X}_{,\xi_1} \cdot \boldsymbol{B}_{,\xi_1}\right) \\ + \phi_2\left(\boldsymbol{x}_{,\xi_1} \cdot \boldsymbol{n}_{,\xi_1} - \boldsymbol{X}_{,\xi_1} \cdot \boldsymbol{N}_{,\xi_1}\right) + O(h^2) \end{aligned} \tag{4.44}$$

while the remaining components of the strain are either $O(h^2)$ or identically zero, where h denotes the cable cross-section dimension. Since we assume $h << L$, the cable length dimension, and thus neglect the $O(h^2)$ terms, E_{11} is the only nonzero component of the Green–Lagrange strain tensor that remains in the modeling. Furthermore, using the fact that in the current configuration $\boldsymbol{x}_{,\xi_1} \cdot \boldsymbol{b} = 0$ and $\boldsymbol{x}_{,\xi_1} \cdot \boldsymbol{n} = 0$, and taking parametric derivatives of these expressions, gives $-\boldsymbol{x}_{,\xi_1} \cdot \boldsymbol{b}_{,\xi_1} = \boldsymbol{x}_{,\xi_1\xi_1} \cdot \boldsymbol{b}$ and $-\boldsymbol{x}_{,\xi_1} \cdot \boldsymbol{n}_{,\xi_1} = \boldsymbol{x}_{,\xi_1\xi_1} \cdot \boldsymbol{n}$. We also note $\boldsymbol{x}_{,\xi_1\xi_1} \cdot \boldsymbol{b} = 0$, which gives $\boldsymbol{x}_{,\xi_1} \cdot \boldsymbol{b}_{,\xi_1} = 0$. Analogous identities also hold true for the reference

configuration quantities. With these identities, we simplify E_{11} simplifies as

$$E_{11} = \epsilon_b - \phi_2 \kappa_b \tag{4.45}$$

where $\epsilon_b = \frac{1}{2}\left(\boldsymbol{x}_{,\xi_1} \cdot \boldsymbol{x}_{,\xi_1} - \boldsymbol{X}_{,\xi_1} \cdot \boldsymbol{X}_{,\xi_1}\right)$ denote the strain due to membrane action, and κ_b denotes the change in curvature due to bending action, and $\kappa_b = \boldsymbol{x}_{,\xi_1\xi_1} \cdot \boldsymbol{n} - \boldsymbol{X}_{,\xi_1\xi_1} \cdot \boldsymbol{N}$ denotes the curvature change due to bending action

The covariant basis vector in the reference configuration $\boldsymbol{G}_1$ coincides with the tangent vector and is given by

$$\boldsymbol{G}_1 = \boldsymbol{X}_{,\xi_1} \tag{4.46}$$

The contravariant basis vector $\boldsymbol{G}^1$ may expressed as

$$\boldsymbol{G}^1 = \frac{\boldsymbol{G}_1}{\|\boldsymbol{G}_1\|^2} \tag{4.47}$$

(Note that $\|\boldsymbol{G}^1\| = 1/\|\boldsymbol{G}_1\|$.) To write the stress-strain relationship, we first re-express the Green–Lagrange strain as

$$\boldsymbol{E} = E_{11}\boldsymbol{G}^1 \otimes \boldsymbol{G}^1 = \bar{E}_{11}\frac{\boldsymbol{G}^1}{\|\boldsymbol{G}^1\|} \otimes \frac{\boldsymbol{G}^1}{\|\boldsymbol{G}^1\|} \tag{4.48}$$

where $\bar{E}_{11} = E_{11}\|\boldsymbol{G}^1\|^2$ is the dimensionless component of the strain in the basis $\frac{\boldsymbol{G}^1}{\|\boldsymbol{G}^1\|}$. We adopt the St. Venant–Kirchhoff material law and write

$$\bar{S}^{11} = E_c \bar{E}_{11} \tag{4.49}$$

where E_c is the Young's modulus and $\bar{S}^{11}$ is the component of the second Piola–Kirchhoff stress tensor in the basis $\frac{\boldsymbol{G}_1}{\|\boldsymbol{G}_1\|}$. The second Piola–Kirchhoff stress may now be expressed as

$$\boldsymbol{S} = \bar{S}^{11}\frac{\boldsymbol{G}_1}{\|\boldsymbol{G}_1\|} \otimes \frac{\boldsymbol{G}_1}{\|\boldsymbol{G}_1\|} = S^{11}\boldsymbol{G}_1 \otimes \boldsymbol{G}_1 \tag{4.50}$$

where $S^{11} = \bar{S}^{11}/\|\boldsymbol{G}_1\|^2 = \bar{S}^{11}\|\boldsymbol{G}^1\|^2$ is the component of the second Piola–Kirchhoff stress tensor in the covariant basis $\boldsymbol{G}_1$.

Introducing $\bar{E}_{11} = E_{11}\|\boldsymbol{G}^1\|^2$ and Eq. 4.49 into the expression of the internal virtual work in Eq. 4.2, we obtain

$$\begin{aligned}\delta W_{int} &= \int_{\Omega_0^s} \delta\boldsymbol{E} : \boldsymbol{S}\, d\Omega \\ &= \int_{\Omega_0^s} \delta\bar{E}_{11}\bar{S}^{11}\, d\Omega \\ &= \int_{\Omega_0^s} (\delta\epsilon_b - \phi_2\delta\kappa_b)\, E_c\|\boldsymbol{G}^1\|^4\, (\epsilon_b - \phi_2\kappa_b)\; d\Gamma\end{aligned} \tag{4.51}$$

where

$$\delta\epsilon_b = \delta\boldsymbol{x}_{,\xi_1} \cdot \boldsymbol{x}_{,\xi_1} \tag{4.52}$$

and

$$\delta\kappa_b = \delta\boldsymbol{x}_{,\xi_1\xi_1} \cdot \boldsymbol{n} + \boldsymbol{x}_{,\xi_1\xi_1} \cdot \delta\boldsymbol{n} \tag{4.53}$$

are the variations of the membrane strain and curvature, respectively, expressed in terms of the variation of the position vector $\delta\boldsymbol{x}$. Pre-integrating in Eq. (4.51) over A_0, the cable cross-section in the undeformed configuration, we obtain

$$\delta W^{\text{int}} = \int_{L_0} \delta\epsilon_b A_0 E_c\|\boldsymbol{G}^1\|^4\epsilon_b\, dL + \int_{L_0} \delta\kappa_b I_0 E_c\|\boldsymbol{G}^1\|^4\kappa_b\, dL \tag{4.54}$$

where L_0 is the beam/cable middle curve in reference configuration, and $I_0 = \int_{A_0} \phi_2^2\, dA$ is the cable second moment of area, both in the reference configuration.

The complete variational formulation of rotational free beam/cable can be stated as:

find the displacement of the beam/cable middle curve $\boldsymbol{d}^h$, such that $\forall \mathbf{w}_s^h$,

$$\begin{aligned}
&\int_{L_0} \boldsymbol{w}_s^h \cdot \overline{\rho}_s^b A_0 \left(\frac{d^2 \boldsymbol{d}^h}{dt^2} - \mathbf{f}_s \right) \mathrm{d}L \\
&+ \int_{L_0} \delta\, \overline{\boldsymbol{\epsilon}}_b^h \cdot E_c A_0 \left\| \mathbf{G}^1 \right\|^4 \overline{\boldsymbol{\epsilon}}_b^h \, \mathrm{d}L \\
&+ \int_{L_0} \delta\, \overline{\boldsymbol{\kappa}}_b^h \cdot E_c I_0 \left\| \mathbf{G}^1 \right\|^4 \overline{\boldsymbol{\kappa}}_b^h \, \mathrm{d}L = 0
\end{aligned} \tag{4.55}$$

where $\overline{\boldsymbol{\epsilon}}_b^h$ and $\overline{\boldsymbol{\kappa}}_b^h$ are beam/cable membrane strains and curvature changes in Voigt notation written with respect to the local Cartesian basis, and $\delta\overline{\boldsymbol{\epsilon}}_b^h$ and $\delta\overline{\boldsymbol{\kappa}}_b^h$ are the corresponding variations. ρ_s^b is the through-cross-section-averaged shell density given by ρ_s^b

$$\overline{\rho}_s^b = \frac{1}{A_0} \int_{A_0} \rho_2 \, dA \tag{4.56}$$

The formulation of shell and cable/beam are solved in a coupled way by assembling their left hand side matrices and right hand side vectors together. Note that we assume the beams/cables don't feel the loads from the fluid due to small cross section of beams/cables.

4.4 Acknowledgement

This chapter, in part, is a reprint of the materials as they appear in : "Computational free-surface fluid-structure interaction with applications on offshore floating wind turbines" (with A. Korobenko, X. Deng, Y. Bazilevs) *Computers and Fluids*, 2016. The dissertation author is the primary investigator and author of this paper.

Chapter 5

Free-surface FSI formulation

5.1 Augmented Lagrangian approach

To derive the free-surface FSI formulation, the augmented Lagrangian approach is adopted. The augmented Lagrangian function for free-surface fluid-structure interaction problem is defined as

$$\begin{aligned} \boldsymbol{L}(\{\boldsymbol{u}_1, p, \phi\}, \boldsymbol{u}_2, \boldsymbol{\lambda}) &= \boldsymbol{L}_1(\{\boldsymbol{u}_1, p, \phi\}) + \boldsymbol{L}_2(\boldsymbol{u}_2) \\ &+ \int_{(\Gamma_t)_I} \boldsymbol{\lambda} \cdot (\boldsymbol{u}_1 - \boldsymbol{u}_2) \, \mathrm{d}\Gamma \\ &+ \int_{(\Gamma_t)_I} \beta(\boldsymbol{u}_1 - \boldsymbol{u}_2) \cdot (\boldsymbol{u}_1 - \boldsymbol{u}_2) \, \mathrm{d}\Gamma \end{aligned} \tag{5.1}$$

where $\boldsymbol{u}_1, p, \phi$ are the fluid velocity, pressure and level set, respectively, $\boldsymbol{u}_2$ is the structural velocity, $\boldsymbol{L}_1$ and $\boldsymbol{L}_2$ are the Lagrangian functionals whose stationary points generate the variational equations of the free-surface flow (including velocity, pressure and level set) and structural mechanics, $\boldsymbol{\lambda}$ is a Lagrange multiplier for the kinematic interface condition $\boldsymbol{u}_1 = \boldsymbol{u}_2$, and β is a penalty parameter, which we will discuss later. The augmented Lagrangian approach may be interpreted as a combination of the Lagrange multiplier and penalty method. It is a popular approach in optimization, as well as in applications of nonlinear structural mechanics that involve some form of constraints (e.g., contact). Here,

we adopt it as a point of departure for generating a family of FSI formulations.

Taking the variational derivatives of $\boldsymbol{L}$ with respect to the free-surface, structural and Lagrange multiplier unknowns, and setting the result to zero yields the following set of variational equations: find $\{\boldsymbol{u}_1, p_1, \phi\} \in \mathcal{V}_1$, $\boldsymbol{u}_2 \in \mathcal{V}_2$ and the Lagrange multiplier $\boldsymbol{\lambda} \in \mathcal{V}_\lambda$, such that $\forall\{\boldsymbol{w}_1, q, \eta\} \in \mathcal{W}_1$, $\forall \boldsymbol{w}_2 \in \mathcal{W}_2$ and $\forall \delta\boldsymbol{\lambda} \in \mathcal{W}_\lambda$

$$\boldsymbol{B}_1(\{\boldsymbol{w}_1, q, \eta\}, \{\boldsymbol{u}_1, p, \phi\}) - \boldsymbol{F}_1(\boldsymbol{w}_1, q, \eta) + \int_{(\Gamma_t)_I} \boldsymbol{w}_1 \cdot \boldsymbol{\lambda} \, \mathrm{d}\Gamma + \int_{(\Gamma_t)_I} \boldsymbol{w}_1 \cdot \beta(\boldsymbol{u}_1 - \boldsymbol{u}_2) \, \mathrm{d}\Gamma = 0 \tag{5.2}$$

$$\boldsymbol{B}_2(\boldsymbol{w}_2, \boldsymbol{u}_2) - \boldsymbol{F}_2(\boldsymbol{w}_2) - \int_{(\Gamma_t)_I} \boldsymbol{w}_2 \cdot \boldsymbol{\lambda} \, \mathrm{d}\Gamma + \int_{(\Gamma_t)_I} \boldsymbol{w}_2 \cdot \beta(\boldsymbol{u}_1 - \boldsymbol{u}_2) \, \mathrm{d}\Gamma = 0 \tag{5.3}$$

$$\int_{(\Gamma_t)_I} \delta\boldsymbol{\lambda} \cdot (\boldsymbol{u}_1 - \boldsymbol{u}_2) \, \mathrm{d}\Gamma = 0 \tag{5.4}$$

Where $\boldsymbol{B}_1$, $\boldsymbol{B}_2$, $\boldsymbol{F}_1$ and $\boldsymbol{F}_2$ are the semilinear forms and linear functional corresponding to the free-surface and structural mechanics problems, respectively, which are discussed in previous sections. Combined with boundary terms of the variational forms discussed in previous sections, the variational formulations given by Eq. 5.2 and Eq. 5.3 give the following Euler-Lagrange conditions on the fluid-structural interface $(\Gamma_t)_I$

$$\boldsymbol{\lambda} = -\boldsymbol{\sigma}_1 \boldsymbol{n}_1 - \beta(\boldsymbol{u}_1 - \boldsymbol{u}_2) \tag{5.5}$$

$$\boldsymbol{\lambda} = \boldsymbol{\sigma_2} \boldsymbol{n}_2 - \beta(\boldsymbol{u}_1 - \boldsymbol{u}_2) \tag{5.6}$$

where $\boldsymbol{n}_1$ and $\boldsymbol{n}_2$ are the unit outward normal vectors on the fluid and structural domains, respectively. Note that, $\boldsymbol{n}_1 = -\boldsymbol{n}_2$ at the fluid-structure interface. Subtracting Eq. 5.5 from Eq. 5.6 yields

$$\boldsymbol{\sigma}_1 \boldsymbol{n}_1 + \boldsymbol{\sigma}_2 \boldsymbol{n}_2 = \boldsymbol{0} \tag{5.7}$$

which indicates that the fluid and structure traction are in equilibrium at their interface.

The Lagrange multiplier Eq. 5.4 implies the kinematic compatibility condition at the fluid-structure interface, namely

$$\boldsymbol{u}_1 = \boldsymbol{u}_2 \tag{5.8}$$

Remark Note that the traction compatibility condition given by Eq. 5.7 was derived without using the kinematic compatibility condition of Eq. 5.8. This is a consequence of the augmented Lagrangian formulation.

Eq. 5.2, Eq. 5.3 and Eq. 5.9 also imply

$$\boldsymbol{\lambda} = -\boldsymbol{\sigma}_1 \boldsymbol{n}_1 = \boldsymbol{\sigma}_2 \boldsymbol{n}_2 \tag{5.9}$$

which gives an interpretation of the Lagrange multiplier as the interface traction vector that may be computed from the fluid or structural subdomains. As a result, $\boldsymbol{\lambda}$ may be expressed as convex combination of the fluid and structure traction vectors as

$$\boldsymbol{\lambda} = -\alpha \boldsymbol{\sigma}_1 \boldsymbol{n}_1 + (1-\alpha)\boldsymbol{\sigma}_2 \boldsymbol{n}_2 \tag{5.10}$$

where α is a real number between 0 and 1.

We now formally eliminate the Lagrange multiplier from the formulation of the FSI problem. The variation of $\boldsymbol{\lambda}$ with respect to the fluid and structural mechanics unknowns may be computed directly from Eq. 5.10, which gives

$$\delta\boldsymbol{\lambda} = -\alpha\delta(\boldsymbol{\sigma}_1 \boldsymbol{n}_1) + (1-\alpha)\delta(\boldsymbol{\sigma}_2 \boldsymbol{n}_2) \tag{5.11}$$

Introducing Eq. 5.10 and Eq. 5.11 into Eq. 5.2, Eq. 5.2 and Eq. 5.4 and combining them into a single variational form gives: find $\{\boldsymbol{u}_1, p_1, \phi\} \in \mathcal{V}_1$ and $\boldsymbol{u}_2 \in \mathcal{V}_2$, such that $\forall \{\boldsymbol{w}_1, q, \eta\} \in \mathcal{W}_1$

and $\forall \boldsymbol{w}_2 \in \mathcal{W}_2$

$$\begin{aligned}
&\boldsymbol{B}_1(\{\boldsymbol{w}_1, q, \eta\}, \{\boldsymbol{u}_1, p, \phi\}) - \boldsymbol{F}_1(\{\boldsymbol{w}_1, q, \eta\}) + \boldsymbol{B}_2(\boldsymbol{w}_2, \boldsymbol{u}_2) - \boldsymbol{F}_2(\boldsymbol{w}_2) \\
&+ \int_{(\Gamma_t)_I} (\boldsymbol{w}_1 - \boldsymbol{w}_2) \cdot (-\alpha \boldsymbol{\sigma}_1 \boldsymbol{n}_1 + (1-\alpha)\boldsymbol{\sigma}_2 \boldsymbol{n}_2)\, \mathrm{d}\Gamma \\
&+ \int_{(\Gamma_t)_I} (-\alpha \delta(\boldsymbol{\sigma}_1 \boldsymbol{n}_1) + (1-\alpha)\delta(\boldsymbol{\sigma}_2 \boldsymbol{n}_2)) \cdot (\boldsymbol{u}_1 - \boldsymbol{u}_2)\, \mathrm{d}\Gamma \\
&+ \int_{(\Gamma_t)_I} (\boldsymbol{w}_1 - \boldsymbol{w}_2) \cdot \beta(\boldsymbol{u}_1 - \boldsymbol{u}_2)\, \mathrm{d}\Gamma = 0
\end{aligned} \tag{5.12}$$

The variational formulation given by Eq. 5.12 defines a family of FSI formulation parameterized by α and β. However, we note that the different choices of these parameters do not change the underlying FSI problem.

In this work, we choose $\alpha = 1$, which is motivated to avoid taking the variation of the structural stress. The choice β will be defined latter. With this definition of the parameters, we obtain the following coupled formulation: find $\{\boldsymbol{u}_1, p_1, \phi\} \in \mathcal{V}_1$ and $\boldsymbol{u}_2 \in \mathcal{V}_2$, such that $\forall \{\boldsymbol{w}_1, q, \eta\} \in \mathcal{W}_1$ and $\forall \boldsymbol{w}_2 \in \mathcal{W}_2$

$$\begin{aligned}
&\boldsymbol{B}_1(\{\boldsymbol{w}_1, q, \eta\}, \{\boldsymbol{u}_1, p, \phi\}) - \boldsymbol{F}_1(\{\boldsymbol{w}_1, q, \eta\}) + \boldsymbol{B}_2(\boldsymbol{w}_2, \boldsymbol{u}_2) - \boldsymbol{F}_2(\boldsymbol{w}_2) \\
&- \int_{(\Gamma_t)_I} (\boldsymbol{w}_1 - \boldsymbol{w}_2) \cdot \boldsymbol{\sigma}_1 \boldsymbol{n}_1\, \mathrm{d}\Gamma \\
&- \int_{(\Gamma_t)_I} \delta(\boldsymbol{\sigma}_1 \boldsymbol{n}_1) \cdot (\boldsymbol{u}_1 - \boldsymbol{u}_2)\, \mathrm{d}\Gamma \\
&+ \int_{(\Gamma_t)_I} (\boldsymbol{w}_1 - \boldsymbol{w}_2) \cdot \beta(\boldsymbol{u}_1 - \boldsymbol{u}_2)\, \mathrm{d}\Gamma = 0
\end{aligned} \tag{5.13}$$

The coupled formulation given by Eq. 5.13 leads to the following interpretation of the individual fluid and structural subproblems.

The fluid subproblem may be obtained by setting $\boldsymbol{w}_2 = \boldsymbol{0}$ in Eq. 5.13. This yields:

find $\{\boldsymbol{u}_1, p_1, \phi\} \in \mathcal{V}_1$, such that $\forall \{\boldsymbol{w}_1, q, \eta\} \in \mathcal{W}_1$

$$\begin{aligned}
&\boldsymbol{B}_1(\{\boldsymbol{w}_1, q, \eta\}, \{\boldsymbol{u}_1, p, \phi\}) - \boldsymbol{F}_1(\{\boldsymbol{w}_1, q, \eta\}) \\
&- \int_{(\Gamma_t)_I} \boldsymbol{w}_1 \cdot \boldsymbol{\sigma}_1 \boldsymbol{n}_1 \, \mathrm{d}\Gamma \\
&- \int_{(\Gamma_t)_I} \delta(\boldsymbol{\sigma}_1 \boldsymbol{n}_1) \cdot (\boldsymbol{u}_1 - \boldsymbol{u}_2) \, \mathrm{d}\Gamma \\
&+ \int_{(\Gamma_t)_I} \boldsymbol{w}_1 \cdot \beta(\boldsymbol{u}_1 - \boldsymbol{u}_2) \, \mathrm{d}\Gamma = 0
\end{aligned} \tag{5.14}$$

Setting $\{\boldsymbol{u}_1, p_1, \phi\} = \{\boldsymbol{0}, 0, 0\}$ in Eq. 5.13 gives the following structural mechanics subproblem: find $\boldsymbol{u}_2 \in \mathcal{V}_2$, such that $\forall \boldsymbol{w}_2 \in \mathcal{W}_2$

$$\boldsymbol{B}_2(\boldsymbol{w}_2, \boldsymbol{u}_2) - \boldsymbol{F}_2(\boldsymbol{w}_2) + \int_{(\Gamma_t)_I} \boldsymbol{w}_2 \cdot \boldsymbol{\sigma}_1 \boldsymbol{n}_1 \, \mathrm{d} - \int_{(\Gamma_t)_I} \boldsymbol{w}_2 \cdot \beta(\boldsymbol{u}_1 - \boldsymbol{u}_2) \, \mathrm{d}\Gamma = 0 \tag{5.15}$$

which states that at fluid-structure interface structural problem is driven by the fluid traction vector $\boldsymbol{t}_1$ given by

$$\boldsymbol{t}_1 = -\boldsymbol{\sigma}_1 \boldsymbol{n}_1 + \beta(\boldsymbol{u}_1 - \boldsymbol{u}_2) \tag{5.16}$$

The traction vector contains the usual term $-\boldsymbol{\sigma}_1 \boldsymbol{n}_1$, and it is also augmented by the term that is proportional to the difference between the fluid and structural velocities at their interface.

Remark. The coupled formulation given by Eq. 5.1, derived using the augmented Lagrangian approach as a starting point, may also be interpreted as Nitsches method for FSI (see [112, 62]) or as a continuous version of the Discontinuous Galerkin method for FSI applied at the fluid-structure interface.

Remark. The sliding interface formulation of free-surface flows and re-distancing for handling objects in relative motion, can also be inspired from Eq. 5.1 by choosing $\boldsymbol{B}_1$ and $\boldsymbol{F}_1$ to be the bilinear form and linear functional, respectively, corresponding to the fluid mechanics problem on the one subdomain, $\boldsymbol{B}_2$ and $\boldsymbol{F}_2$ to be the bilinear form and linear functional, respectively, corresponding to the fluid mechanics problem on another subdomain, and $\alpha = 1$. Subscripts 1 and 2 denote the quantities pertaining to the fluid

mechanics problem on the the two subdomains, respectively.

Remark. In the above developments we assumed that the trial and test function spaces of the fluid and structural subproblems are independent of each other. This approach provides one with the framework that is capable of handling non-matching fluid and structural interface discretizations. If we explicitly assume that the fluid and structural velocities and the corresponding test functions are continuous at their interface, the FSI formulation given by Eq. 5.17 reduces to: find $\{\boldsymbol{u}_1, p_1, \phi\} \in \mathcal{V}_1$ and $\boldsymbol{u}_2 \in \mathcal{V}_2$, such that $\forall\{\boldsymbol{w}_1, q, \eta\} \in \mathcal{W}_1$ and $\forall \boldsymbol{w}_2 \in \mathcal{W}_2$

$$\boldsymbol{B}_1(\{\boldsymbol{w}_1, q, \eta\}, \{\boldsymbol{u}_1, p, \phi\}) - \boldsymbol{F}_1(\{\boldsymbol{w}_1, q, \eta\}) + \boldsymbol{B}_2(\boldsymbol{w}_2, \boldsymbol{u}_2) - \boldsymbol{F}_2(\boldsymbol{w}_2) = 0 \tag{5.17}$$

This form of the FSI problem is suitable for matching fluid-structure interface meshes. Although somewhat limiting, matching interface discretizations were employed by many researchers [19, 18, 27, 22, 25, 30, 29, 168, 71, 105, 43] to solve several problems of contemporary interest in computational mechanics and engineering.

Remark. The mesh motion problem is governed by the equations of elastostatics with jacobian-based stiffening [152, 157, 78, 150, 153] to preserve the good mesh quality for the entire computation. In the continuum setting, the mesh displacement can be computed from the following variational formulation: find the mesh displacement from its referential configuration, given $\hat{\boldsymbol{y}} \in \mathcal{S}_m$, such that $\forall \boldsymbol{w}_m \in \mathcal{V}_m$:

$$\int_{\hat{\Omega}_t} \boldsymbol{\nabla}^S \boldsymbol{w}_m \cdot \boldsymbol{D}_m \boldsymbol{\nabla}^S \left(\hat{\boldsymbol{y}}(t) - \hat{\boldsymbol{y}}(t^*)\right) = \boldsymbol{0} \tag{5.18}$$

where $\hat{\Omega}_t$ and $\hat{\boldsymbol{y}}(t^*)$ are the fluid domain and its displacement vector, respectively, at time $t^* < t$ and considered known. $\mathcal{S}_m$ and $\mathcal{V}_m$ are the spaces of trial and test functions for the fluid-domain motion. $\boldsymbol{\nabla}^S$ is the symmetric gradient operator evaluated using the spatial coordinate on $\hat{\Omega}_t$, and $\boldsymbol{D}_m$ is the elasticity tensor, defined by two Lamé parameters, which

are given as

$$\mu_m = \frac{E_m}{2(1+\nu_m)} \tag{5.19}$$

$$\lambda_m = \frac{\nu_m E_m}{(1+\nu_m)(1-2\nu_m)} \tag{5.20}$$

where E_m is the mesh Young's modulus, defined as

$$E_m = E^* \left[det\left(\frac{\partial \boldsymbol{x}}{\partial \boldsymbol{\xi}}\right)\right]^{-\Upsilon} \tag{5.21}$$

where E^* and ν_m are the constant, user-prescribed nominal mesh Young's modulus and Poisson's ration. Υ is a real positive number. The mesh Young modulus E_m is scaled with the inverse of the Jacobian determinant of the isoparametric element mapping. The objective is to stiffen the smaller elements, which are typically located close to the fluid-structure interface, than larger elements.

5.2 Time integration of free-surface FSI equations

Let $\boldsymbol{U}, \dot{\boldsymbol{U}}$ and $\boldsymbol{P}$ denote the vectors of nodal degrees-of-freedom of fluid velocity, its time derivative, and pressure, respectively. Let $\boldsymbol{\Phi}$ and $\dot{\boldsymbol{\Phi}}$ denote the vectors of nodal degrees-of-freedom of the level set function and their time derivative. Let $\boldsymbol{D}, \dot{\boldsymbol{D}}$ and $\ddot{\boldsymbol{D}}$ denote the vectors of nodal degrees-of-freedom of structure displacement, velocity and acceleration, respectively. Finally, let $\hat{\boldsymbol{D}}, \dot{\hat{\boldsymbol{D}}}$ and $\ddot{\hat{\boldsymbol{D}}}$ denote the vectors of nodal degrees-of-freedom of mesh displacement, velocity and acceleration, respectively. In conceptual form, full discretization of the free-surface FSI formulation described in the previous section leads to coupled, nonlinear equation systems that need to be solved at every time step, namely: find $\boldsymbol{U}, \dot{\boldsymbol{U}}, \boldsymbol{P}, \boldsymbol{\Phi}, \dot{\boldsymbol{\Phi}}, \boldsymbol{D}, \dot{\boldsymbol{D}}, \ddot{\boldsymbol{D}}, \hat{\boldsymbol{D}}, \dot{\hat{\boldsymbol{D}}}$ and $\ddot{\hat{\boldsymbol{D}}}$, such that

$$\begin{cases} \boldsymbol{N}_{1M}(\boldsymbol{U}, \dot{\boldsymbol{U}}, \boldsymbol{P}, \boldsymbol{\Phi}, \dot{\boldsymbol{\Phi}}, \boldsymbol{D}, \dot{\boldsymbol{D}}, \ddot{\boldsymbol{D}}, \hat{\boldsymbol{D}}, \dot{\hat{\boldsymbol{D}}}, \ddot{\hat{\boldsymbol{D}}}) = \boldsymbol{0} \\ \boldsymbol{N}_{1C}(\boldsymbol{U}, \dot{\boldsymbol{U}}, \boldsymbol{P}, \boldsymbol{\Phi}, \dot{\boldsymbol{\Phi}}, \boldsymbol{D}, \dot{\boldsymbol{D}}, \ddot{\boldsymbol{D}}, \hat{\boldsymbol{D}}, \dot{\hat{\boldsymbol{D}}}, \ddot{\hat{\boldsymbol{D}}}) = \boldsymbol{0} \\ \boldsymbol{N}_{2}(\boldsymbol{U}, \dot{\boldsymbol{U}}, \boldsymbol{P}, \boldsymbol{\Phi}, \dot{\boldsymbol{\Phi}}, \boldsymbol{D}, \dot{\boldsymbol{D}}, \ddot{\boldsymbol{D}}, \hat{\boldsymbol{D}}, \dot{\hat{\boldsymbol{D}}}, \ddot{\hat{\boldsymbol{D}}}) = \boldsymbol{0} \\ \boldsymbol{N}_{3}(\boldsymbol{U}, \dot{\boldsymbol{U}}, \boldsymbol{P}, \boldsymbol{\Phi}, \dot{\boldsymbol{\Phi}}, \boldsymbol{D}, \dot{\boldsymbol{D}}, \ddot{\boldsymbol{D}}, \hat{\boldsymbol{D}}, \dot{\hat{\boldsymbol{D}}}, \ddot{\hat{\boldsymbol{D}}}) = \boldsymbol{0} \\ \boldsymbol{N}_{4}(\boldsymbol{U}, \dot{\boldsymbol{U}}, \boldsymbol{P}, \boldsymbol{\Phi}, \dot{\boldsymbol{\Phi}}, \boldsymbol{D}, \dot{\boldsymbol{D}}, \ddot{\boldsymbol{D}}, \hat{\boldsymbol{D}}, \dot{\hat{\boldsymbol{D}}}, \ddot{\hat{\boldsymbol{D}}}) = \boldsymbol{0} \end{cases} \tag{5.22}$$

where $\boldsymbol{N}_{1M}, \boldsymbol{N}_{1C}, \boldsymbol{N}_2, \boldsymbol{N}_3$ and $\boldsymbol{N}_4$ are the vectors of nodal residuals of fluid momentum, continuity, level set, structure and mesh motion equations.

In the following, we present the time integration algorithm for the above coupled free-surface FSI equations. We make use of the predictor-multicorrector algorithm based on generalized-α method and Newmark scheme. The generalized-α method for time integration was originally proposed for solving structural mechanics equations in [51] and Navier-Stokes equations [77]. It was extended to the FSI equations with single fluid in [18]. The further extension to free-surface FSI equations is presented here. We first define the nodal solutions at the intermediate time level as

$$\dot{\boldsymbol{U}}_{n+\alpha_m} = \dot{\boldsymbol{U}}_n + \alpha_m(\dot{\boldsymbol{U}}_{n+1} - \dot{\boldsymbol{U}}_n) \tag{5.23}$$

$$\boldsymbol{U}_{n+\alpha_f} = \boldsymbol{U}_n + \alpha_f(\boldsymbol{U}_{n+1} - \dot{\boldsymbol{U}}_n) \tag{5.24}$$

$$\dot{\boldsymbol{\Phi}}_{n+\alpha_m} = \dot{\boldsymbol{\Phi}}_n + \alpha_m(\dot{\boldsymbol{\Phi}}_{n+1} - \dot{\boldsymbol{\Phi}}_n) \tag{5.25}$$

$$\boldsymbol{\Phi}_{n+\alpha_f} = \boldsymbol{\Phi}_n + \alpha_f(\boldsymbol{\Phi}_{n+1} - \boldsymbol{\Phi}_n) \tag{5.26}$$

$$\ddot{\boldsymbol{D}}_{n+\alpha_m} = \ddot{\boldsymbol{D}}_n + \alpha_m(\ddot{\boldsymbol{D}}_{n+1} - \ddot{\boldsymbol{D}}_n) \tag{5.27}$$

$$\dot{\boldsymbol{D}}_{n+\alpha_f} = \dot{\boldsymbol{D}}_n + \alpha_f(\dot{\boldsymbol{D}}_{n+1} - \dot{\boldsymbol{D}}_n) \tag{5.28}$$

$$\boldsymbol{D}_{n+\alpha_f} = \boldsymbol{D}_n + \alpha_f(\boldsymbol{D}_{n+1} - \boldsymbol{D}_n) \tag{5.29}$$

$$\ddot{\hat{\boldsymbol{D}}}_{n+\alpha_m} = \ddot{\hat{\boldsymbol{D}}}_n + \alpha_m(\ddot{\hat{\boldsymbol{D}}}_{n+1} - \ddot{\hat{\boldsymbol{D}}}_n) \tag{5.30}$$

$$\dot{\hat{\boldsymbol{D}}}_{n+\alpha_f} = \dot{\hat{\boldsymbol{D}}}_n + \alpha_f(\dot{\hat{\boldsymbol{D}}}_{n+1} - \dot{\hat{\boldsymbol{D}}}_n) \tag{5.31}$$

$$\hat{\boldsymbol{D}}_{n+\alpha_f} = \hat{\boldsymbol{D}}_n + \alpha_f(\hat{\boldsymbol{D}}_{n+1} - \hat{\boldsymbol{D}}_n) \tag{5.32}$$

The fluid momentum, continuity, level set, structure and mesh motion equations are collocated at these intermediate levels:

$$\begin{cases} \boldsymbol{N}_{1M}(\boldsymbol{U}_{n+\alpha_f}, \dot{\boldsymbol{U}}_{n+\alpha_m}, \boldsymbol{P}_{n+1}, \boldsymbol{\Phi}_{n+\alpha_f}, \dot{\boldsymbol{\Phi}}_{n+\alpha_m}, \boldsymbol{D}_{n+\alpha_f}, \dot{\boldsymbol{D}}_{n+\alpha_f}, \ddot{\boldsymbol{D}}_{n+\alpha_m}, \hat{\boldsymbol{D}}_{n+\alpha_f}, \dot{\hat{\boldsymbol{D}}}_{n+\alpha_f}, \ddot{\hat{\boldsymbol{D}}}_{n+\alpha_m}) = \boldsymbol{0} \\ \boldsymbol{N}_{1C}(\boldsymbol{U}_{n+\alpha_f}, \dot{\boldsymbol{U}}_{n+\alpha_m}, \boldsymbol{P}_{n+1}, \boldsymbol{\Phi}_{n+\alpha_f}, \dot{\boldsymbol{\Phi}}_{n+\alpha_m}, \boldsymbol{D}_{n+\alpha_f}, \dot{\boldsymbol{D}}_{n+\alpha_f}, \ddot{\boldsymbol{D}}_{n+\alpha_m}, \hat{\boldsymbol{D}}_{n+\alpha_f}, \dot{\hat{\boldsymbol{D}}}_{n+\alpha_f}, \ddot{\hat{\boldsymbol{D}}}_{n+\alpha_m}) = \boldsymbol{0} \\ \boldsymbol{N}_{2}(\boldsymbol{U}_{n+\alpha_f}, \dot{\boldsymbol{U}}_{n+\alpha_m}, \boldsymbol{P}_{n+1}, \boldsymbol{\Phi}_{n+\alpha_f}, \dot{\boldsymbol{\Phi}}_{n+\alpha_m}, \boldsymbol{D}_{n+\alpha_f}, \dot{\boldsymbol{D}}_{n+\alpha_f}, \ddot{\boldsymbol{D}}_{n+\alpha_m}, \hat{\boldsymbol{D}}_{n+\alpha_f}, \dot{\hat{\boldsymbol{D}}}_{n+\alpha_f}, \ddot{\hat{\boldsymbol{D}}}_{n+\alpha_m}) = \boldsymbol{0} \\ \boldsymbol{N}_{3}(\boldsymbol{U}_{n+\alpha_f}, \dot{\boldsymbol{U}}_{n+\alpha_m}, \boldsymbol{P}_{n+1}, \boldsymbol{\Phi}_{n+\alpha_f}, \dot{\boldsymbol{\Phi}}_{n+\alpha_m}, \boldsymbol{D}_{n+\alpha_f}, \dot{\boldsymbol{D}}_{n+\alpha_f}, \ddot{\boldsymbol{D}}_{n+\alpha_m}, \hat{\boldsymbol{D}}_{n+\alpha_f}, \dot{\hat{\boldsymbol{D}}}_{n+\alpha_f}, \ddot{\hat{\boldsymbol{D}}}_{n+\alpha_m}) = \boldsymbol{0} \\ \boldsymbol{N}_{4}(\boldsymbol{U}_{n+\alpha_f}, \dot{\boldsymbol{U}}_{n+\alpha_m}, \boldsymbol{P}_{n+1}, \boldsymbol{\Phi}_{n+\alpha_f}, \dot{\boldsymbol{\Phi}}_{n+\alpha_m}, \boldsymbol{D}_{n+\alpha_f}, \dot{\boldsymbol{D}}_{n+\alpha_f}, \ddot{\boldsymbol{D}}_{n+\alpha_m}, \hat{\boldsymbol{D}}_{n+\alpha_f}, \dot{\hat{\boldsymbol{D}}}_{n+\alpha_f}, \ddot{\hat{\boldsymbol{D}}}_{n+\alpha_m}) = \boldsymbol{0} \end{cases} \tag{5.33}$$

The above equations are solved for nodal unknowns at t_{n+1}, assuming that the solution at t_n is given. In addition to the above equations, the relationships between the nodal degrees-of-freedom and their time derivatives are given by the discrete Newmark formulas, namely,

$$\boldsymbol{U}_{n+1} = \boldsymbol{U}_n + \Delta t \left((1-\gamma)\dot{\boldsymbol{U}}_n + \gamma \dot{\boldsymbol{U}}_{n+1} \right) \tag{5.34}$$

$$\boldsymbol{\Phi}_{n+1} = \boldsymbol{\Phi}_n + \Delta t \left((1-\gamma)\dot{\boldsymbol{\Phi}}_n + \gamma \dot{\boldsymbol{\Phi}}_{n+1} \right) \tag{5.35}$$

$$\dot{\boldsymbol{D}}_{n+1} = \dot{\boldsymbol{D}}_n + \Delta t \left((1-\gamma)\ddot{\boldsymbol{D}}_n + \gamma \ddot{\boldsymbol{D}}_{n+1} \right) \tag{5.36}$$

$$\boldsymbol{D}_{n+1} = \boldsymbol{D}_n + \Delta t \dot{\boldsymbol{D}}_n + \frac{\Delta t^2}{2} \left((1-2\beta)\ddot{\boldsymbol{D}}_n + 2\beta \ddot{\boldsymbol{D}}_{n+1} \right) \tag{5.37}$$

$$\dot{\hat{\boldsymbol{D}}}_{n+1} = \dot{\hat{\boldsymbol{D}}}_n + \Delta t \left((1-\gamma)\ddot{\hat{\boldsymbol{D}}}_n + \gamma \ddot{\hat{\boldsymbol{D}}}_{n+1} \right) \tag{5.38}$$

$$\hat{\boldsymbol{D}}_{n+1} = \hat{\boldsymbol{D}}_n + \Delta t \dot{\hat{\boldsymbol{D}}}_n + \frac{\Delta t^2}{2} \left((1-2\beta)\ddot{\hat{\boldsymbol{D}}}_n + 2\beta \ddot{\hat{\boldsymbol{D}}}_{n+1} \right) \tag{5.39}$$

To solve the nonlinear system of equations, we employ Newton's method, which results in a two-stage predictor-multicorrector algorithm. Given the nodal solutions of fluid velocity, pressure, level set, structure and mesh solutions at time step t_n, the corresponding quantities at time step t_{n+1} are found by executing the following stages:

Predictor stage. Initialize:

$$
\begin{aligned}
\dot{\boldsymbol{U}}_{n+1}^{0} &= \frac{\gamma-1}{\gamma}\dot{\boldsymbol{U}}_{n} \\
\boldsymbol{U}_{n+1}^{0} &= \boldsymbol{U}_{n} \\
\boldsymbol{P}_{n+1}^{0} &= \boldsymbol{P}_{n} \\
\dot{\boldsymbol{\Phi}}_{n+1}^{0} &= \frac{\gamma-1}{\gamma}\dot{\boldsymbol{\Phi}}_{n} \\
\boldsymbol{\Phi}_{n+1}^{0} &= \boldsymbol{\Phi}_{n} \\
\ddot{\boldsymbol{D}}_{n+1}^{0} &= \frac{\gamma-1}{\gamma}\ddot{\boldsymbol{D}}_{n} \\
\dot{\boldsymbol{D}}_{n+1}^{0} &= \dot{\boldsymbol{D}}_{n} \\
\boldsymbol{D}_{n+1}^{0} &= \boldsymbol{D}_{n} + \Delta t\dot{\boldsymbol{D}}_{n} + \frac{\Delta t^{2}}{2}\left((1-2\beta)\ddot{\boldsymbol{D}}_{n} + \beta\ddot{\boldsymbol{D}}_{n+1}^{0}\right) \\
\ddot{\hat{\boldsymbol{D}}}_{n+1}^{0} &= \frac{\gamma-1}{\gamma}\ddot{\hat{\boldsymbol{D}}}_{n} \\
\dot{\hat{\boldsymbol{D}}}_{n+1}^{0} &= \dot{\hat{\boldsymbol{D}}}_{n} \\
\hat{\boldsymbol{D}}_{n+1}^{0} &= \hat{\boldsymbol{D}}_{n} + \Delta t\dot{\hat{\boldsymbol{D}}}_{n} + \frac{\Delta t^{2}}{2}\left((1-2\beta)\ddot{\hat{\boldsymbol{D}}}_{n} + \beta\ddot{\hat{\boldsymbol{D}}}_{n+1}^{0}\right)
\end{aligned}
\tag{5.40}
$$

where the quantities with subscript n represent the nodal solutions at time level t_n, the quantities with subscript $n+1$ represent the nodal values at time level t_{n+1}, which need to solved by several iterations and the superscript 0 represents the zeroth value of the iteration counter.

Multicorrector stage. We repeat the following 3 steps for $l = 1, ..., l_{max}$, where l is the iteration counter and l_{max} is the maximum number of nonlinear iterations specified for the current time step.

1. Evaluate the iterates at the intermediate time level:

$$
\begin{aligned}
\dot{\boldsymbol{U}}^{l}_{n+\alpha_m} &= \dot{\boldsymbol{U}}_n + \alpha_m(\dot{\boldsymbol{U}}^{l-1}_{n+1} - \dot{\boldsymbol{U}}_n)\\
\boldsymbol{U}^{l}_{n+\alpha_f} &= \boldsymbol{U}_n + \alpha_f(\boldsymbol{U}^{l-1}_{n+1} - \dot{\boldsymbol{U}}_n)\\
\dot{\boldsymbol{\Phi}}^{l}_{n+\alpha_m} &= \dot{\boldsymbol{\Phi}}_n + \alpha_m(\dot{\boldsymbol{\Phi}}^{l-1}_{n+1} - \dot{\boldsymbol{\Phi}}_n)\\
\boldsymbol{\Phi}^{l}_{n+\alpha_f} &= \boldsymbol{\Phi}_n + \alpha_f(\boldsymbol{\Phi}^{l-1}_{n+1} - \boldsymbol{\Phi}_n)\\
\ddot{\boldsymbol{D}}^{l}_{n+\alpha_m} &= \ddot{\boldsymbol{D}}_n + \alpha_m(\ddot{\boldsymbol{D}}^{l-1}_{n+1} - \ddot{\boldsymbol{D}}_n)\\
\dot{\boldsymbol{D}}^{l}_{n+\alpha_f} &= \dot{\boldsymbol{D}}_n + \alpha_f(\dot{\boldsymbol{D}}^{l-1}_{n+1} - \dot{\boldsymbol{D}}_n)\\
\boldsymbol{D}^{l}_{n+\alpha_f} &= \boldsymbol{D}_n + \alpha_f(\boldsymbol{D}^{l-1}_{n+1} - \boldsymbol{D}_n)\\
\ddot{\hat{\boldsymbol{D}}}^{l}_{n+\alpha_m} &= \ddot{\hat{\boldsymbol{D}}}_n + \alpha_m(\ddot{\hat{\boldsymbol{D}}}^{l-1}_{n+1} - \ddot{\hat{\boldsymbol{D}}}_n)\\
\dot{\hat{\boldsymbol{D}}}^{l}_{n+\alpha_f} &= \dot{\hat{\boldsymbol{D}}}_n + \alpha_f(\dot{\hat{\boldsymbol{D}}}^{l-1}_{n+1} - \dot{\hat{\boldsymbol{D}}}_n)\\
\hat{\boldsymbol{D}}^{l}_{n+\alpha_f} &= \hat{\boldsymbol{D}}_n + \alpha_f(\hat{\boldsymbol{D}}^{l-1}_{n+1} - \hat{\boldsymbol{D}}_n)
\end{aligned}
\tag{5.41}
$$

2. Use the intermediate values to assemble $\boldsymbol{N}^l_{1M}, \boldsymbol{N}^l_{1C}, \boldsymbol{N}^l_2, \boldsymbol{N}^l_3$ and $\boldsymbol{N}^l_4$, the discrete residuals of the momentum, continuity, level set, structure and mesh equations and the corresponding matrices of the linear equation system at l th iteration:

$$
\begin{cases}
\frac{\partial \boldsymbol{N}_{1M}}{\partial \dot{\boldsymbol{U}}_{n+1}}\Big|_l \Delta\dot{\boldsymbol{U}}^l_{n+1} + \frac{\partial \boldsymbol{N}_{1M}}{\partial \boldsymbol{P}_{n+1}}\Big|_l \Delta\boldsymbol{P}^l_{n+1} + \frac{\partial \boldsymbol{N}_{1M}}{\partial \dot{\boldsymbol{\Phi}}_{n+1}}\Big|_l \Delta\dot{\boldsymbol{\Phi}}^l_{n+1} + \frac{\partial \boldsymbol{N}_{1M}}{\partial \ddot{\boldsymbol{D}}_{n+1}}\Big|_l \Delta\ddot{\boldsymbol{D}}^l_{n+1} + \frac{\partial \boldsymbol{N}_{1M}}{\partial \ddot{\hat{\boldsymbol{D}}}_{n+1}}\Big|_l \Delta\ddot{\hat{\boldsymbol{D}}}^l_{n+1} = -\boldsymbol{N}^l_{1M}\\
\frac{\partial \boldsymbol{N}_{1C}}{\partial \dot{\boldsymbol{U}}_{n+1}}\Big|_l \Delta\dot{\boldsymbol{U}}^l_{n+1} + \frac{\partial \boldsymbol{N}_{1C}}{\partial \boldsymbol{P}_{n+1}}\Big|_l \Delta\boldsymbol{P}^l_{n+1} + \frac{\partial \boldsymbol{N}_{1C}}{\partial \dot{\boldsymbol{\Phi}}_{n+1}}\Big|_l \Delta\dot{\boldsymbol{\Phi}}^l_{n+1} + \frac{\partial \boldsymbol{N}_{1C}}{\partial \ddot{\boldsymbol{D}}_{n+1}}\Big|_l \Delta\ddot{\boldsymbol{D}}^l_{n+1} + \frac{\partial \boldsymbol{N}_{1C}}{\partial \ddot{\hat{\boldsymbol{D}}}_{n+1}}\Big|_l \Delta\ddot{\hat{\boldsymbol{D}}}^l_{n+1} = -\boldsymbol{N}^l_{1C}\\
\frac{\partial \boldsymbol{N}_{2}}{\partial \dot{\boldsymbol{U}}_{n+1}}\Big|_l \Delta\dot{\boldsymbol{U}}^l_{n+1} + \frac{\partial \boldsymbol{N}_{2}}{\partial \boldsymbol{P}_{n+1}}\Big|_l \Delta\boldsymbol{P}^l_{n+1} + \frac{\partial \boldsymbol{N}_{2}}{\partial \dot{\boldsymbol{\Phi}}_{n+1}}\Big|_l \Delta\dot{\boldsymbol{\Phi}}^l_{n+1} + \frac{\partial \boldsymbol{N}_{2}}{\partial \ddot{\boldsymbol{D}}_{n+1}}\Big|_l \Delta\ddot{\boldsymbol{D}}^l_{n+1} + \frac{\partial \boldsymbol{N}_{2}}{\partial \ddot{\hat{\boldsymbol{D}}}_{n+1}}\Big|_l \Delta\ddot{\hat{\boldsymbol{D}}}^l_{n+1} = -\boldsymbol{N}^l_{2}\\
\frac{\partial \boldsymbol{N}_{3}}{\partial \dot{\boldsymbol{U}}_{n+1}}\Big|_l \Delta\dot{\boldsymbol{U}}^l_{n+1} + \frac{\partial \boldsymbol{N}_{3}}{\partial \boldsymbol{P}_{n+1}}\Big|_l \Delta\boldsymbol{P}^l_{n+1} + \frac{\partial \boldsymbol{N}_{3}}{\partial \dot{\boldsymbol{\Phi}}_{n+1}}\Big|_l \Delta\dot{\boldsymbol{\Phi}}^l_{n+1} + \frac{\partial \boldsymbol{N}_{3}}{\partial \ddot{\boldsymbol{D}}_{n+1}}\Big|_l \Delta\ddot{\boldsymbol{D}}^l_{n+1} + \frac{\partial \boldsymbol{N}_{3}}{\partial \ddot{\hat{\boldsymbol{D}}}_{n+1}}\Big|_l \Delta\ddot{\hat{\boldsymbol{D}}}^l_{n+1} = -\boldsymbol{N}^l_{3}\\
\frac{\partial \boldsymbol{N}_{4}}{\partial \dot{\boldsymbol{U}}_{n+1}}\Big|_l \Delta\dot{\boldsymbol{U}}^l_{n+1} + \frac{\partial \boldsymbol{N}_{4}}{\partial \boldsymbol{P}_{n+1}}\Big|_l \Delta\boldsymbol{P}^l_{n+1} + \frac{\partial \boldsymbol{N}_{4}}{\partial \dot{\boldsymbol{\Phi}}_{n+1}}\Big|_l \Delta\dot{\boldsymbol{\Phi}}^l_{n+1} + \frac{\partial \boldsymbol{N}_{4}}{\partial \ddot{\boldsymbol{D}}_{n+1}}\Big|_l \Delta\ddot{\boldsymbol{D}}^l_{n+1} + \frac{\partial \boldsymbol{N}_{4}}{\partial \ddot{\hat{\boldsymbol{D}}}_{n+1}}\Big|_l \Delta\ddot{\hat{\boldsymbol{D}}}^l_{n+1} = -\boldsymbol{N}^l_{4}
\end{cases}
\tag{5.42}
$$

The above linear system is solved for the increment of the fluid velocity, pressure, level set, structure and mesh motion unknowns. The coupling strategy that is employed in this paper to solve the above linear equation system will be presented in the next section.

3. Based on Newmark time integration schemes, update the solutions as

$$
\begin{aligned}
\dot{\boldsymbol{U}}^{l}_{n+1} &= \dot{\boldsymbol{U}}^{l-1}_{n+1} + \Delta\dot{\boldsymbol{U}}^{l}_{n+1} \\
\boldsymbol{U}^{l}_{n+1} &= \boldsymbol{U}^{l-1}_{n+1} + \gamma\Delta t\Delta\dot{\boldsymbol{U}}^{l}_{n+1} \\
\boldsymbol{P}^{l}_{n+1} &= \boldsymbol{P}^{l-1}_{n+1} + \Delta\boldsymbol{P}^{l}_{n+1} \\
\dot{\boldsymbol{\Phi}}^{l}_{n+1} &= \dot{\boldsymbol{\Phi}}^{l-1}_{n+1} + \Delta\dot{\boldsymbol{\Phi}}^{l}_{n+1} \\
\boldsymbol{\Phi}^{l}_{n+1} &= \boldsymbol{\Phi}^{l-1}_{n+1} + \gamma\Delta t\dot{\boldsymbol{\Phi}}^{l}_{n+1} \\
\ddot{\boldsymbol{D}}^{l}_{n+1} &= \ddot{\boldsymbol{D}}^{l-1}_{n+1} + \Delta\ddot{\boldsymbol{D}}^{l}_{n+1} \\
\dot{\boldsymbol{D}}^{l}_{n+1} &= \dot{\boldsymbol{D}}^{l-1}_{n+1} + \gamma\Delta t\ddot{\boldsymbol{D}}^{l}_{n+1} \\
\boldsymbol{D}^{l}_{n+1} &= \boldsymbol{D}^{l-1}_{n+1} + \beta\Delta t^2\ddot{\boldsymbol{D}}^{l}_{n+1} \\
\ddot{\hat{\boldsymbol{D}}}^{l}_{n+1} &= \ddot{\hat{\boldsymbol{D}}}^{l-1}_{n+1} + \Delta\ddot{\hat{\boldsymbol{D}}}^{l}_{n+1} \\
\dot{\hat{\boldsymbol{D}}}^{l}_{n+1} &= \dot{\hat{\boldsymbol{D}}}^{l-1}_{n+1} + \gamma\Delta t\ddot{\hat{\boldsymbol{D}}}^{l}_{n+1} \\
\hat{\boldsymbol{D}}^{l}_{n+1} &= \hat{\boldsymbol{D}}^{l-1}_{n+1} + \beta\Delta t^2\ddot{\hat{\boldsymbol{D}}}^{l}_{n+1}
\end{aligned}
\tag{5.43}
$$

Level set clean-up stage. Re-distancing of level set function according to Eq. 2.31 and mass balancing according to Eq. 2.38 are performed after the multicorrector stage is finished. This completes the time step t_{n+1}, at which the time step counter is incremented and we go back to the predictor stage of next time step.

Remark. In above equations, $\alpha_m, \alpha_f, \gamma$ and β are the real-valued parameters that define the generalized-α method and Newmark scheme and chosen based on the stability and accuracy criteria. It has been showed in [77] that second-order accuracy in time is achieved provided that

$$\gamma = \frac{1}{2} + \alpha_m + \alpha_f \tag{5.44}$$

$$\beta = \frac{(1 + \alpha_m + \alpha_f)^2}{4} \tag{5.45}$$

while unconditional stability is attained provided that

$$\alpha_m \geq \alpha_f \geq \frac{1}{2} \tag{5.46}$$

5.3 Quasi-direct coupling with matrix-free technique

To solve the coupled equations (Eq. 5.42), we utilize the quasi-direct coupling, in which the physics system including fluid, level set and structure and mesh system are treated as two separate blocks, and the nonlinear iterations are carried out one block at a time. In solving a block of equations for its associated unknowns, we use the most updated values of the other block of unknowns to assemble the left hand matrices and right hand side vector. As a result, in an iteration step taking us from iterative account $l-1$ to l, the following two blocks of equations are solved.

$$\begin{Bmatrix} \frac{\partial \boldsymbol{N}_{1M}}{\partial \dot{\boldsymbol{U}}_{n+1}} & \frac{\partial \boldsymbol{N}_{1M}}{\partial \boldsymbol{P}_{n+1}} & \frac{\partial \boldsymbol{N}_{1M}}{\partial \dot{\boldsymbol{\Phi}}_{n+1}} & \frac{\partial \boldsymbol{N}_{1M}}{\partial \ddot{\boldsymbol{D}}_{n+1}} \\ \frac{\partial \boldsymbol{N}_{1C}}{\partial \dot{\boldsymbol{U}}_{n+1}} & \frac{\partial \boldsymbol{N}_{1C}}{\partial \boldsymbol{P}_{n+1}} & \frac{\partial \boldsymbol{N}_{1C}}{\partial \dot{\boldsymbol{\Phi}}_{n+1}} & \frac{\partial \boldsymbol{N}_{1C}}{\partial \ddot{\boldsymbol{D}}_{n+1}} \\ \frac{\partial \boldsymbol{N}_{2}}{\partial \dot{\boldsymbol{U}}_{n+1}} & \frac{\partial \boldsymbol{N}_{2}}{\partial \boldsymbol{P}_{n+1}} & \frac{\partial \boldsymbol{N}_{2}}{\partial \dot{\boldsymbol{\Phi}}_{n+1}} & \frac{\partial \boldsymbol{N}_{2}}{\partial \ddot{\boldsymbol{D}}_{n+1}} \\ \frac{\partial \boldsymbol{N}_{3}}{\partial \dot{\boldsymbol{U}}_{n+1}} & \frac{\partial \boldsymbol{N}_{3}}{\partial \boldsymbol{P}_{n+1}} & \frac{\partial \boldsymbol{N}_{3}}{\partial \dot{\boldsymbol{\Phi}}_{n+1}} & \frac{\partial \boldsymbol{N}_{3}}{\partial \ddot{\boldsymbol{D}}_{n+1}} \end{Bmatrix}_{(l-1,n+1)} \begin{Bmatrix} \Delta \dot{\boldsymbol{U}}^{l}_{n+1} \\ \Delta \boldsymbol{P}^{l}_{n+1} \\ \Delta \dot{\boldsymbol{\Phi}}^{l}_{n+1} \\ \Delta \ddot{\boldsymbol{D}}^{l}_{n+1} \end{Bmatrix} = \begin{Bmatrix} -\boldsymbol{N}_{1M} \\ -\boldsymbol{N}_{1C} \\ -\boldsymbol{N}_{2} \\ -\boldsymbol{N}_{3} \end{Bmatrix}_{(l-1,n+1)} \tag{5.47}$$

$$\dot{\boldsymbol{U}}^{l}_{n+1} = \dot{\boldsymbol{U}}^{l-1}_{n+1} + \Delta \dot{\boldsymbol{U}}^{l}_{n+1} \tag{5.48}$$

$$\boldsymbol{P}^{l}_{n+1} = \boldsymbol{P}^{l-1}_{n+1} + \Delta \dot{\boldsymbol{\Phi}}^{l}_{n+1} \tag{5.49}$$

$$\dot{\boldsymbol{\Phi}}^{l}_{n+1} = \dot{\boldsymbol{\Phi}}^{l-1}_{n+1} + \Delta \dot{\boldsymbol{\Phi}}^{l}_{n+1} \tag{5.50}$$

$$\ddot{\boldsymbol{D}}^{l}_{n+1} = \ddot{\boldsymbol{D}}^{l-1}_{n+1} + \Delta \ddot{\boldsymbol{D}}^{l}_{n+1} \tag{5.51}$$

$$\left.\frac{\partial \boldsymbol{N}_4}{\partial \ddot{\hat{\boldsymbol{D}}}_{n+1}}\right|_{(\dot{\boldsymbol{U}}^{l}_{n+1},\boldsymbol{P}^{l}_{n+1},\dot{\boldsymbol{\Phi}}^{l}_{n+1},\ddot{\boldsymbol{D}}^{l}_{n+1},\ddot{\hat{\boldsymbol{D}}}^{l-1}_{n+1})} \Delta\ddot{\hat{\boldsymbol{D}}}^{l}_{n+1} = -\boldsymbol{N}_4(\dot{\boldsymbol{U}}^{l}_{n+1}, \boldsymbol{P}^{l}_{n+1}, \dot{\boldsymbol{\Phi}}^{l}_{n+1}, \ddot{\boldsymbol{D}}^{l}_{n+1}, \ddot{\hat{\boldsymbol{D}}}^{l-1}_{n+1}) \tag{5.52}$$

$$\ddot{\hat{\boldsymbol{D}}}^{l}_{n+1} = \ddot{\hat{\boldsymbol{D}}}^{l-1}_{n+1} + \Delta\ddot{\hat{\boldsymbol{D}}}^{l}_{n+1} \tag{5.53}$$

In Eq. 5.47 , the subscript $(l-1, n+1)$ means the left hand matrix and right hand vector of the physics block are evaluated by intermediate solution $(\dot{\boldsymbol{U}}^{l-1}_{n+1}, \boldsymbol{P}^{l-1}_{n+1}, \dot{\boldsymbol{\Phi}}^{l-1}_{n+1}, \ddot{\boldsymbol{D}}^{l-1}_{n+1}, \ddot{\hat{\boldsymbol{D}}}^{l-1}_{n+1})$. In quasi-direct coupling, the off-diagonal derivatives are needed to solve the physics block system given by Eq. 5.47. Since non-matching discretizations are employed between the fluid domain and structure domain, it is tedious to derive the mathematical expressions and construct the corresponding data structure to represent and store these off-diagonal derivatives. In order to avoid assembling these off-diagonal terms, flexible-GMRES (FGMRES) solver with block-preconditioning is adopted. To present the technique in some detail, let $\boldsymbol{J}_{phy}$ denote the left hand side matrix of the physics block given by Eq. 5.47. The basic idea of GMRES solver is that the solution of the linear system is minimized within the Krylov subspace. Considering the fact that the only operation taken on the Jacobian matrix inside the GMRES solver is its production with the vector in the Krylov space, namely $\boldsymbol{J}_{phy}\boldsymbol{e}_{phy}$, where $\boldsymbol{e}_{phy}$ is the vector in Krylov space $\boldsymbol{J}_{phy}$ is acting on, given as

$$\boldsymbol{e}_{phy} = (\boldsymbol{e}_u, \boldsymbol{e}_p, \boldsymbol{e}_\phi, \boldsymbol{e}_s)^T \tag{5.54}$$

where $\boldsymbol{e}_u, \boldsymbol{e}_p, \boldsymbol{e}_\phi, \boldsymbol{e}_s$ are the parts associated with fluid acceleration, pressure, time derivative of level set and structural acceleration. This matrix-vector production $\boldsymbol{J}_p\boldsymbol{e}_p$ inside FGMRES

solver can be approximated by the following finite difference scheme:

$$\boldsymbol{J}_{phy}\boldsymbol{e}_{phy} \approx \begin{Bmatrix} \frac{\boldsymbol{N}_{1M}(\dot{\boldsymbol{U}}_{n+1}^{l-1}+\epsilon_u\boldsymbol{e}_u,\boldsymbol{P}_{n+1}^{l-1}+\epsilon_u\boldsymbol{e}_p,\dot{\boldsymbol{\Phi}}_{n+1}^{l-1}+\epsilon_u\boldsymbol{e}_\phi,\ddot{\boldsymbol{D}}_{n+1}^{l-1}+\epsilon_u\boldsymbol{e}_s)-\boldsymbol{N}_{1M}(\dot{\boldsymbol{U}}_{n+1}^{l-1},\boldsymbol{P}_{n+1}^{l-1},\dot{\boldsymbol{\Phi}}_{n+1}^{l-1},\ddot{\boldsymbol{D}}_{n+1}^{l-1})}{\epsilon_u} \\ \frac{\boldsymbol{N}_{1C}(\dot{\boldsymbol{U}}_{n+1}^{l-1}+\epsilon_p\boldsymbol{e}_u,\boldsymbol{P}_{n+1}^{l-1}+\epsilon_p\boldsymbol{e}_p,\dot{\boldsymbol{\Phi}}_{n+1}^{l-1}+\epsilon_p\boldsymbol{e}_\phi,\ddot{\boldsymbol{D}}_{n+1}^{l-1}+\epsilon_p\boldsymbol{e}_s)-\boldsymbol{N}_{1C}(\dot{\boldsymbol{U}}_{n+1}^{l-1},\boldsymbol{P}_{n+1}^{l-1},\dot{\boldsymbol{\Phi}}_{n+1}^{l-1},\ddot{\boldsymbol{D}}_{n+1}^{l-1})}{\epsilon_p} \\ \frac{\boldsymbol{N}_{2}(\dot{\boldsymbol{U}}_{n+1}^{l-1}+\epsilon_\phi\boldsymbol{e}_u,\boldsymbol{P}_{n+1}^{l-1}+\epsilon_\phi\boldsymbol{e}_p,\dot{\boldsymbol{\Phi}}_{n+1}^{l-1}+\epsilon_\phi\boldsymbol{e}_\phi,\ddot{\boldsymbol{D}}_{n+1}^{l-1}+\epsilon_\phi\boldsymbol{e}_s)-\boldsymbol{N}_{2}(\dot{\boldsymbol{U}}_{n+1}^{l-1},\boldsymbol{P}_{n+1}^{l-1},\dot{\boldsymbol{\Phi}}_{n+1}^{l-1},\ddot{\boldsymbol{D}}_{n+1}^{l-1})}{\epsilon_\phi} \\ \frac{\boldsymbol{N}_{3}(\dot{\boldsymbol{U}}_{n+1}^{l-1}+\epsilon_s\boldsymbol{e}_u,\boldsymbol{P}_{n+1}^{l-1}+\epsilon_s\boldsymbol{e}_p,\dot{\boldsymbol{\Phi}}_{n+1}^{l-1}+\epsilon_s\boldsymbol{e}_\phi,\ddot{\boldsymbol{D}}_{n+1}^{l-1}+\epsilon_s\boldsymbol{e}_s)-\boldsymbol{N}_{3}(\dot{\boldsymbol{U}}_{n+1}^{l-1},\boldsymbol{P}_{n+1}^{l-1},\dot{\boldsymbol{\Phi}}_{n+1}^{l-1},\ddot{\boldsymbol{D}}_{n+1}^{l-1})}{\epsilon_s} \end{Bmatrix} \tag{5.55}$$

where $\epsilon_u, \epsilon_p, \epsilon_\phi, \epsilon_s$ are small perturbation values. Depending on the problems, different appropriate ϵ values may be used for fluid, level set and structure equations. In our computation, we perturb the free-surface flow solutions with the same perturbation value and perturb the structure solution with another bigger value, namely $\epsilon_u = \epsilon_p = \epsilon_\phi < \epsilon_s$.

Given that the evaluation of $\boldsymbol{N}_{1M}, \boldsymbol{N}_{1C}, \boldsymbol{N}_2, \boldsymbol{N}_3$ is relatively expensive, a good preconditioner is justified. As preconditioning for the coupled matrix, we solve the diagonal blocks representing the individual fluid, level set and structure problems. The corresponding preconditioning matrix is given by Eq. 5.56. For preconditioning, the individual fluid and level set subproblems are solved by diagonally preconditioned GMRES solver [118] and the structure subproblem is solved by diagonally preconditioned Conjugate Gradient method [64].

$$\boldsymbol{M}_{pre} = \begin{Bmatrix} \frac{\partial \boldsymbol{N}_{1M}}{\partial \dot{\boldsymbol{U}}_{n+1}} & \frac{\partial \boldsymbol{N}_{1M}}{\partial \boldsymbol{P}_{n+1}} & 0 & 0 \\ \frac{\partial \boldsymbol{N}_{1C}}{\partial \dot{\boldsymbol{U}}_{n+1}} & \frac{\partial \boldsymbol{N}_{1C}}{\partial \boldsymbol{P}_{n+1}} & 0 & 0 \\ 0 & 0 & \frac{\partial \boldsymbol{N}_{2}}{\partial \dot{\boldsymbol{\Phi}}_{n+1}} & 0 \\ 0 & 0 & 0 & \frac{\partial \boldsymbol{N}_{3}}{\partial \ddot{\boldsymbol{D}}_{n+1}} \end{Bmatrix}^{-1} \tag{5.56}$$

Remark. Eq. 5.55 presents a first-order finite-difference approximation of the action of the Jacobian matrix on a vector from a Krylov space. To improve accuracy, higher-oder schemes, like central-difference approximation (Eq. 5.57), may be adopted to compute a matrix-vector product. However, these are also computationally more expensive, a tradeoff

that could be examined for a given application.

$$\boldsymbol{J}_{phy}\boldsymbol{e}_{phy} \approx \left\{ \begin{array}{c} \frac{\boldsymbol{N}_{1M}(\dot{\boldsymbol{U}}^{l-1}_{n+1}+\epsilon_u\boldsymbol{e}_u,\boldsymbol{P}^{l-1}_{n+1}+\epsilon_u\boldsymbol{e}_p,\dot{\boldsymbol{\Phi}}^{l-1}_{n+1}+\epsilon_u\boldsymbol{e}_\phi,\ddot{\boldsymbol{D}}^{l-1}_{n+1}+\epsilon_u\boldsymbol{e}_s)-\boldsymbol{N}_{1M}(\dot{\boldsymbol{U}}^{l-1}_{n+1}-\epsilon_u\boldsymbol{e}_u,\boldsymbol{P}^{l-1}_{n+1}-\epsilon_u\boldsymbol{e}_p,\dot{\boldsymbol{\Phi}}^{l-1}_{n+1}-\epsilon_u\boldsymbol{e}_\phi,\ddot{\boldsymbol{D}}^{l-1}_{n+1}-\epsilon_u\boldsymbol{e}_s)}{2\epsilon_u} \\ \frac{\boldsymbol{N}_{1C}(\dot{\boldsymbol{U}}^{l-1}_{n+1}+\epsilon_p\boldsymbol{e}_u,\boldsymbol{P}^{l-1}_{n+1}+\epsilon_p\boldsymbol{e}_p,\dot{\boldsymbol{\Phi}}^{l-1}_{n+1}+\epsilon_p\boldsymbol{e}_\phi,\ddot{\boldsymbol{D}}^{l-1}_{n+1}+\epsilon_p\boldsymbol{e}_s)-\boldsymbol{N}_{1C}(\dot{\boldsymbol{U}}^{l-1}_{n+1}-\epsilon_p\boldsymbol{e}_u,\boldsymbol{P}^{l-1}_{n+1}-\epsilon_p\boldsymbol{e}_p,\dot{\boldsymbol{\Phi}}^{l-1}_{n+1}-\epsilon_p\boldsymbol{e}_\phi,\ddot{\boldsymbol{D}}^{l-1}_{n+1}-\epsilon_p\boldsymbol{e}_s)}{2\epsilon_p} \\ \frac{\boldsymbol{N}_{2}(\dot{\boldsymbol{U}}^{l-1}_{n+1}+\epsilon_\phi\boldsymbol{e}_u,\boldsymbol{P}^{l-1}_{n+1}+\epsilon_\phi\boldsymbol{e}_p,\dot{\boldsymbol{\Phi}}^{l-1}_{n+1}+\epsilon_\phi\boldsymbol{e}_\phi,\ddot{\boldsymbol{D}}^{l-1}_{n+1}+\epsilon_\phi\boldsymbol{e}_s)-\boldsymbol{N}_{2}(\dot{\boldsymbol{U}}^{l-1}_{n+1}-\epsilon_\phi\boldsymbol{e}_u,\boldsymbol{P}^{l-1}_{n+1}-\epsilon_\phi\boldsymbol{e}_p,\dot{\boldsymbol{\Phi}}^{l-1}_{n+1}-\epsilon_\phi\boldsymbol{e}_\phi,\ddot{\boldsymbol{D}}^{l-1}_{n+1}-\epsilon_\phi\boldsymbol{e}_s)}{2\epsilon_\phi} \\ \frac{\boldsymbol{N}_{3}(\dot{\boldsymbol{U}}^{l-1}_{n+1}+\epsilon_s\boldsymbol{e}_u,\boldsymbol{P}^{l-1}_{n+1}+\epsilon_s\boldsymbol{e}_p,\dot{\boldsymbol{\Phi}}^{l-1}_{n+1}+\epsilon_s\boldsymbol{e}_\phi,\ddot{\boldsymbol{D}}^{l-1}_{n+1}+\epsilon_s\boldsymbol{e}_s)-\boldsymbol{N}_{3}(\dot{\boldsymbol{U}}^{l-1}_{n+1}-\epsilon_s\boldsymbol{e}_u,\boldsymbol{P}^{l-1}_{n+1}-\epsilon_s\boldsymbol{e}_p,\dot{\boldsymbol{\Phi}}^{l-1}_{n+1}-\epsilon_s\boldsymbol{e}_\phi,\ddot{\boldsymbol{D}}^{l-1}_{n+1}-\epsilon_s\boldsymbol{e}_s)}{2\epsilon_s} \end{array} \right\} \tag{5.57}$$

5.4 Acknowledgement

This chapter, in part, is a reprint of the materials as they appear in : "Computational free-surface fluid-structure interaction with applications on offshore floating wind turbines" (with A. Korobenko, X. Deng, Y. Bazilevs) *Computers and Fluids*, 2016. The dissertation author is the primary investigator and author of this paper.

Chapter 6

Applications: Fluid-structure interaction simulations

In this chapter, the proposed free-surface FSI formulation is applied on several real-world engineering problems . In Section 6.1, the fluid-structure interaction framework is applied on Kayak propulsion system using compliant hydrofoils, which is a joint work with Hobbie cat company. The experimental test is also briefly described. In Section 6.2, 3D, dynamic, fully coupled free-surface FSI simulations of OC3-Hywind floating wind turbines are performed under several wave conditions. To solve the problem, all the capabilities of the proposed free-surface FSI framework are enabled. The free-surface FSI simulation with small amplitude Airy wave inflow condition is performed first. To better access the survivability of the floating wind turbines, an auxiliary piston-type numerical wave generator used to generate violent and realistic waves is also introduced, and the FSI simulation of the floating wind turbines subjected to realistic numerical wave is presented.

6.1 Kayak propulsion using compliant hydrofoils

Nowadays, bio-inspired design concepts are widely used in engineering applications, like Micro Aerial Vehicles (MAV), Kayak Propulsion and the placement of Vertical-Axis Wind Turbines (VAWTs) arrays [54, 92, 126, 146, 140]. The idea comes from that the

performance and efficiency of these devices may be improved by mimicking the shape, structure and motion of animals, like birds, insects, or fishes, since these factors are somehow optimized in the long span of these animals' evolution. In order to truly understand the underlying mechanism, in the last several years, there has been a significant increase in the research centered around the aerodynamic, hydrodynamic and structural modeling of bio-inspired devices [56, 101, 111, 120, 122, 126, 146, 129].

In this dissertation, we undertake fluid-structure interaction of a bio-inspired propulsion system utilizing compliant hydrofoils. Although there has been an extensive numerical studies of the hydrofoils [91, 98, 116], the fidelity of the simulations need to be raised. In these simulations, the foils were either considered as a rigid body or the geometry and materials of foils were significantly simplified. Few researchers considered the full-scale hydrofoil FSI simulation, where the structural, geometry, material properties and complex operation motions are all modeled. This paper presents a 3D, time-dependent, full-scale, full coupled FSI studies of both a single compliant foil and two compliant foils in tandem configuration for the first time. In our opinion, the FSI simulation of the hydrofoils is very challenging for the following reasons. The first challenging is the Reynolds number of the flow is very high creating truly unsteady turbulent hydrodynamics even under uniform inflow conditions. High-fidelity modeling of the underlying hydrodynamics requires a numerical formulation that properly accounts for this unsteadiness and is valid for all the operation conditions. The second challenging is to represent how the turbulent flow features generated by the upstream foil (front foil) affect the hydrodynamics and structural behavior of the downstream foil (back foil) for the case of two hydrofoils in tandem configuration. The complexity is further increased because the front foil and back foil are operating in close proximity to one another (the closest clearance is less than 0.026m). The third challenging is the foils are quite flexible and undergo large deformations, which requires an accurate and robust structural mechanics formulation and mesh moving techniques. Further more, the front foil and back foil are moving in opposite direction. More advanced mesh moving techniques is required to handle such relative component motion. The last challenging is the relative mass of the foils is small leading to high added mass in the coupled FSI problem

that, in turn, requires more sophisticated coupling strategy.

The above challengings are addressed in present work. For the hydrodynamics, the ALE-VMS method [76, 146, 43] and weakly enforcement essential boundary conditions [32] are adopted. the acts as a Large Eddy Simulation (LES) turbulence model [16, 41], which may be thought of as an extension of the residual-based variational (RBVMS) formulation [17] to moving domains handled using the ALE technique, while the latter relaxes the boundary layers resolution in large spatial engineering applications without losing solution accuracy.

The structural mechanics of the tandem compliant foils are modeled by combining the displacement-based Kirchhoff-Love shell [89, 88] and beam/cable [115] theory. Both the structural mechanics are discretized by Isogeometric Analysis (IGA) with nonuniform rational B-spline (NURBS) [52, 75] . This approach is more efficient by avoiding the rotational degree of freedom and more accurate due to the higher order and higher continuity NURBS-based shape functions. Non-matching discretization of the fluid-structure interface is employed in the FSI modeling here. L2-projection technique is used to transfer the kinematics and traction information between the non-matching surface meshes (see Ref. [31] for more details about method).

To accommodate the rotating motion of the foils superposed on the global elastic deformation of the foils, and to maintain a moving-mesh discretization with good boundary-layer resolution critical for hydrodynamics accuracy, the mesh motion technique is designed as the following. While at the fluid-structure interface the fluid mechanics mesh follows the foils' motion, the outer boundary of the sub-domain 1 and sub-domain 2 that encloses the front foil and back foils are only allowed to move as a rigid object. The rigid-body motion part is based on the kinematics conditions applied on the leading edge of the foils and is applied directly to the outer boundaries of the two sub-domains . The fluid mechanics mesh motion in the interior of the two sub-domains is governed by the equations of elasto-statics with Jacobian-based stiffening [78, 123, 157, 150, 152, 158] to preserve the hydrodynamic mesh quality.

The generalized-α method [18, 51, 77] is employed to advance to FSI equations in

time. At every time step, full discretization of the FSI formulation leads to three coupled, nonlinear equations, which correspond to the fluid, structure and mesh part of the problem. In the problem, relatively, the structure is light and the fluid is heavy. The added mass effort is very pronounced, thus, the quasi-direct coupling is employed to solve the nonlinear system [158, 154, 155, 159].

This section is arranged as follows. The structural model of the foil including the geometry and materials distributions is presented in 6.1.2. To validate the structure model, a pure structural simulation is performed. The experiment apparatus and field test results conducted by Hobbie Cat company is briefly introduced 6.1.1. The FSI simulation of single foil configuration is presented in 6.1.3. Then the FSI of two foils in a tandem configuration is performed in 6.1.4

6.1.1 Experimental apparatus

In this section we describe the inner workings of the propulsion system analyzed, which is the Mirage Drive designed and built by Hobie Cat Co. We then provide some details on the measurement system devised to study hydrodynamic loading on the foils and their twisting deformation. The dynamic loading measurements obtained are presented next, and, using this data, propulsive efficiency of the Mirage Drive as a function of travel speed and stroke frequency is assessed.

Mirage Drive propulsion system

The Mirage Drive is a human-powered propulsion system that transforms pedaling motion of a driver into transverse sweeping motion of two underwater foils in tandem configuration (see Figure 6.1 for a depiction of the Mirage Drive propulsion system). The propulsion system is typically installed on surface vessels used for recreational water-sports activities, such as kayaking. The system is installed by inserting it through the boat hull such that the foils protrude beneath the hull, and the pedals are accessible to the driver atop the boat (see Figure 6.2). The foils are placed in a tandem configuration and can sweep through a maximum angle of 196°.

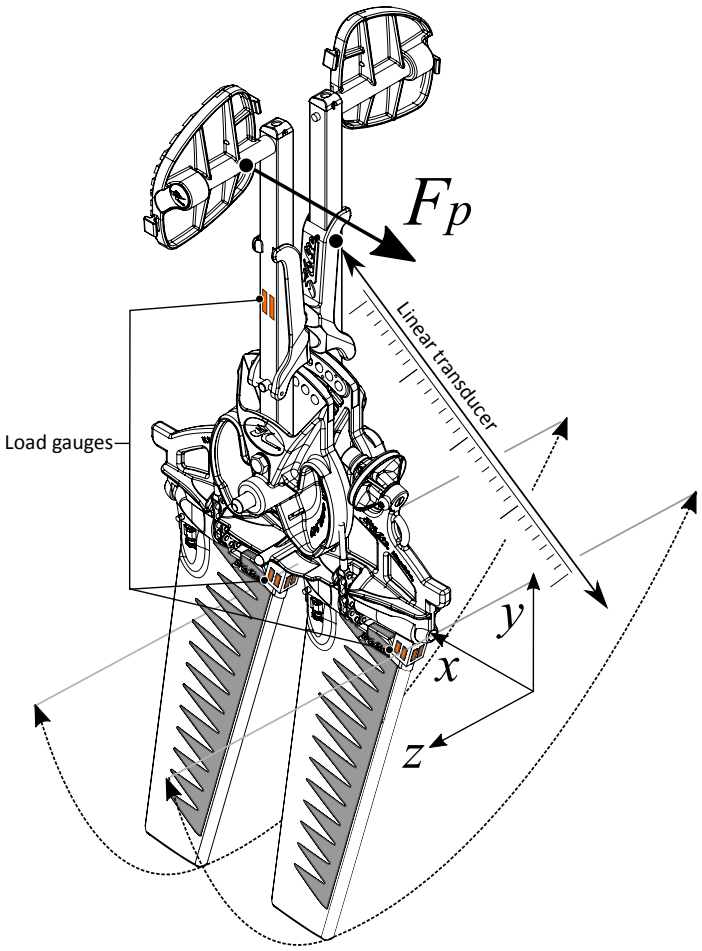

Figure 6.1: Design

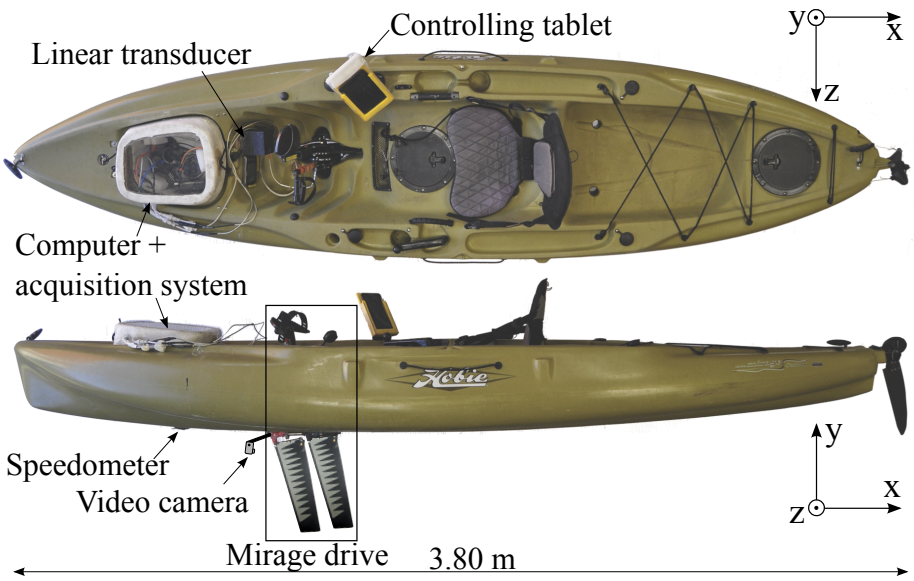

Figure 6.2: Instrumented kayak equipped with the Mirage Drive

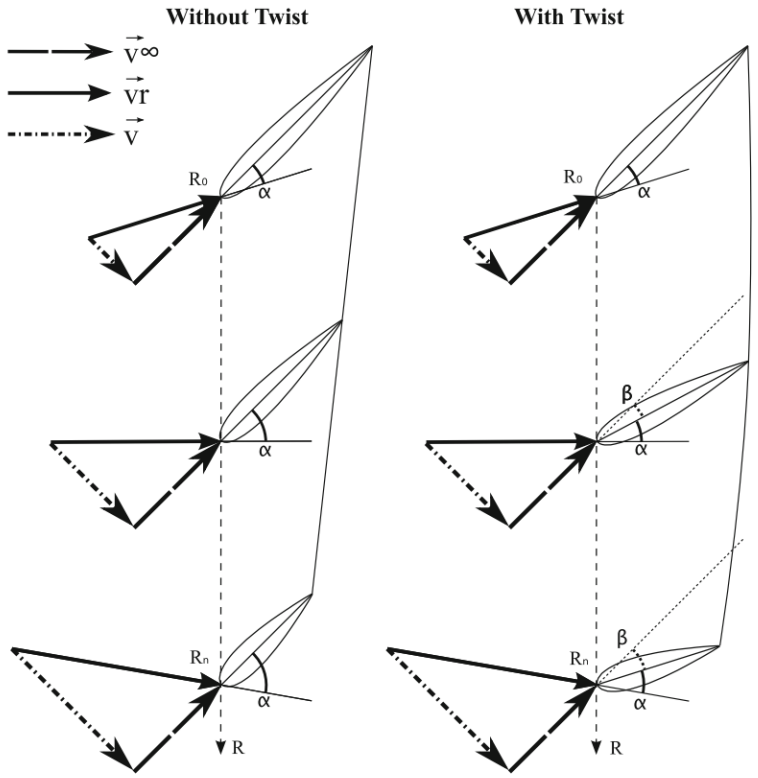

Figure 6.3: Illustration of the apparent flow angle α and twist angle β. In the absence of twisting $\beta = 0$

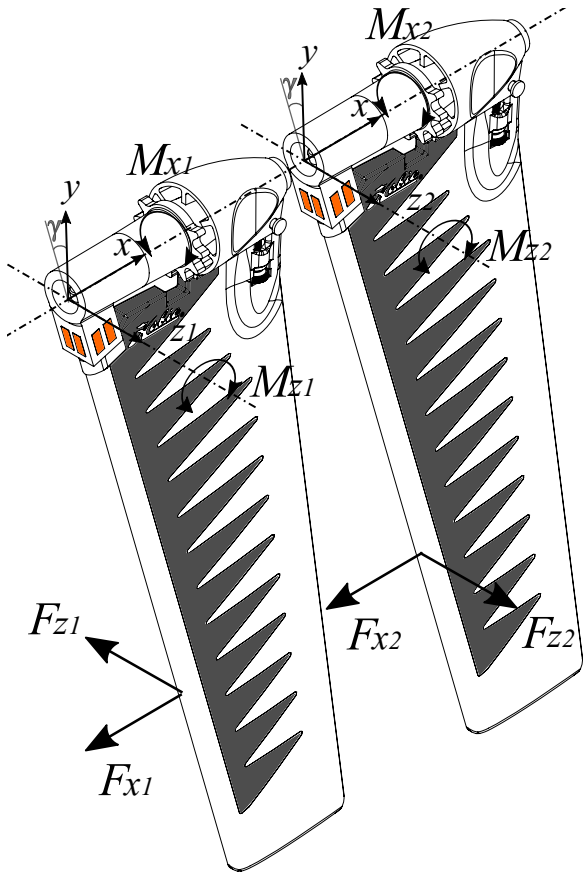

Figure 6.4: Positioning of the gauges and coordinate system employed for the two foils in tandem configuration

As the driver pedals, the foils move under water. The periodic motion of each foil is dominated by rigid-body rotation induced by that of the main steel shaft (or mast) located at the foils leading edge. The rigid body rotation takes place along the axis aligned with the direction of travel of the vessel. The compliant nature of the foils also results in significant twisting and somewhat less pronounced bending motion of the foils axial cross-sections. It is precisely this additional elastic deformation of the foils that generates the necessary thrust force that propels the vessel forward. The foil motion and its compliant nature bring about space- and time-dependent variation of the apparent flow angle α and twist angle β (see Fig. 6.3) for an illustration). In the absence of twisting (i.e., $\beta = 0$) no thrust can be generated, while very large values of β may lead to excessive drag. As a result, it is desirable to design the foil geometry and materials (i.e., stiffness) such that, when the foil is loaded with hydrodynamic forces, the fraction of the pedaling effort that goes into the resulting thrust force is maximized. However, even before such optimization studies are performed, it is important to devise an experimental apparatus, coupled to an advanced FSI model of the propulsion system to understand its behavior in typical operating conditions.

Measurement system

Full-scale measurements are performed on a Outback kayak (see Figure 6.2) also built by the Hobie Cat Co. The Outback is a 3.80 m, 40 kg fully rigged kayak made of rotomolded Polyethylene with the Mirage Drive propulsion system installed. The kayak and propulsion system are equipped with dedicated instrumentation, and the following measurements are performed:

a) Moments on both foils in the x- and z-direction created by the hydrodynamic forces, denoted by M_x and M_z, respectively, are measured using two 120 ohm gauges (HBM LY11-3/120) mounted in a Wheastone bridge configuration. The mast insert is replaced by a stainless steel square bar. The gauges are placed on the square bar, and the bar is welded on the shaft, drilled, and threaded to screw in the mast. We refer to this setup as the hydrodynamic balance. Figure 6.4 illustrates the position of the gauges on each face of the square bar, as well as the coordinate frames used in the study. We assume that the

y- and z-axes rotate with the mast, and the x-axis is coincident with the kayak direction of travel (see Figure 6.2). Note that M_z is generated by the thrust force, while M_x arises due to the lateral forces acting on the foil. As a result, a good foil design may be characterized as having a larger M_z-to-M_x ratio. Also note that different masts can be attached to the stainless steel bar, which facilitates testing many different designs using the same hydrodynamic balance system.

b) The bracket of the left pedal is instrumented in order to measure the time-dependent force applied by the driver, illustrated Figure 6.4. The load sensors are connected to a dedicated gauge analog amplifier and conditioner Expresso from HBM. The position of the pedal is measured by a linear transducer (Figure 6.4) attached from the inside of the cockpit to the right bracket. The linear transducer is linked to a Dataq 430 AD converter.

c) The kayak speed is measured by a trough-the-hull speedometer installed on the kayak. The speed signal is recorded via a dedicated NMEA frame converter. Kayak speed is also recorded using a separate GPS device.

d) A video camera is installed under the hull of the boat in order to capture the motion of the forward foil. A GoPro Hero3 camera and its supporting bar are attached to the base of the mast of the forward foil. The camera follows the motion of the mast by rotating with it. Stripes are superposed on the foil snapshots at 30, 60, 80, and 100 % of the span. Their intersection with the leading and trailing edge are marked by lines. Along the stripes, the foil is equipped with so-called telltales located at 15 and 85 % of the chord. This setup allows us to accurately measure the time-dependent twist angle at the locations along the mast where the stripes are placed. Due to the relatively short focal length of the camera there is some distortion that is present in the image making direct post processing of the twist angle inaccurate. This inaccuracy is overcome with a simple calibration procedure using snapshots of the foil twisted by a prescribed set of angles at each axial cross-section. With this calibration procedure in place, we are able to measure twist angle with 1° precision.

The different instruments employed in the measurements are connected to a inboard PC. Synchronization of the heterogeneous data is done in postprocessing. The load sensors are calibrated to a precision error of $< 1\%$. Because the tests are done in seawater, appropriate

measures are taken to protect the sensors from water damage.

Dynamic load measurements: single foil configuration

The experimental tests presented in this section are done using a set of constant kayak speeds denoted by v_∞. The driver adapts a stroke frequency (or cadence) and the pedal load for different targeted kayak speeds. The following cases are tested corresponding to different cruising conditions:

v_∞ = 1.44 m/s: Low-speed cruising

v_∞ = 1.75 m/s: Medium-speed cruising,

v_∞ = 2.11 m/s: High-speed cruising,

v_∞ = 2.52 m/s: Competitive racing

The driver keeps a steady speed for 60 s while the measurement data is recorded. Fig. 6.5 shows the time history of the applied force perpendicular to the pedal axis at different kayak speeds. Angular position of the pedal is periodic in time and may be closely approximated by a sine function, the fact which we employ in the computation presented later in the paper. Time history of the pedal force exhibits a steep ramp-up followed by a smoother decay. Note that the driver always applies a positive force on the pedal (i.e., the force vector does not change direction). Fig. 6.6 shows the time series of the moments M_x and M_z acting on the foil at different kayak speeds. Some asymmetry is observed between the positive and negative peaks of M_x for the low-speed cruising case, which is consistent with the driver reporting some difficulties in maintaining this low constant kayak speed. The asymmetry in M_x disappears at higher cruising speeds, which were simpler to maintain in the tests performed. The peaks of M_x and M_z are coincident, meaning the trust force is maximum when the foil side load is maximum, both corresponding to the configuration where the foil is orthogonal to the water surface.

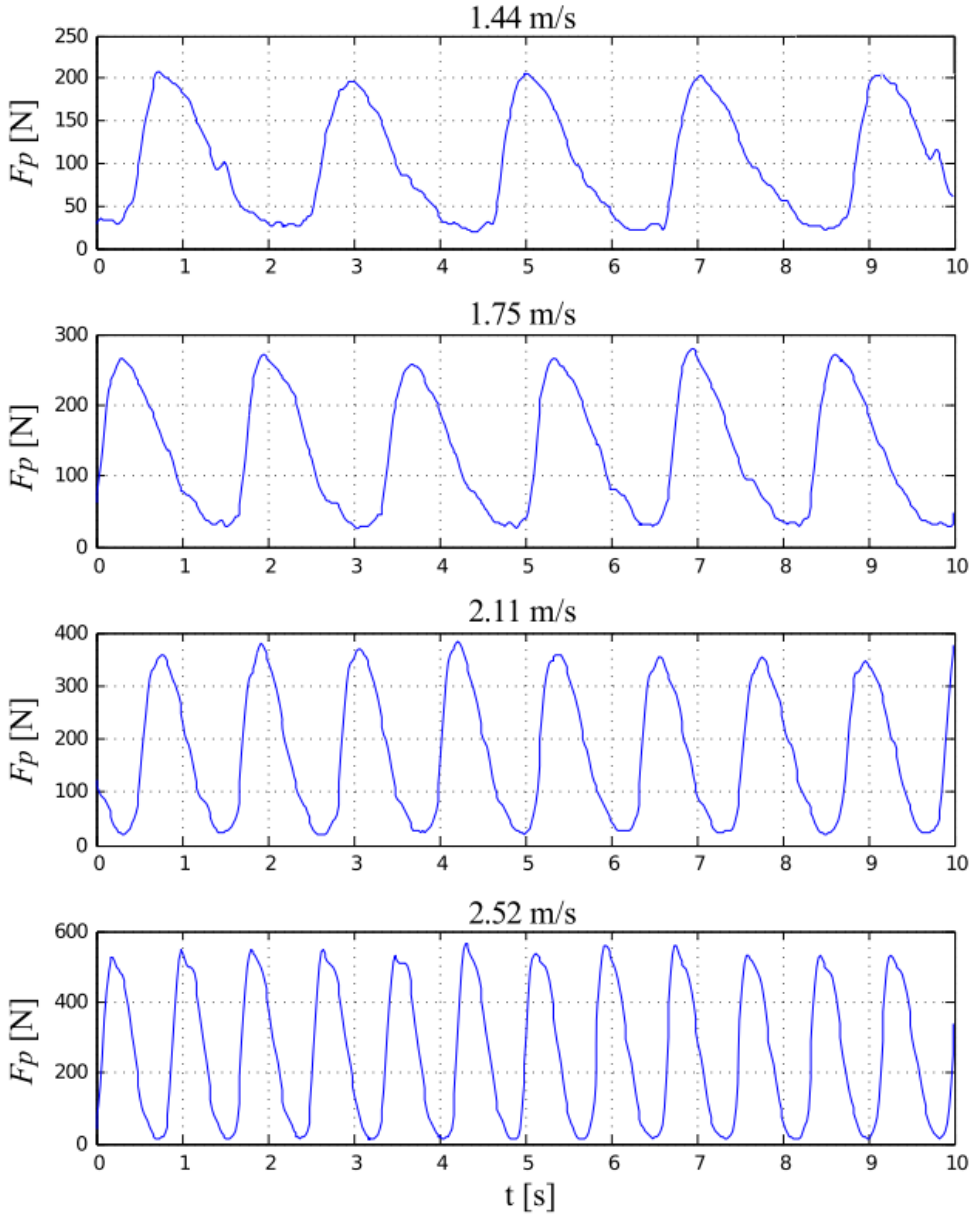

Figure 6.5: Times series of the applied pedal force for different kayak speeds

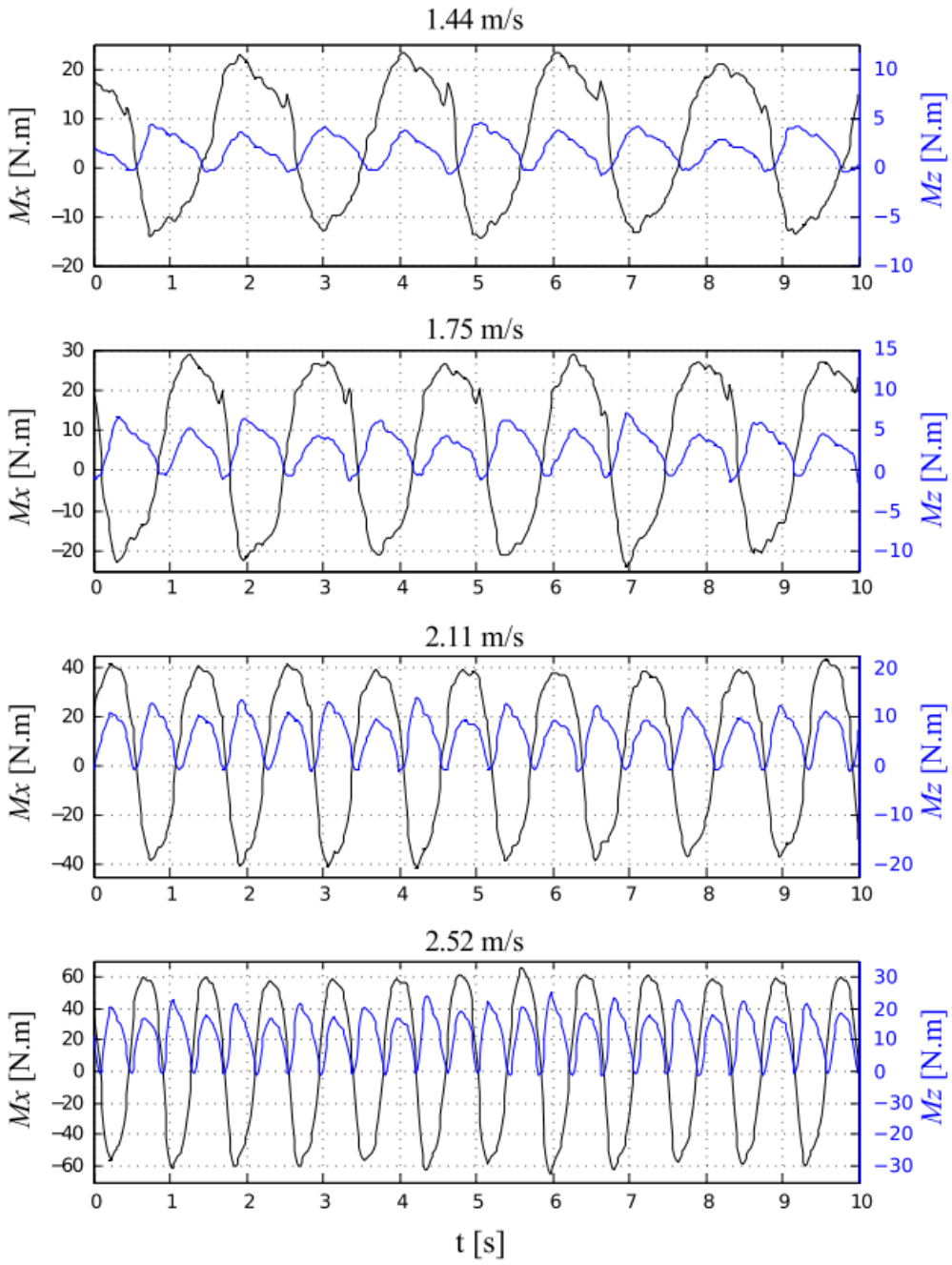

Figure 6.6: Times series of M_x and M_z for different kayak speed

Efficiency of the propulsion system

We define the propulsion system efficiency η_e as the ratio

$$\eta_e = \frac{\overline{P}_{out}}{2\overline{P}_{in}} \tag{6.1}$$

where $\overline{P}_{out}$ and $\overline{P}_{int}$ are the average power out and in, respectively. Here $\overline{P}_{out}$ is defined as power required to overcome the boat drag, which is

$$\overline{P}_{out} = v_\infty \overline{F}_d \tag{6.2}$$

where $\overline{F}_d$ is the average boat drag force. The average power $\overline{P}_{in}$ is defined as that exerted by the driver pushing on the pedal, and may be expressed as

$$\overline{P}_{in} = \frac{1}{T}\int_T F_p l\dot{\theta} dT \tag{6.3}$$

where F_p is the time history of the pedal force shown in Fig.6.5, l is the moment arm (distance from the load sensor to the pedal axis), and $\dot{\theta}$ is the time-dependent angular velocity of the pedal. The factor two in the denominator Eq. 6.1 is due to the fact that there are two pedals.

Table 6.1: Stroke requency f, efficiency η_e, andM_z/M_x, the ratio of the maximum moment corresponding to the propulsive force to that corresponding to the foil side force not contributing to thrust

$v_\infty(m/s)$	1.44	1.75	2.11	2.52
f (Hz)	0.5165	0.6240	0.7498	0.8547
η_e	0.290	0.381	0.458	0.592
M_z/M_x	0.188	0.231	0.335	0.374

Table 6.1 summarizes the boat speed, stroke frequency, and efficiency for the four boat speeds considered. Efficiency η_e is also plotted as a function of boat speed and stroke frequency in Fig. 6.7. The measurement data suggest that the efficiency is nearly a linear function of the boat speed and stroke frequency in the range of boat speeds and stroke

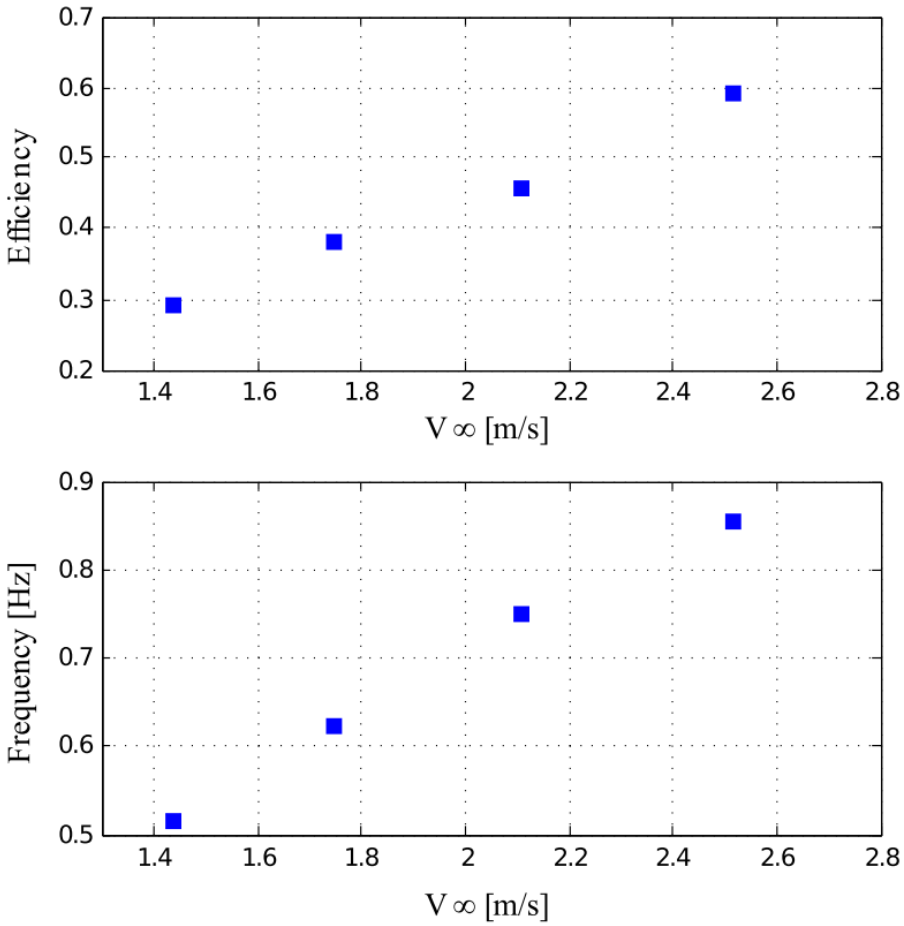

Figure 6.7: Efficiency of the propulsion system as a function of boat speed and stroke frequency. Efficiency is nearly a linear function of the boat speed and stroke frequency within the range of parameters considered

frequencies considered. This linear increase in efficiency with boat speed (and stroke frequency) is likely an intrinsic property of foil-based propulsion systems. Table 6.1 also provides the ratio M_z/M_x, which is the ratio of the maximum moment corresponding to the propulsive force to that corresponding to the foil side force not contributing to thrust. The ratio grows as a function of speed suggesting larger and larger fraction of the total effort goes into propelling the kayak forward as the boat speed is increased. The propulsion system efficiency may be further increased by improving foil geometry and material composition. As a result, besides accurate experimental measurements, it is desirable to develop advanced FSI modeling and simulation methods for such propulsion systems, which is the focus of the following section.

6.1.2 Foil geometry and materials

Figure 6.8 shows the geometry and dimensions of the foil used in Mirage Drive propulsion system. The structure has a symmetric hydrofoil shape. Nearly 10,000 quadratic NURBS elements are employed in the model. The bending strip technique [88] is employed to deal with the multiple-patch discretization. The model is comprised of two material zones, referred to as Black and Grey material, as shown on Figure 6.8. Each zone is made of an isotropic St. Venant-Kirchhoff material with properties summarized in Table 6.2. The zigzag pattern of the material is designed such that the foil has the desired flexibility and stiffness. The chord-wise bending stiffness distribution on the foil surface is presented in Figure 6.8, where the zigzag pattern is clearly visible.

Table 6.2: Material properties

Material	Black	Grey
Young's Modulus(MPa)	27.58	12.24
Poisson's Ratio	0.47	0.47
Density (kg/m^3)	1200	1200

To validate the structural model (i.e., to ensure that the geometry and material distribution are correctly assigned) we perform the sag test of the foil. The setup is presented in Fig. 6.9. The foil is clamped in close proximity of the root, and subjected to gravitational

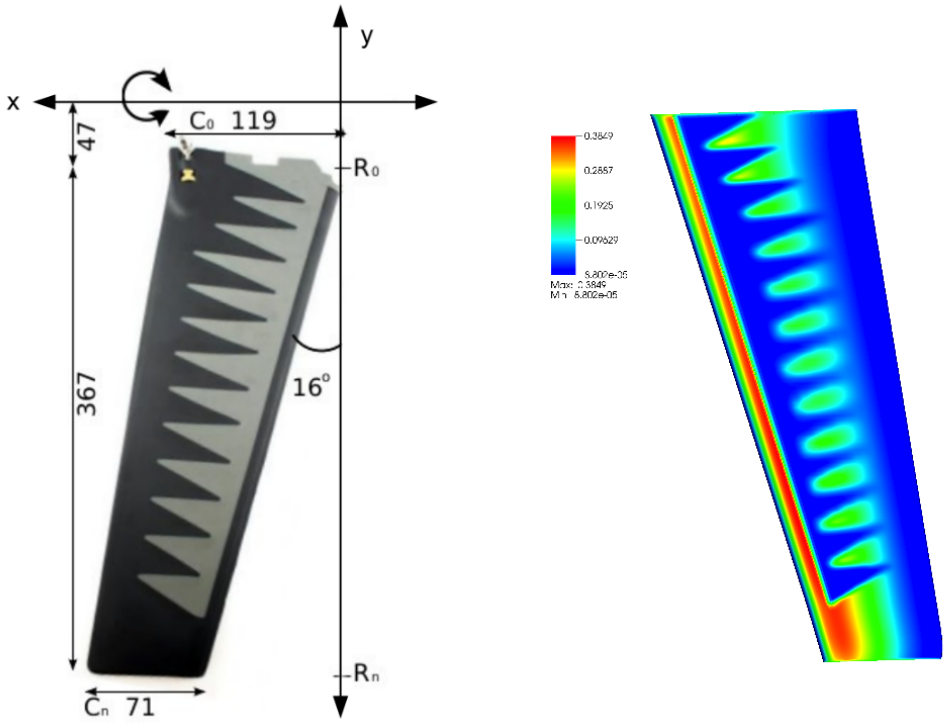

Figure 6.8: (left) Geometry and dimension of the foil (in mm). (b) Blending stiffness distribution in chord wise-direction

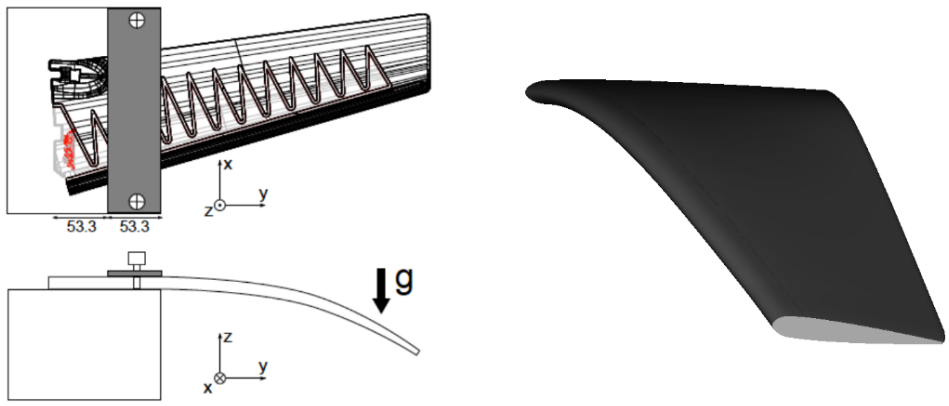

Figure 6.9: (left) Sag test setup. (right) Deformed shape

force due to its weight. For the purposes of the test, the main shaft is removed from the structure. The test results are summarized in Table 6.3. The maximum deflection, twist angle at the tip, and total mass of the foil are compared to the test data and show good

Table 6.3: Comparison of computational values with experiment

	Computation	Experiment
Mass(kg)	0.258	0.26
Max Deflection (mm)	90.2	87.6
Twist Angle (deg)	11	12

agreement. The deformed shape of the foil under gravity is shown in Fig. 6.9, where the tip deflection and twist are clearly visible.

6.1.3 FSI simulation: Single oscillating foil

The FSI simulation of a single oscillating foil is presented in this section. The FSI simulation of two-foil in tandem configuration using the sliding-interface formulation [33, 70, 73] will be presented in next section.

Problem setup

The problem domain is as follows. The outer cylindrical fluid mechanics domain has the radius of 0.96 m and length of 2 m. The foil is placed inside the cylindrical domain as shown in Fig. 6.10. A uniform inflow velocity of 2.11 m/s corresponding to the high-speed cruising case is set on the inlet plane. On the cylinder lateral surface zero streamwise traction is applied, while the remaining velocity components are set to zero. Finally, at the outflow, zero traction (or do nothing) boundary conditions are set.

The fluid mechanics domain uses linear elements, and has triangular prisms in the foil boundary layer and tetrahedra elsewhere in the domain. The boundary-layer mesh is constructed using ten layers of elements, with the size of the first element in the wall-normal direction of 0.0002 m and a growth ratio of 1.2. An inner refinement box is built around the foil in order to better capture the turbulent wake. The statistics of the fluid mechanics

Table 6.4: Mesh sizes (in m) employed in the fluid mechanics domain

Foil	Boundary layer	Inner Box	Outer Cylinder
0.003	0.0002	0.015	0.1

,

Table 6.5: Number of nodes and elements of fluid mechanics mesh

Num. of nodes	Num. of elements
485317	2275660

mesh are summarized in Table 6.4 and Table 6.5. Here,"Surface" gives the element in-plane dimension on the foil surface, "Layer" gives the size of the first boundary-layer element in the direction normal to the foil surface, "Inner" gives the mesh size on the surfaces of the inner box used for mesh refinement near the foil, and "Outer" gives the mesh size on the outer cylindrical boundary. A slice of the fluid mechanics mesh and triangular-prism discretization of the foil boundary layer are shown in Fig. 6.10.

To drive the foil, the following time-dependent kinematic boundary conditions are applied to the leading-edge control points of the foil NURBS mesh:

$$\theta(t) = \frac{A\pi}{2} sin\left(\frac{2\pi t}{T}\right) \tag{6.4}$$

$$\boldsymbol{y}(t) = (\boldsymbol{R}(\theta) - \boldsymbol{I})(\boldsymbol{X} - \boldsymbol{X}_0) \tag{6.5}$$

where $\boldsymbol{R}(\theta)$ is the rotation matrix, $\boldsymbol{X}$ denotes the position of the foil leading-edge control points, and $\boldsymbol{X}_0$ is the center of rotation. In Eq. 6.4, $\frac{A\pi}{2}$ and T give the maximum rotation angle and period of the oscillation (inverse of the stroke frequency), respectively. In the simulation, we set $A = 1.092$ and $T = 1.154s$, which are consistent with the high-speed cruising setup. Application of the rigid-body motion models the effect of the steel shaft driving the foil at the leading edge. The top corner of the trailing edge is attached to the rotation axis using a single NURBS cable element (see Fig 6.11). This models the actual connection between the trailing edge and rotation axis, intentionally designed to allow the foil to develop higher twisting angles. The cable is slightly loosened to allow mild trailing-edge-top-corner displacement, which, in turn, leads to higher overall foil twist.

The fluid mesh on the foil leading edge and the outer cylinder boundary follows the rigid-body motion given by Eq. 6.4 and Eq. 6.5. The fluid mesh on the remainder of foil surface follows the motion of the elastic foil structure. Elsewhere in the domain the mesh

displacement is governed by the equations of elastostatics with Jacobian-based stiffening. The computation is carried out in a parallel computing environment. The mesh is partitioned into subdomains using METIS [84, 85], and each subdomain is assigned to a compute core. The parallel implementation of the methodology may be found in [67]. The time step, Δt, is set to 1.0×10^4 s.

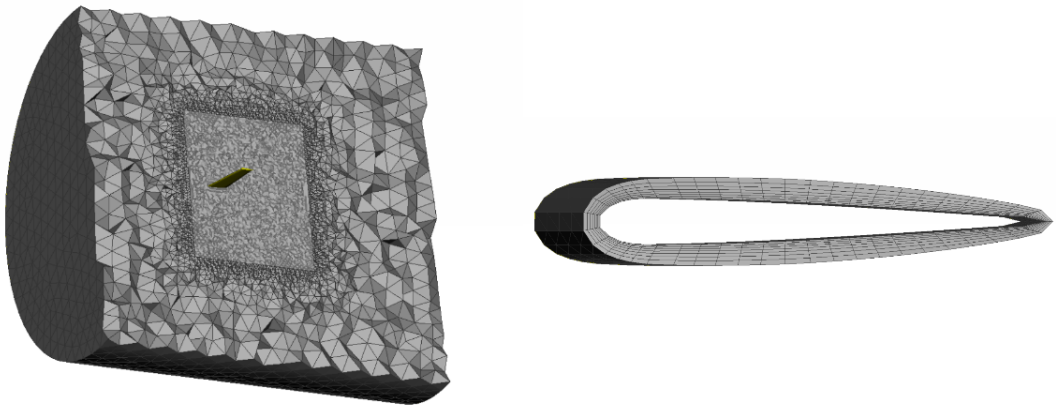

Figure 6.10: (left) Slice of the fluid mechanics mesh showing the outer cylinder, inner box, and foil surface. (right) Triangular-prism discretization of the foil boundary layer

FSI simulation results and discussions

Table 6.6: Comparison of drag and twist angle between the experimental measurements and FSI computation

	Computation	Experiment
Drag(N)	25.53	25.66
Max. Angle(Sec.1)(°)	23.30	22.00
Max. Angle(Sec.2)(°)	29.93	29.00
Max. Angle(Sec.3)(°)	37.32	41.00
Max. Angle(Sec.4)(°)	37.56	40.00

Starting with the foil in the underformed configuration, we compute for two stroke cycles. We extract time histories of M_x and M_z from the second cycle and plot them in

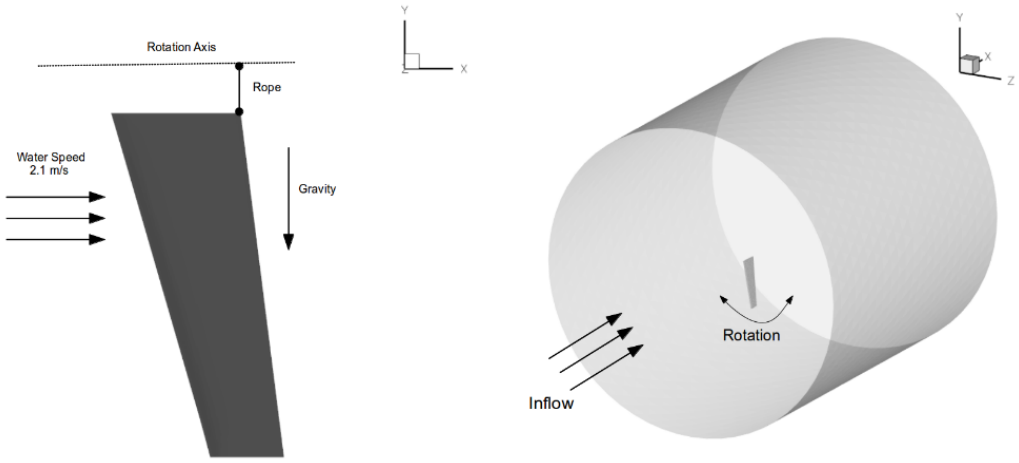

Figure 6.11: (left) Initial configuration of the foil; (right) FSI domain and setup

Fig 6.12 and Fig 6.13, respectively. The maximum predicted M_x is about 41 Nm, while the maximum predicted M_z is about 13 Nm. The experimentally measured data is also plotted in the figures for comparison, and the agreement with the computational results is very good. The averaged drag in the FSI computation is reported in Table 6.6 and compared with the test data. The two drag values are very close. These results suggest that the structural response of the foil to hydrodynamic loads, including its twisting motion, is captured very well in the FSI computation. Time history of the twisting angle at Sections 1-4 on the foil are plotted in Fig 6.15. The locations of these Sections are shown in 6.16. As expected, the cross-sections that are further away from the rotation axis twist more. Table 6.6 summarizes the maximum twist angle for each section predicted by the FSI computation and measured in the experiment. The two data sets match very well, which is further confirmation that the foil twisting action is accurately captured in the FSI simulation. Figure 6.14 shows the foil configurations at four positions in a side-by-side comparison with the underwater photographs of the foil at the same angular-position instances ($\theta = 90°$, $\theta = 0°$,$\theta = -90°$ and $\theta = 0°$) during a motion cycle. Very similar patterns of the deformation are observed between experiment and simulation. This visual comparison reveals very similar deformation patterns between the experimental data and FSI predictions.

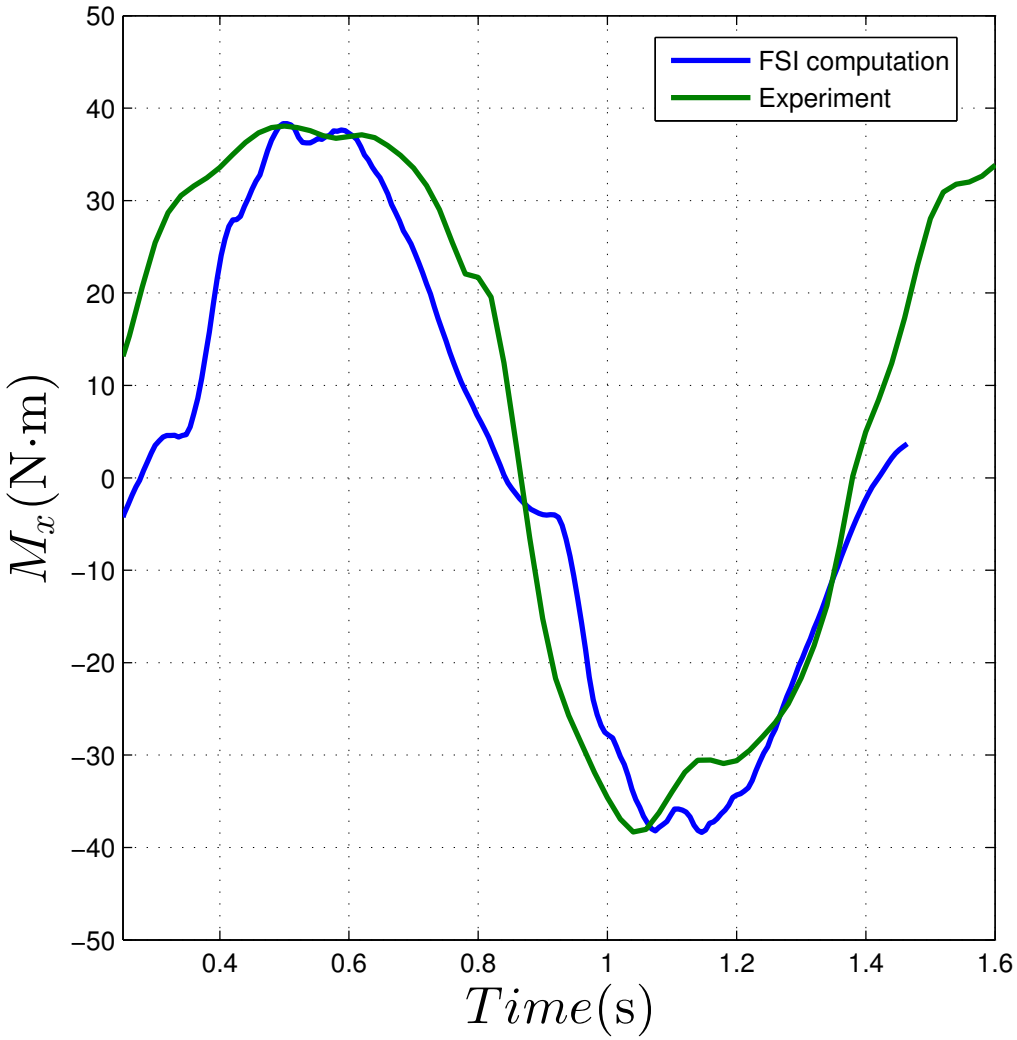

Figure 6.12: Time history of moment in x direction compared with experimental data

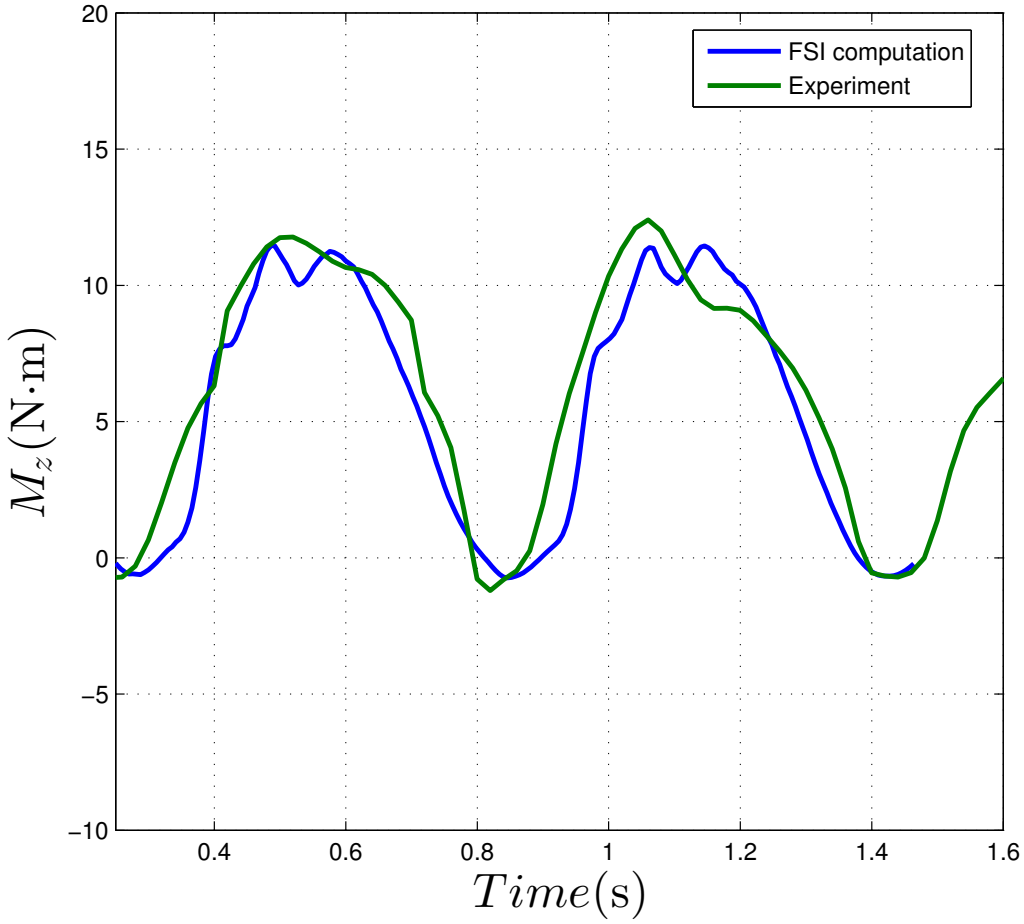

Figure 6.13: Time history of moment in z direction compared with experimental data

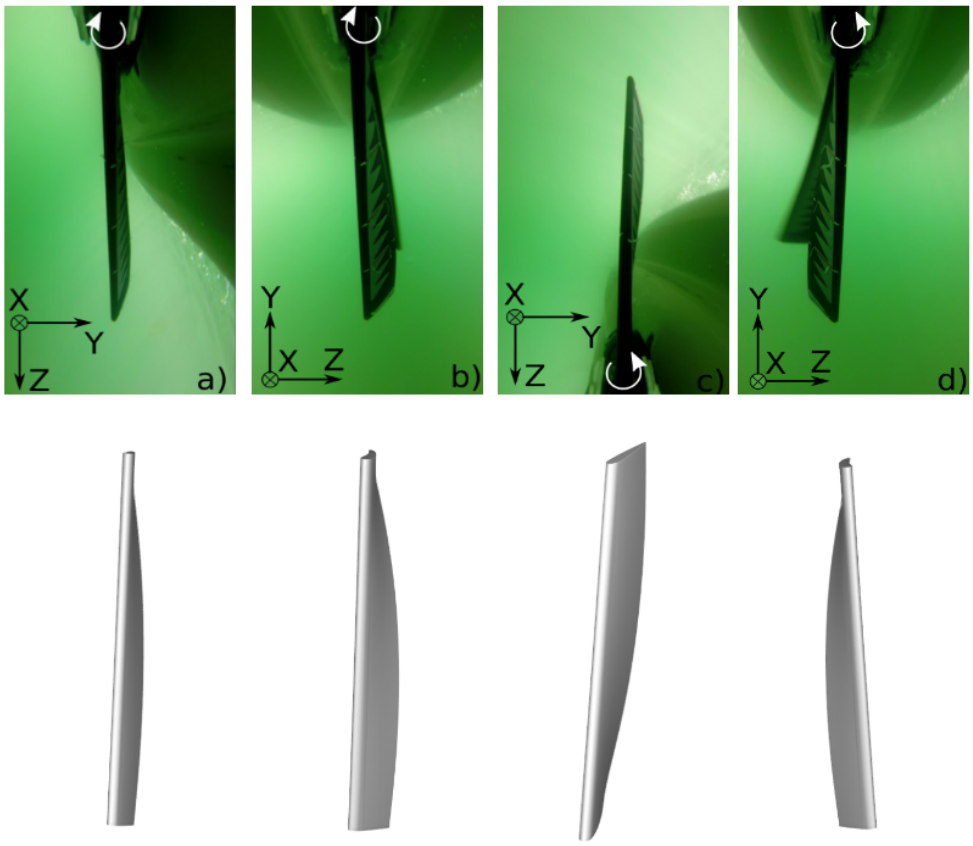

Figure 6.14: Configurations of deformed foil at four different positions

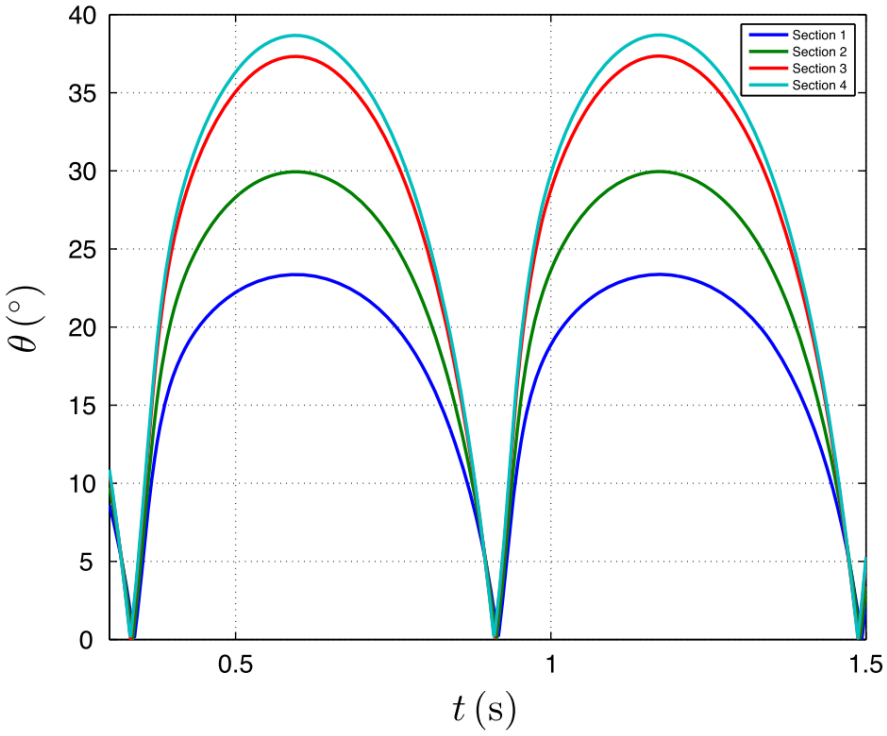

Figure 6.15: Time history of twist angle at five cross-sections

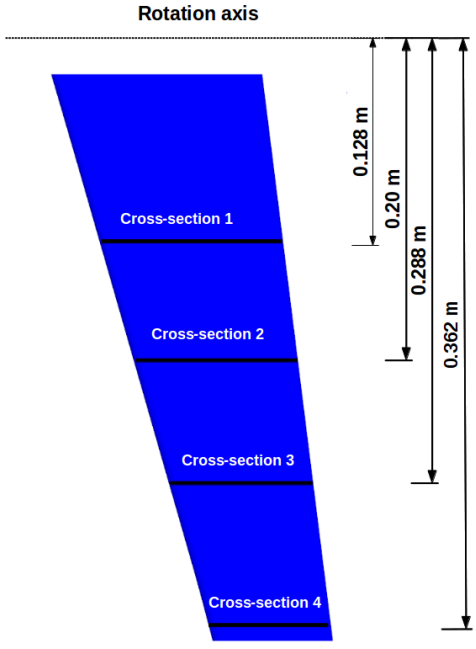

Figure 6.16: Locations of four cross sections

Fig. 6.17 and Fig. 6.18 show the velocity magnitude field and vorticity isosurfaces colored by flow speed close to the foil surface at four instances during the stroke cycle. The figure illustrates the complexity of the underlying wall-bounded turbulent flow phenomena, and underscores the necessity to use advanced FSI modeling and simulation for this problem class.

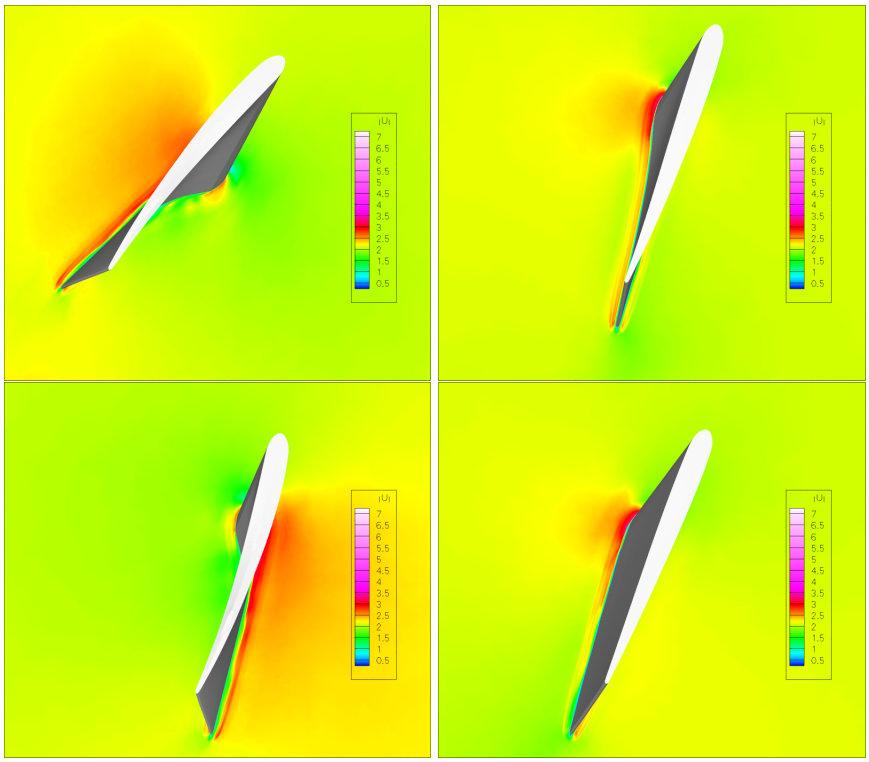

Figure 6.17: Velocity profile at four instants during the stroke cycle

6.1.4 FSI simulation: Two foils in tandem configuration

The FSI simulation of two oscillating foils in tandem configuration is presented in this section. The sliding-interface technique [33, 70, 73] is adopted to handle the relative motions between the front foils and back foils. The field tests of two foils in tandem configuration were performed in the San Diego Bay. Fig. 6.19 shows the times series of M_{xi} and M_{zi}, where $i = 1$ and $i = 2$ correspond to the front and back foil, respectively, and the pedal-bracket load F_p measured for a kayak speed of 2.1 m/s. As expected, the propulsive

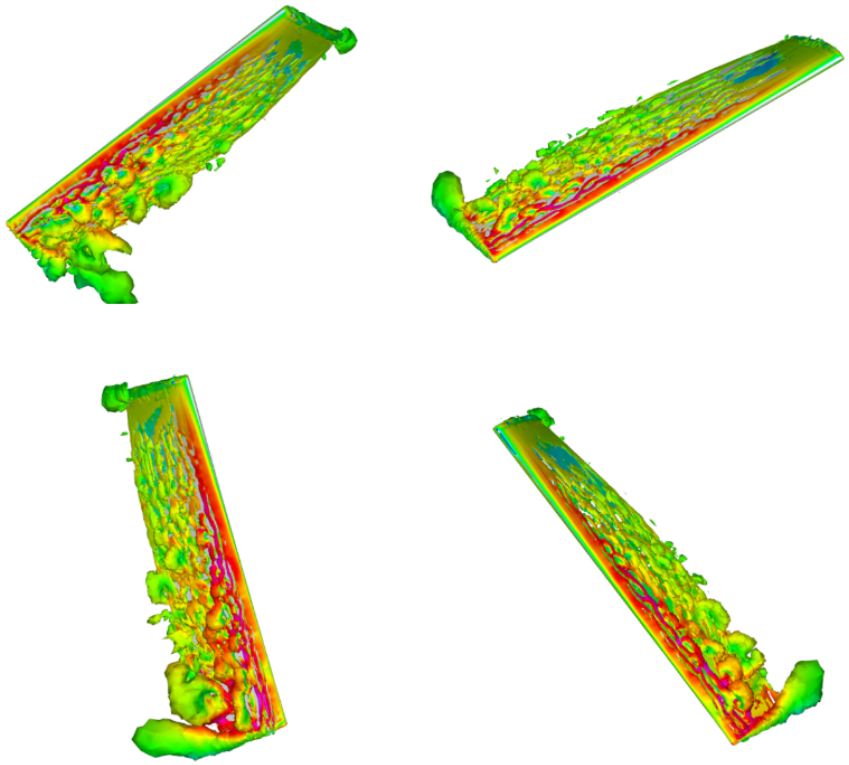

Figure 6.18: Vorticity isosurfaces colored by flow speed at four instants during the stroke cycle

moment M_{zi} is non-negative and has double the frequency of the side moment M_{xi}. Because the kayak is propelled by a human driver, the measured data exhibits some differences from one period to the next. Nevertheless, one trend that clearly emerges is that moments acting on the back foil are generally greater than those acting on the front foil. This finding is novel and indicates that the interaction between the foils in the propulsion system considered in non-negligible.

Problem setup

In present simulation, the front foil and the back foil are identical in terms of geometry and material properties, taken from the single-foil simulation reported in previous section and in [7]. The foil tandem configuration is shown in Fig. 6.20 and the problem

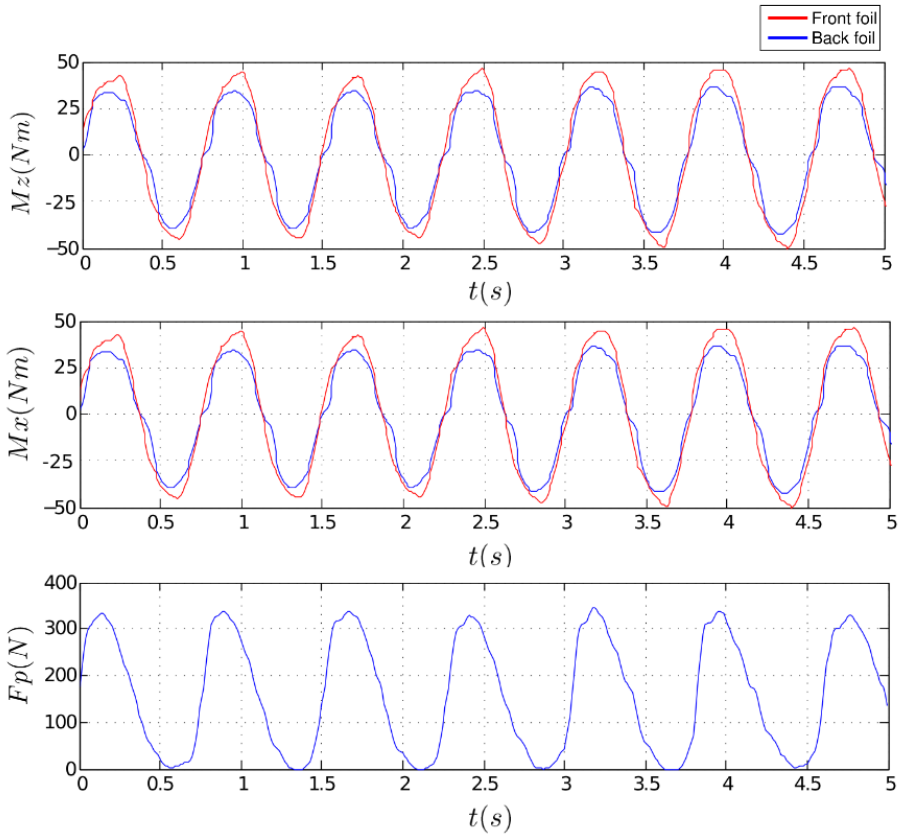

Figure 6.19: Time series of the moments M_{xi} and M_{zi} and the pedal-bracket load F_p measured for a kayak speed of 2.1 m/s

setup is shown in Fig. 6.21. The foils are 0.37 m in length, and clearance between them is 0.0259 m at the top and 0.0772 m at the bottom axial cross-sections. The distance between the rotation axis and top surface of the foils is 0.047 m. The simulation is performed at prescribed steady inlet water speed of 2.1 m/s. To drive the system, time-dependent rotation boundary conditions are applied on the leading edge of each foil. Rotation angles for the front and back foils are given by

$$\theta_F(t) = \frac{A\pi}{2} sin\left(\frac{2\pi t}{T}\right) \tag{6.6}$$

$$\theta_B(t) = -\frac{A\pi}{2} sin\left(\frac{2\pi t}{T}\right) \tag{6.7}$$

respectively. In the above equations $\frac{A\pi}{2}$ and T give the maximum rotation angle and stroke period, respectively. In the simulation of this two foils simulation, we set $A = 0.6501$ and $T = 0.6821$ s, which are also typical conditions for high-speed cruising, and which are also consistent with the field test results presented above.

The connection between the foil top-cross-section trailing edge and rotation axis is modeled using isogeometric cable structures [115]. The cables are loosened by giving them a slightly curved initial configuration profile. This setup mimics the actual attachment mechanism of the foil trailing edge to the rotation axis, and allows the foils to develop higher twisting angles needed for efficient propulsion. Each cable has one end attached to the rotation axis and the other to the trailing edge of the foil top cross-section (see Fig. 6.20). The cables are discretized using a single quadratic NURBS element. We note that cable elements are employed with the sole purpose to appropriately constrain the foil trailing-edge motion. Cable elements do not receive forces from the fluid, nor do they affect the fluid kinematics. The fluid mechanics domain and mesh are designed as follows. The domain boundary is a cylinder with radius of 0.96 m and length of 1.5 m. A refined cylinder is built around the foils in order to better capture the turbulence generated by the foils.

To perform the simulation of compliant foils in tandem configuration and capture the interaction between the front foil and back foil, the fluid domain is divided into two parts

separated by a sliding interface as shown in Fig 6.22. In Fig 6.22, one subdomain contains the front foil while another subdomain encloses the back foil. As the front foil and back foil rotate in opposite directions, the corresponding subdomains rotate with them, also in opposite directions, which creates a sliding interface between the two subdomains. The compatibility conditions enforced at the sliding interface are

$$\boldsymbol{u}_F^h - \boldsymbol{u}_B^h = \mathbf{0} \tag{6.8}$$

$$\left(-p_F^h \boldsymbol{I} + 2\mu\varepsilon(\boldsymbol{u}_F^h)\right)\boldsymbol{n}_F + \left(-p_B^h \boldsymbol{I} + 2\mu\varepsilon(\boldsymbol{u}_B^h)\right)\boldsymbol{n}_B = \mathbf{0} \tag{6.9}$$

where all quantities with subscripts 'F' and 'B' refer to the front and back subdomains, respectively, and $\boldsymbol{n}_F$ and $\boldsymbol{n}_B$ are the unit outward normal vectors of the interface on each side. We choose a cone-shaped sliding interface, which makes the trailing edge of the front foil and leading edge of the back foil nearly equidistant from the interface. The sliding-interface mesh is shown in Fig. 6.24. The elements are clustered toward the cone center to have a more accurate representation of the interaction between the foils. The mesh gradually coarsens toward the lateral boundaries where the flow is uniform. The volume mesh makes use of triangular prisms in the foil boundary layers (see Fig. 6.23), and tetrahedra elsewhere. The mesh statistics are summarized in Table 6.7. Uniform inflow velocity is imposed strongly at the inlet. No penetration and zero streamwise-traction boundary conditions are applied on the cylinder lateral surfaces. Zero traction boundary conditions are imposed at the outlet. The computation is performed in a parallel computing environment. The fluid mesh is partitioned into subdomains using METIS [84, 85], and each subdomain is assigned to a compute core. The parallel implementation methodology employed may be found in [67]. The time step is set to $\Delta t = 1.5 \times 10^4$ s, and the simulation is performed for two stroke cycles.

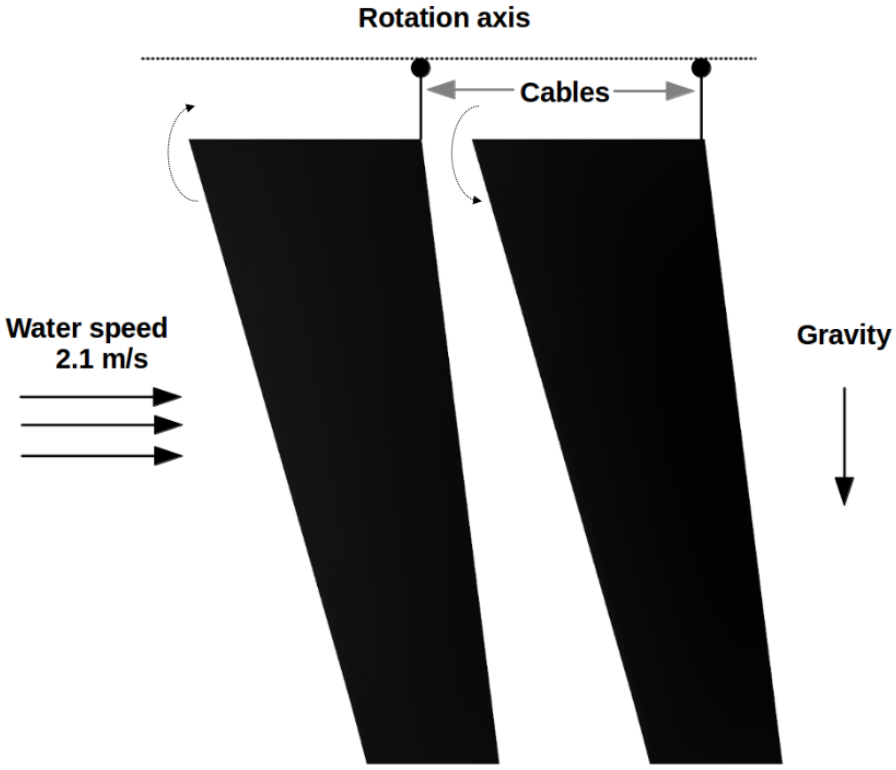

Figure 6.20: Side view of the tandem foil configuration

Table 6.7: Number of nodes and elements of fluid mechanics domain

Num. of nodes	Num. of elements
550,557	2,224,857

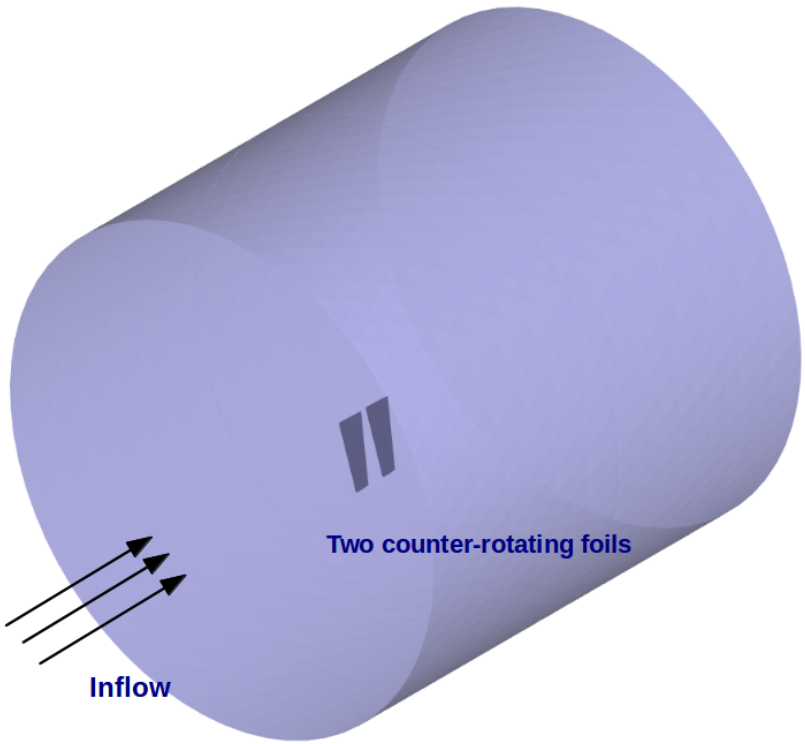

Figure 6.21: Computational domain and problem setup

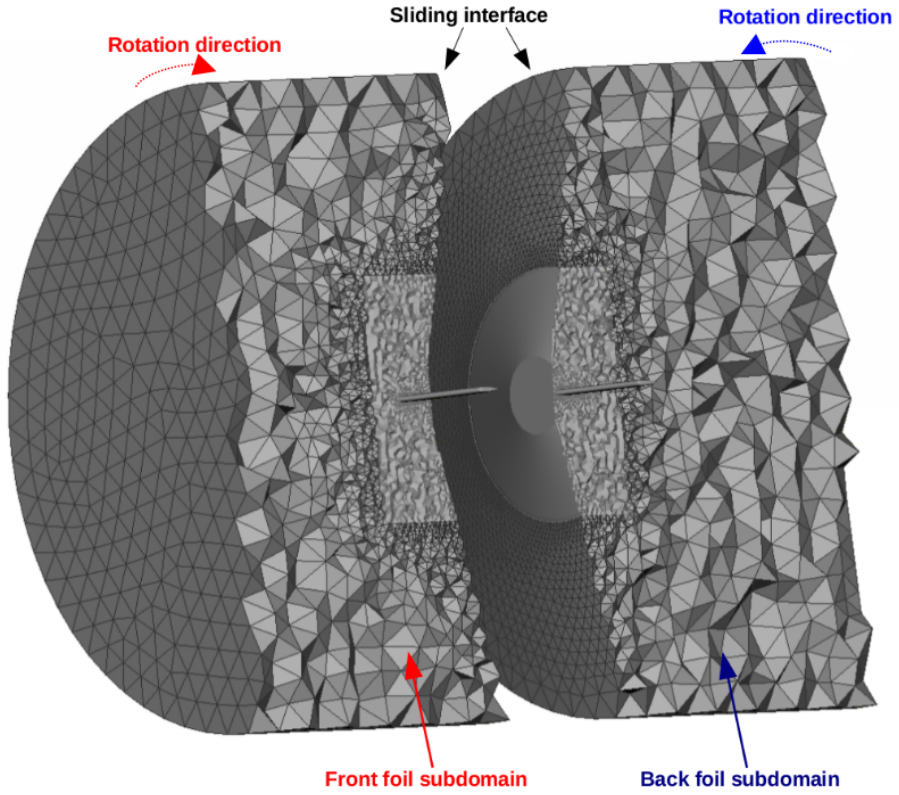

Figure 6.22: Fluid mechanics domain and mesh with a sliding interface shown. The front and back subdomains are artificially separated for illustration purposes

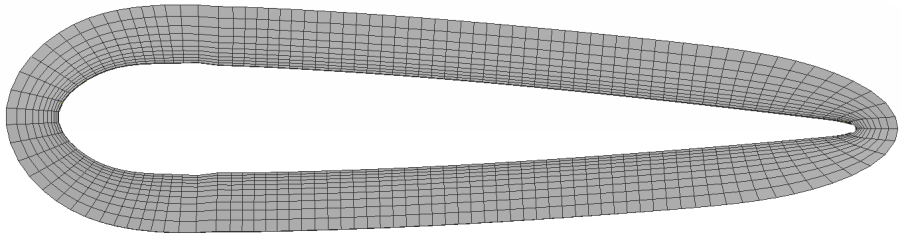

Figure 6.23: Triangular-prism discretization of the foil boundary layers

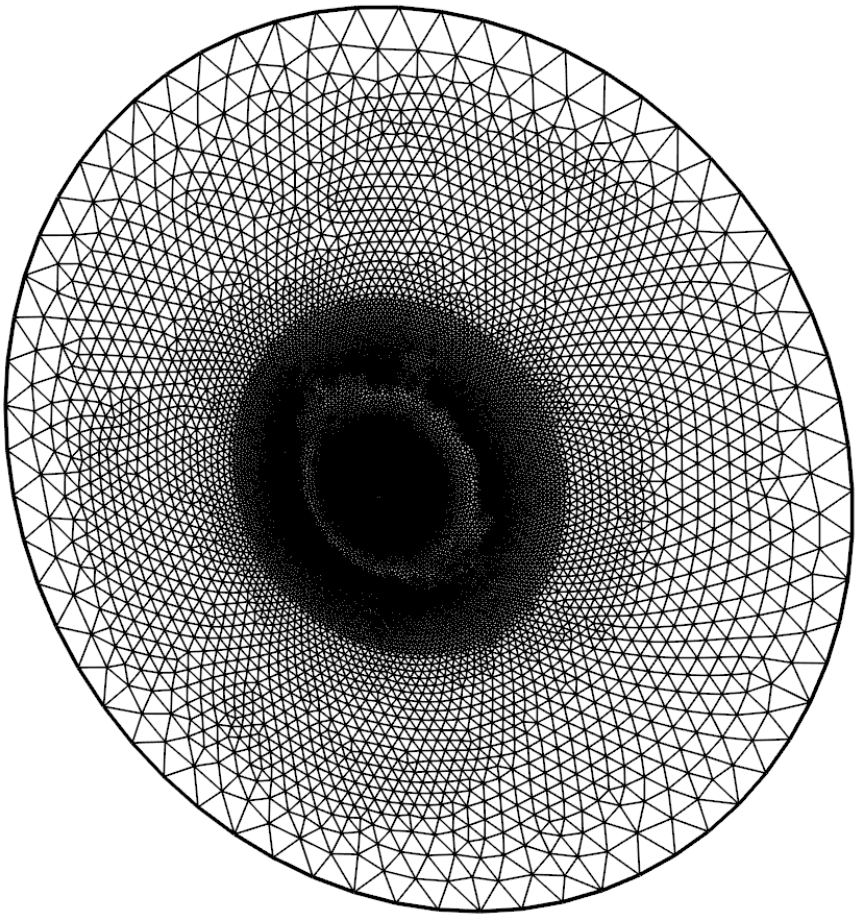

Figure 6.24: Triangular mesh of the sliding interface

FSI simulation results and discussions

Time histories of the computed and measured hydrodynamic moments M_{xi} and M_{zi} are plotted in Fig 6.25. Good agreement both in the hydrodynamic moment magnitude as well as other trends in the moment time history is achieved between the computational results and field test data. When the foils are separated by a large distance, they barely feel each others presence, and the hydrodynamic moments acting on the foils are nearly identical. However, when the foils cross each other, strong interaction between them can be observed, especially in the moment curves coming from the FSI simulation. One important trend that is observed experimentally and reproduced in the computation is that during the entire stroke cycle moments acting on the back foil are greater than or equal to those acting on the front foil. Time histories of the twist angle at four different cross sections along the foil axis are plotted in Fig. 6.26. The cross-section locations are indicated in Fig. 6.16. The maximum twist angle during the stroke cycle is in excellent agreement with the experimental data. Although fairly significant differences in the hydrodynamic moments were observed between the front and back foils, this is not the case for the twist angle. For both foils time histories of the twist angle are very similar, with difference on the order of 1° observed right after the foils cross each other. The difference in the twist angle becomes more pronounced closer to the foil tip where the maximum twist occurs. The curves suggest that the back foil twists more than the front one, which is consistent with the moment curve trends discussed in the previous paragraph. The higher twist of the back foil decreases the flow angle of incidence leading to slight enhancement of its propulsion efficiency.

Fig. 6.27 shows time instances of the fluid velocity vectors on a cut plane superposed on foils in deformed configuration and colored by fluid pressure. These correspond to instances before, during, and after the crossing event. Changes in the flow velocity patterns as the foils get closer to one another are clearly visible. Significant twisting of the foils may also be observed in the figure. Fig 6.28 shows time instances of vorticity isosurfaces colored by flow speed, also before, during, and after the crossing event. Significant vorticity is generated on the suction side of the foil accompanied by massive flow separation. On the pressure side the the flow appears to be attached and very little vorticity is present. The

complexity of the underlying wall-bounded turbulent flow is also clearly seen in the figure, which underscores the necessity to use advanced FSI simulation techniques for this problem class

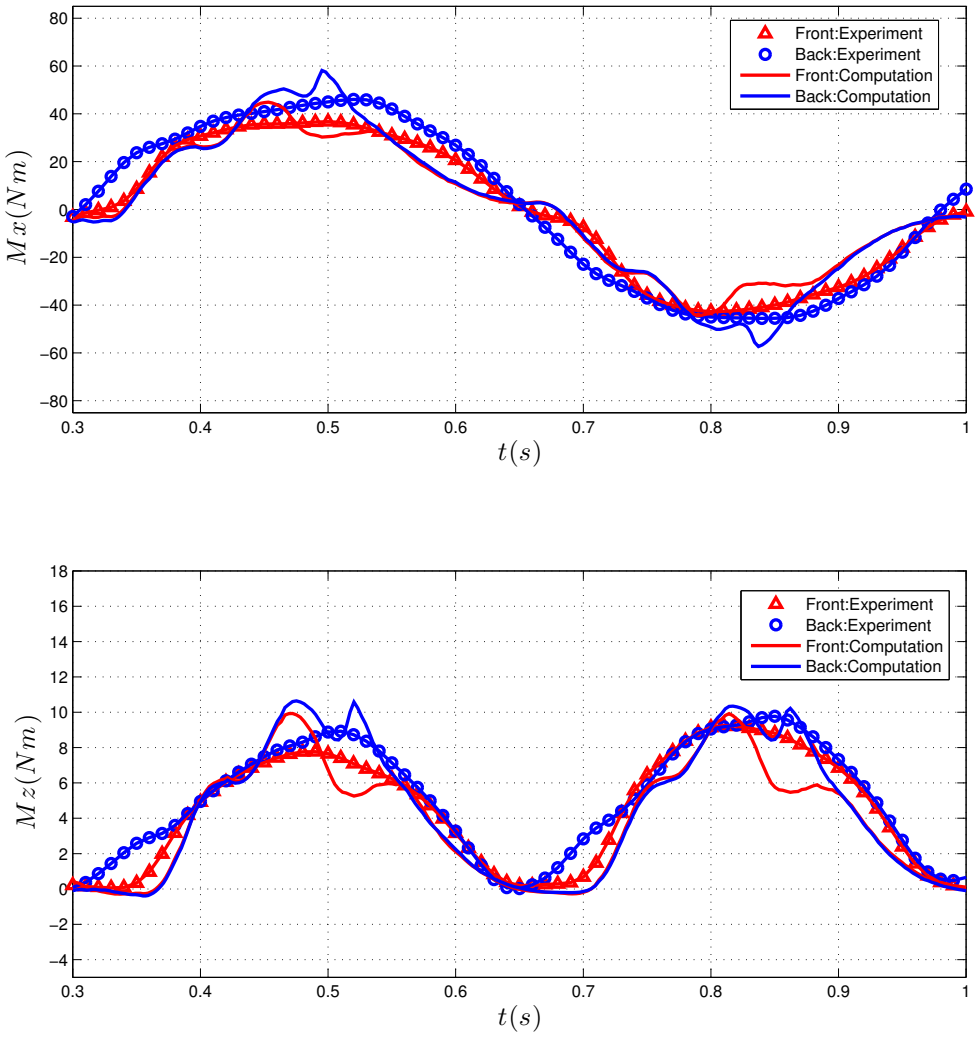

Figure 6.25: Time history of hydrodynamic moments M_{xi} and M_{zi}. Both experimental and computational results are plotted for comparison

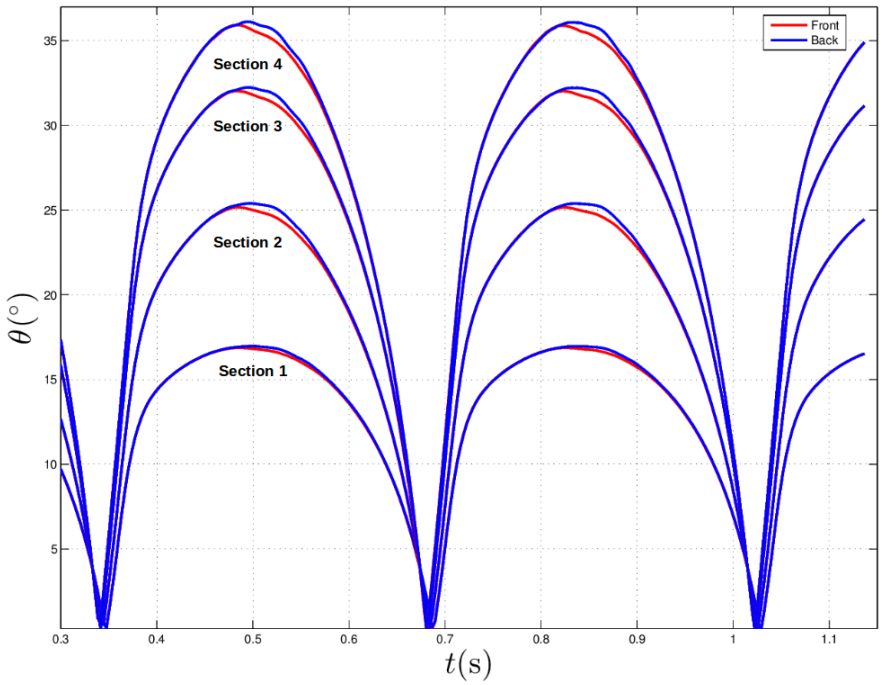

Figure 6.26: Time history of twist angle of four cross sections

6.2 Full-scale offshore floating wind turbines

In this section, we apply the free-surface FSI methodology on offshore floating wind turbines. While a number of floating platforms are proposed for offshore floating wind turbines in recent years, including sparing-buoys, tension leg platforms, barges and hybrid concepts [80], in this paper, the ”OC3-Hywind” floating system, which is defined in [82], is simulated at full scale with non-spinning rotor. The whole floating wind turbine consists of a supporting spar-buoy called “Hywind”, developed by Statoil of Norway, and a NREL 5-MW baseline turbine. This concept was chosen for its suitability for modeling and existence of a full-scale prototype [82, 80]. For the present simulations we consider the rotor in the so-called “parked” configurations, meaning that it is not spinning.

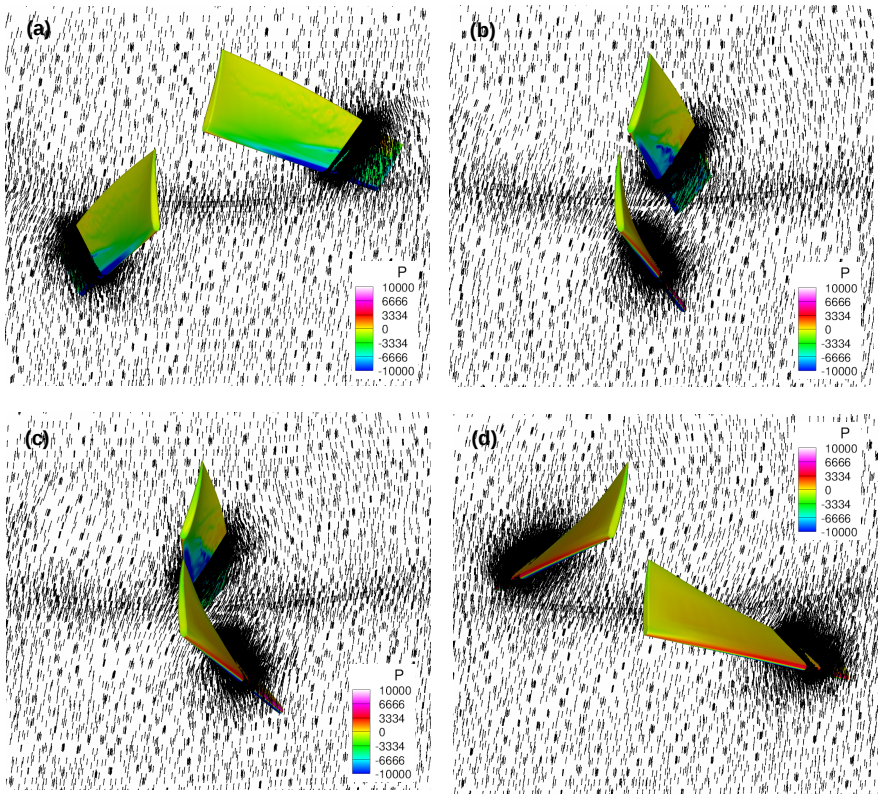

Figure 6.27: Fluid velocity vectors on a cut plane superposed on foils in deformed configuration colored by fluid pressure (in Pa)

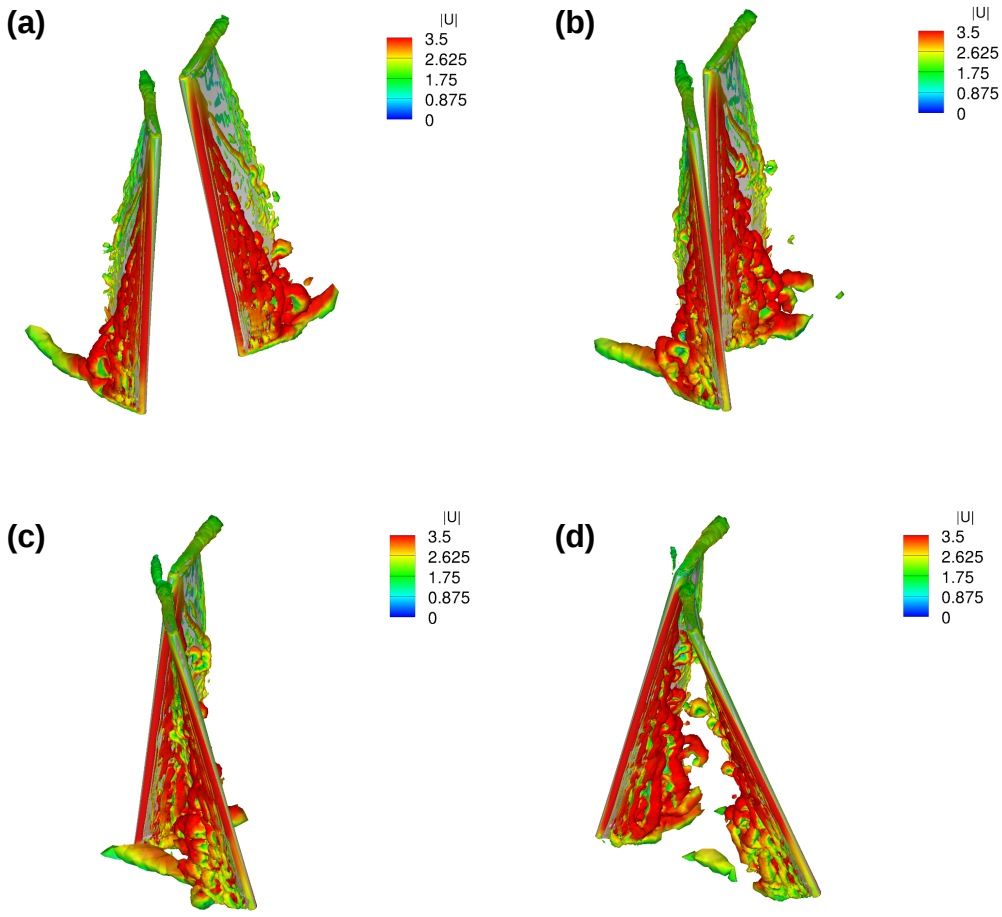

Figure 6.28: Vorticity isosurfaces colored by flow speed (in m/s)

6.2.1 Wind-turbine geometry and materials

The wind-turbine structure consists of a supporting spar buoy developed by Statoil, the NREL 5MW baseline wind turbine mounted on the spar-buoy, and mooring cables attached to the spar-buoy and anchored to the seabed. This concept was chosen due to its relative ease of modeling, as well as due to the existence of a full-scale prototype operating in the North sea [80, 82]. The NREL 5-MW wind turbine is a conventional three-blades design proposed in [79] to support concept studies aimed at assessing offshore wind technology [81, 83, 97, 65, 50, 96, 121]. The FSI and aerodynamics simulations of rotor-only configuration of this wind turbine using IGA and standard FEM can be found in [23, 27, 130, 128, 31, 28, 69, 67, 37], while the FSI simulations of the full machine are recently reported in [73, 34, 142].

The geometry of the complete floating structure is defined as follows. The rotor has a diameter of 126 m. The base of the tower is located at an elevation of 10 m above the still-water level, and reaches the height at the top of 87.6 m above the still-water level. The distance from the sill-water level to the main-shaft centerline is 90 m. The tower has diameter of 6.5 m at the base and 3.87 m at the top, with a linear variation in between. The platform consists of two cylindrical regions, of lengths 14 m and 108 m, and diameters 6.5 m and 9.4 m, respectively, connected by a linearly tapered conical region extending from 4 m to 12 m below the still-water level. Three mooring cables with length of 902 m are attached to the platform 70 m below the still-water level, and are anchored to the seabed at 320 m below the still-water level. The complete floating-turbine structural system is depicted in Fig. 6.29.

The main structural components, namely, the rotor, nacelle, tower and platform, are constructed using the total of 14,709 quadratic NURBS shell elements, while the main shaft and mooring cables are constructed using 33 quadratic NURBS beam/cable elements.

For the current simulations, instead of the originally proposed wind turbine blade design [79], we use a scaled-down version of the SNL 10000 offshore wind turbine blade (scaled down from 100 m to 61 m) designed by the Sandia National Laboratories [61]. The scaled-down version makes use of the same NACA and DU series airfoils as in the

originally proposed 5 MW design. The main modifications, as compared to the original design, include leading and trailing-edge reinforcements, and three shear webs placed to minimize the length of the unsupported panel.

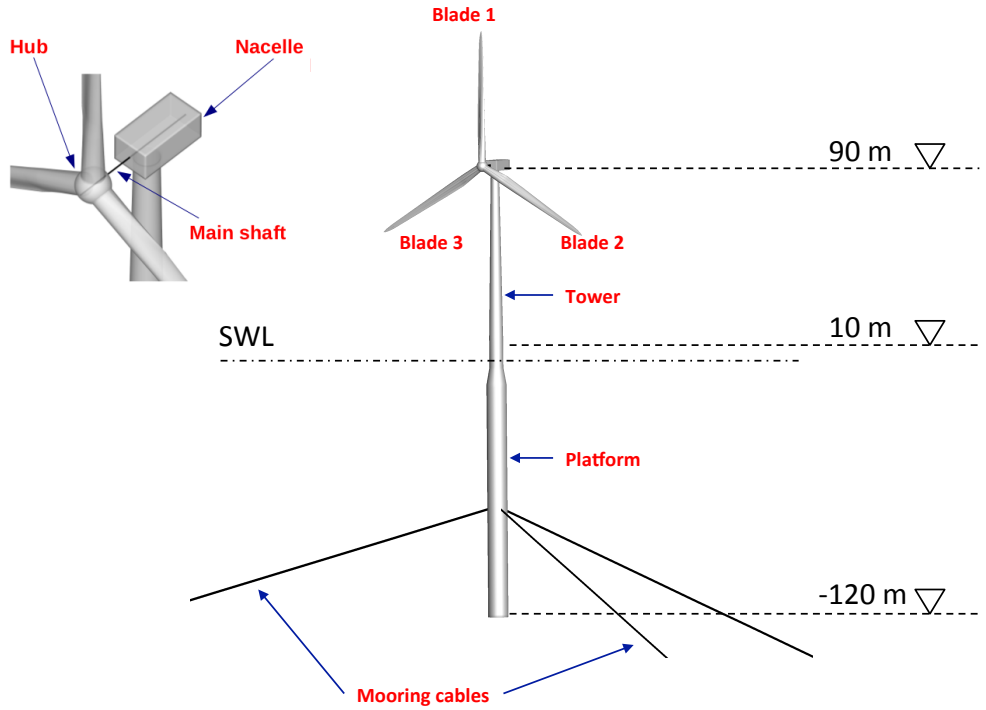

Figure 6.29: Structural model of floating wind turbine with zoomed view on a rotor.

Figure 6.30: Cross-sections of the SNL 10000 blade showing six principal regions. Red: Trailing edge reinforcement; Cyan: Leading edge reinforcement; Blue: Shear web; Magenta: Spar caps; Green: Aft panel

The blade laminate has six principal regions: root, spar cap, trailing edge reinforcement, leading edge panels, aft panels and shear webs, as shown in Fig. 6.30. Table 6.9 list

Table 6.8: Masses of main structural components of floating wind turbine

Part	Rotor	Hub	Nacelle	Tower	Platform	Cables	Total
Mass (kg)	78,895	43,559	229,504	247,155	7,427,624	210,321	8,237,058

Table 6.9: Geometric and Material Properties of Structural Components

Part	Young's Modulus E (GPa)	Poisson's ratio ν_{12}	Density ρ (kg/m^3)
Hub	1000	0.33	7800
Nacelle	1000	0.33	7800
Tower	210	0.33	8500
Platform	210	0.33	8700
Cables	195	NA	12.215

the materials used in the blade design. The root buildup is composed of triaxial material (SNL Triax), and all internal and external blade surfaces have a 5 mm layer of this material. As the root buildup tapers down in thickness, the spar cap increases in thickness. The maximum thickness of the spar cap is 136 mm at maximum chord (19.5%), while the minimum thickness of the spar cap is 5 mm, starting at 94.4% of the blade span and continuing almost all the way to the tip. The trailing edge is reinforced with uniaxial laminate E-LT-5500/EP-3 and foam materials. The trailing edge reinforcement has a constant width of 1.0 m that continues until 94.4% span, and then tapers to the tip. To improve buckling resistance and minimize the weight, foam is also chosen as the core material for the leading panel and aft panels. Longitudinal fibers of E-LT-5500/EP-3 are placed on the spar cap to improve the flapwise bending stiffness. The spar cap has a constant width of 1.5 m. As a result, the two principal shear webs, which begin at 2.4 m and terminate at 94.4 m, are positioned 0.75 m before and after the pitch axis. The third shear web starts at 14.6 m and terminates at 60.2 m, and is positioned at 78% chord at its starting location and 68% chord at its terminal location. A combination of foam and Saertex/EP-3 is used in shear webs to enhance the shear stiffness. An extra 5 mm of epoxy resin is included in the internal blade surface, and the external surface includes 0.6 mm of gelcoat. The same layup is employed for both low- and high-pressure blade surfaces.

To verify the blade model construction, and to select the appropriate blade mesh

resolution for the FSI computations, we first carried out its natural frequency analyses. Three meshes using ,1,166, 3,568 and 7,416 quadratic NURBS elements, referred to as coarse, medium and fine, respectively, were created. The eigen frequencies for the three meshes are summarized in Table 6.11, and compared with the simulation results using beam theory reported in [48]. Good agreement is achieved for all eigenfrequencies reported. The corresponding eigenmodes are presented on Figure 6.32. The results of this analysis indicate that the medium mesh is more than adequate for the FSI analysis, which we present in the next section. The total mass for medium mesh is equal to 115,969.3 kg, while the reference value is 114,172.0 kg. Very good agreement is observed in all the quantities reported.

The masses of all wind-turbine structural component are listed in Table 6.8, while the material properties of these components are summarized in Table 6.9.

Table 6.10: Orthotropic and isotropic materials used in the SNL 100-00 blade

Material Type	Lay-up	E_1 (GPa)	E_2 (GPa)	G_{12} (GPa)	ν_{12}	Density (kg/m^3)
E-LT-5500/EP-3	$[0]_2$	41.8	14	2.63	0.28	1920
Saertex/EP-3	$[^{\pm}45]_4$	13.6	13.3	11.8	0.51	1780
SNL Triax	$[^{\pm}45]_4[0]_2$	27.7	13.65	7.2	0.39	1850
Foam	[0]	0.256	0.256	0.022	0.3	200
Resin	[0]	3.5	3.5	1.4	0.3	1100
Gel Coat	[0]	3.44	3.44	1.38	0.3	1235

Table 6.11: SNL 100-00 blade natural frequencies. The IGA computational results are compared with the reported values from [48]. The values from the reference do not come from actual experiments, but from a beam model of the same blade

Mode Number and Type	Results from SNL Report (Hz)	IGA Results (Hz)		
		Coarse Mesh	Medium Mesh	Fine Mesh
1st Flapwise Bending	0.42	0.456	0.454	0.453
1st Edgewise Bending	0.69	0.681	0.678	0.679

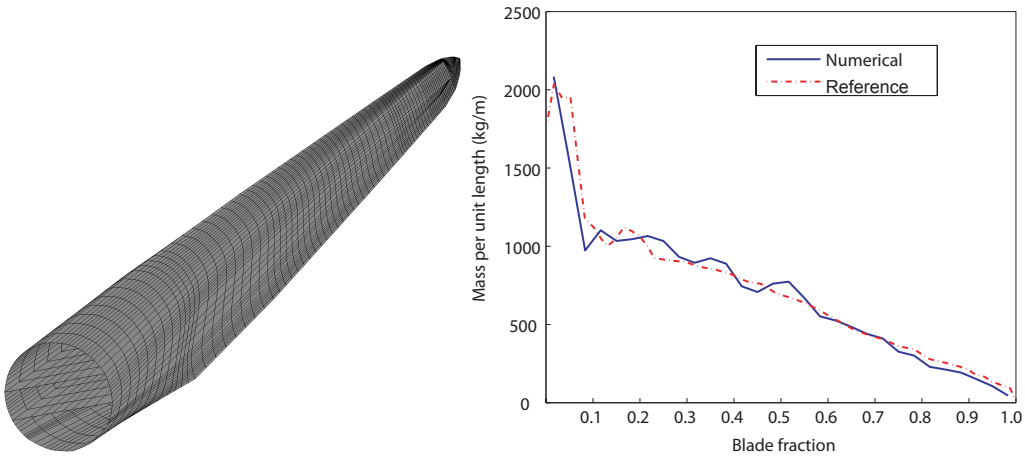

Figure 6.31: Left: SNL 100-00 blade medium NURBS meshes. Right: SNL 100-00 blade mass distribution along the blade axis. Data from [61] are plotted for comparison

Figure 6.32: Eigenmodes of SNL 100-00 blade. Left: 1st bending mode; Right: 1st edgewise mode

6.2.2 FSI simulation: Airy wave conditions

The first simulation of the OC3-Hywind offshore floating wind turbine is performed using the linear Airy wave theory [109] as input. The Airy wave can also be derived using potential flow theory, and specified as follows: given the wave height H, wave length L and water depth h, we compute wavenumber $k = \frac{2\pi}{L}$ and wave phase speed $\omega = \sqrt{gk\tanh(kh)} + kU_{in}$. With these definitions, the Airy wave profile is given by

$$\phi = \frac{H}{2}\cos(kx - \omega t) + h - z \tag{6.10}$$

$$u = \frac{wH}{2\sinh(kh)}\cosh(kz)\cos(kx - \omega t) + U_{in} \tag{6.11}$$

$$v = 0 \tag{6.12}$$

$$w = \frac{wH}{2\sinh(kh)}\sinh(kz)\sin(kx - \omega t) \tag{6.13}$$

where (u, v, w) is the velocity field and U_{in} is the mean flow speed. In this simulation, we set U_{in} = 0 m/s, H = 6 m and L = 156.13 m. The still water level (SWL) is set at z = -30 m. The corresponding wave period $T = \frac{2\pi}{\omega}$ is 10 s.

The fluid mechanics computational domain an mesh of are defined as follows. The computational domain is a box with the dimensions of 550 m × 200 m × 480 m. A refined box is designed around the air-water interface to better capture the evolution of the free-surface. The top and bottom surface of the refined box is 5 m above and below the still water level. The domain is meshed with tetrahedral elements and shown in Fig. 6.33. The mesh statistics are listed in Table 6.12 and Table 6.13. The floating wind turbine is located 150 m away from the inlet. The wave profile with the parameters given above is strongly imposed at the inlet. At lateral and bottom surfaces, no penetration boundary condition is used. Top surface is opened to o the hydrostatic pressure boundary conditions. Finally, zero traction boundary condition is applied at the outlet. For the structural mechanics, all the degrees of freedom are enabled except the three control points of the mooring cables which are anchored at the seabed. The simulation is performed using the time step Δt = 0.005 m.

Figure 6.34 shows the free-surface when the wave is impacting the turbine. The time

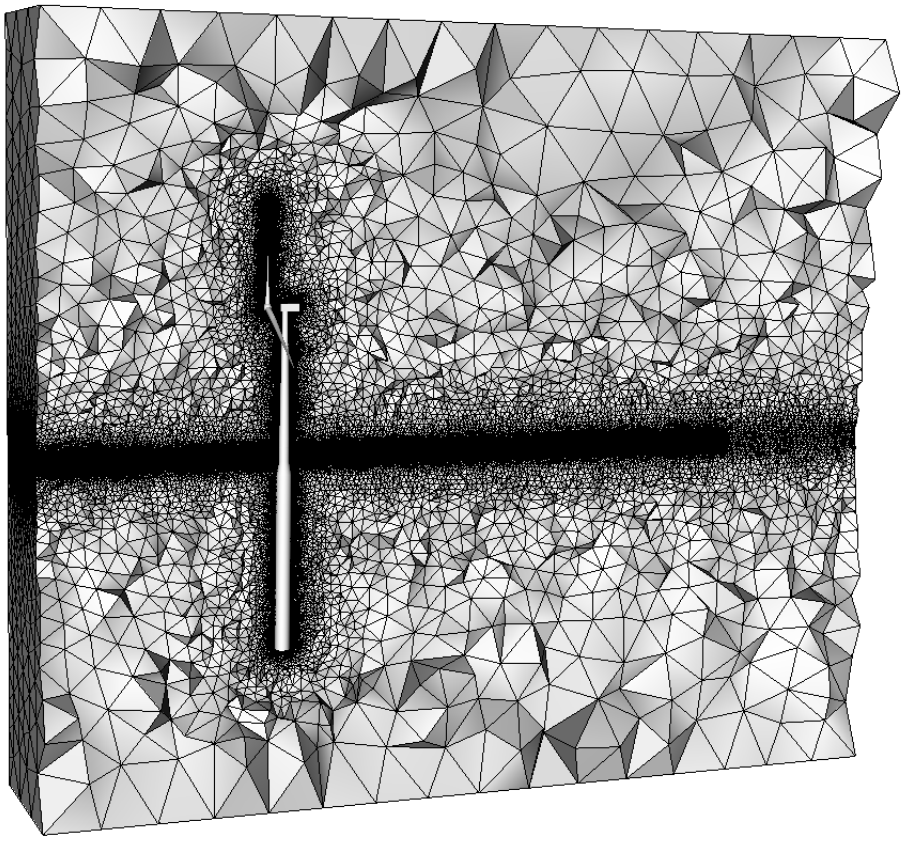

Figure 6.33: Computational domain mesh of floating wind turbine FSI problem

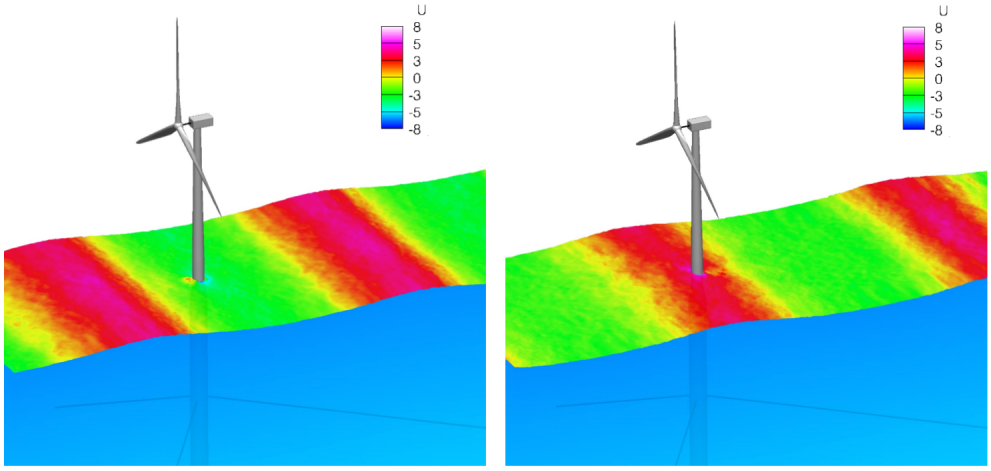

Figure 6.34: Snapshots of the free surface, colored by streamwise velocity, at the instants when the wave trough (left) and peak (right) are passing the platform

Table 6.12: Number of nodes and elements

Num. of nodes	Num. of elements
4,216,201	24,817,979

history surge displacement and heave displacement of the center of mass of the platform are plotted in Figure 6.35. In order to report this quantity, the displacements of the center of mass of the platform are calculated as

$$\boldsymbol{dp} = \frac{\int_{\Omega_p} \rho_p (\boldsymbol{x}_p - \boldsymbol{X}_p)\, d\Omega}{\int_{\Omega_p} \rho_p \, d\Omega} \tag{6.14}$$

where Ω_p is the domain of the platform, ρ_p is the density of the platform, $\boldsymbol{x}_p$ and $\boldsymbol{X}_p$ are current position and initial position of the platform. The simulation results obtained by NREL using their lumped-parameter ADAMS code [80] are also plotted in Figure 6.35 as a reference. Although the NREL data is obtained from the simulation with no rotor configuration, good agreement is still achieved. This is not surprising, since the rotor mass is low compared to the overall mass of the floating turbine. Furthermore, wind loading on the rotor is also very low due to zero-wind-speed conditions employed in the simulation.

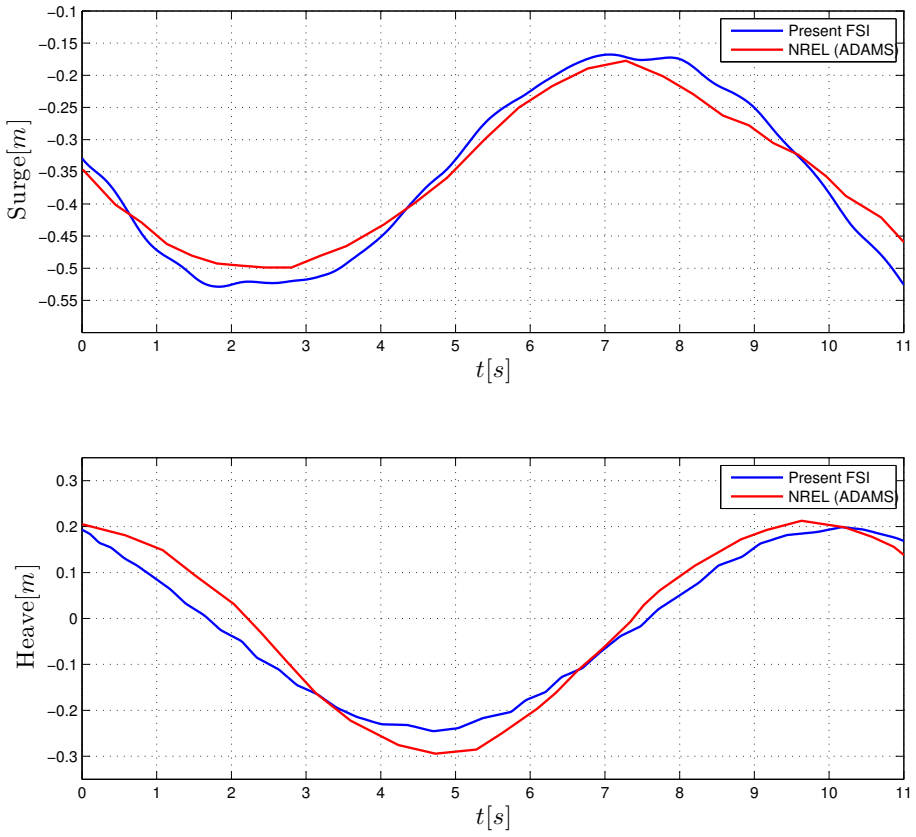

Figure 6.35: Platform center-of-mass displacement time histories for Airy wave conditions

Table 6.13: Element size employed

Outer box	Refined box	Floating wind turbine
30 m	0.8 m	0.1 m-0.5 m

6.2.3 FSI simulation: Violent sea state

Although linear wave theory is often used to model ocean waves, it is insufficient to model more violent sea states. To generate more realistic, higher-amplitude waves for the wind-turbine FSI simulations, a piston-type wave generation concept, which is widely used in offshore engineering research laboratories to generate irregular waves, is utilized in this work, but in a pure numerical setting. We simulate the piston motion by prescribing a time-periodic horizontal displacement to the inlet plane of the computational domain. Such motion results in geometric changes in the computational domain, which are naturally accounted for in our moving-domain FSI framework. In conjunction with the moving inlet plane we impose no-penetration boundary conditions for the flow field in this location, which results in the formation of waves whose amplitude and period may be controlled.

The domain of the numerical tank is designed similarly to the computational domains defined in previous sections. The dimensions of outer box are 600 m × 300 m × 400 m. The top surface and bottom surface of the refined box is 20 m above and 18 m below the still water level, respectively. The domain is meshed with tetrahedral elements and depicted in Figure 6.36. The statistics are listed at Table 6.14 and Table 6.15. The computational setup of the numerical wave tank is illustrated in Figure 6.37. The displacement of inlet (i.e., piston) is specified by the following expressions,

$$S_x(t) = \frac{A_x}{2}\sin(\frac{2\pi t}{T}) \tag{6.15}$$

$$S_y(t) = 0 \tag{6.16}$$

$$S_z(t) = 0 \tag{6.17}$$

where A_x is the magnitude of stroke of the piston and T denotes the period. In present simulation, we set $A_x = 9$ m and $T = 8$ s. The time step, Δt, is set to 0.015 s, and the simulation is performed with 192 processors for 40 s, which corresponds to 5 strokes.

Figure 6.38 shows the deformed free-surface colored by streamwise velocity at t = 8 s, t = 16 s, t = 24 s and t = 32 s. From Figure 6.38, we note that, compared to Airy wave, the waves generated by this piston-type numerical wave tank do not have constant wave length

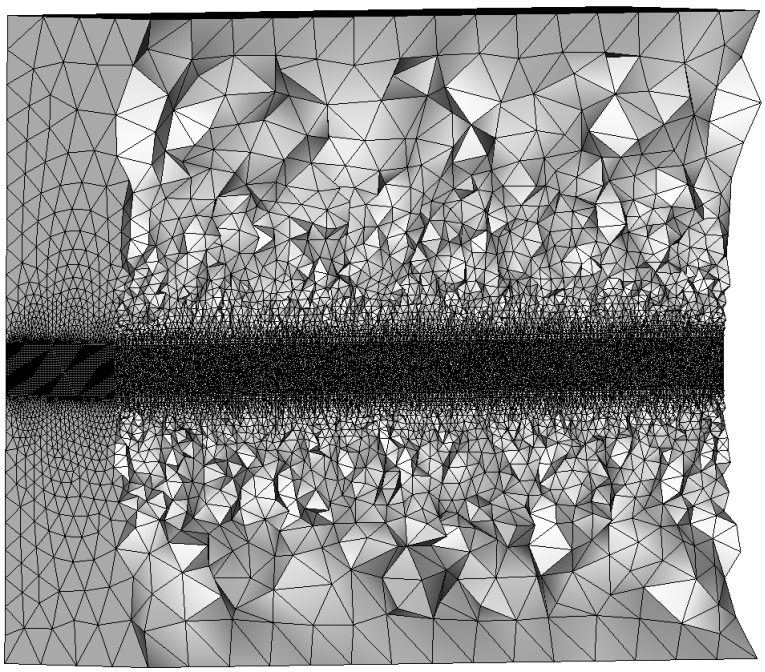

Figure 6.36: Mesh of numerical wave tank

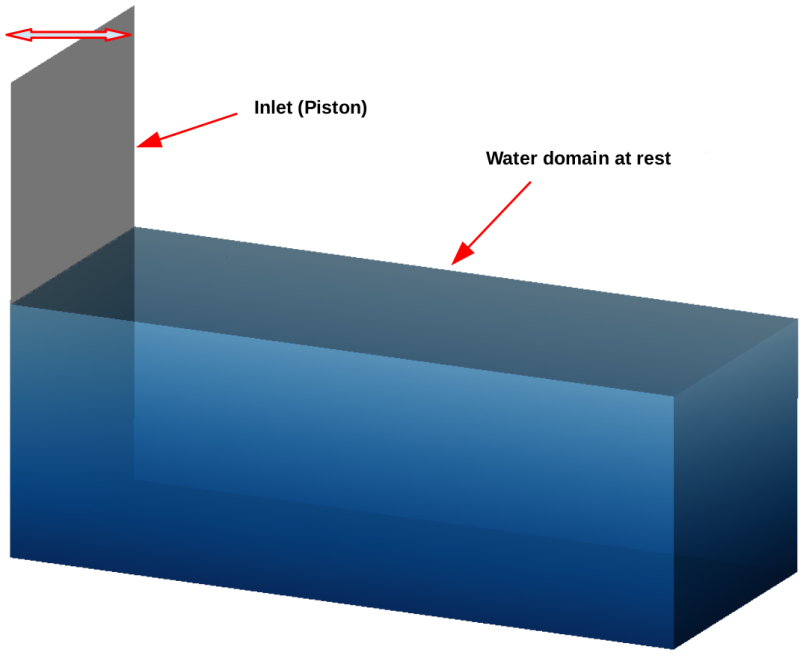

Figure 6.37: Computational setup of piston-type numerical wave tank

Table 6.14: Number of nodes and elements

	Num. of nodes	Num. of elements
Mesh	2,143,125	12,577,489

Table 6.15: Element length

Outer box	Refined box
30 m	1.8 m

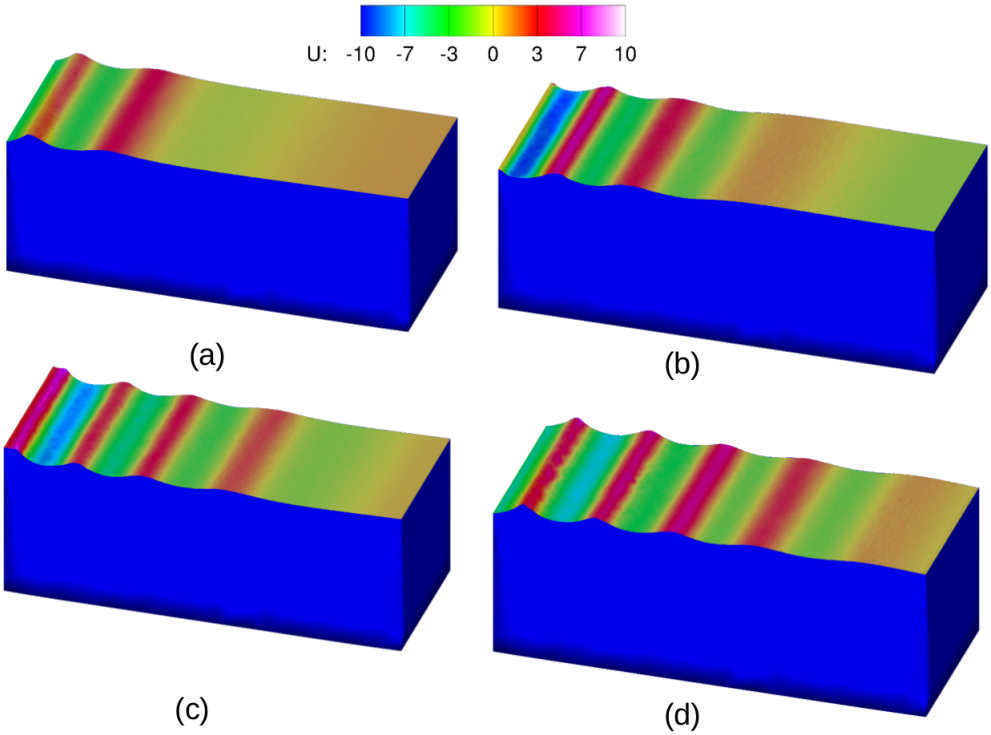

Figure 6.38: Snapshots of the free surface colored by streamwise velocity (m/s) at different times: (a) t = 8 s; (b) t = 16 s; (c) t = 24 s; (d) t = 32 s

Figure 6.39: Two numerically generated wave conditions used for floating wind-turbine FSI simulations. Top profile corresponds to the Wave I case, while bottom profile corresponds to the Wave II case

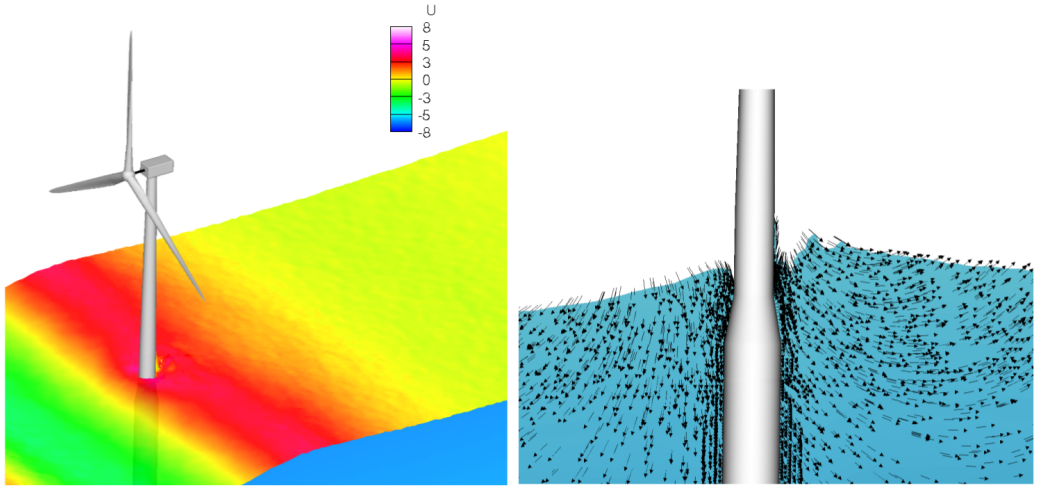

Figure 6.40: Left: Snapshot of the free surface colored by streamwise velocity (m/s). Right: Velocity vectors superposed on the water-domain current configuration. Plots correspond to Wave I conditions

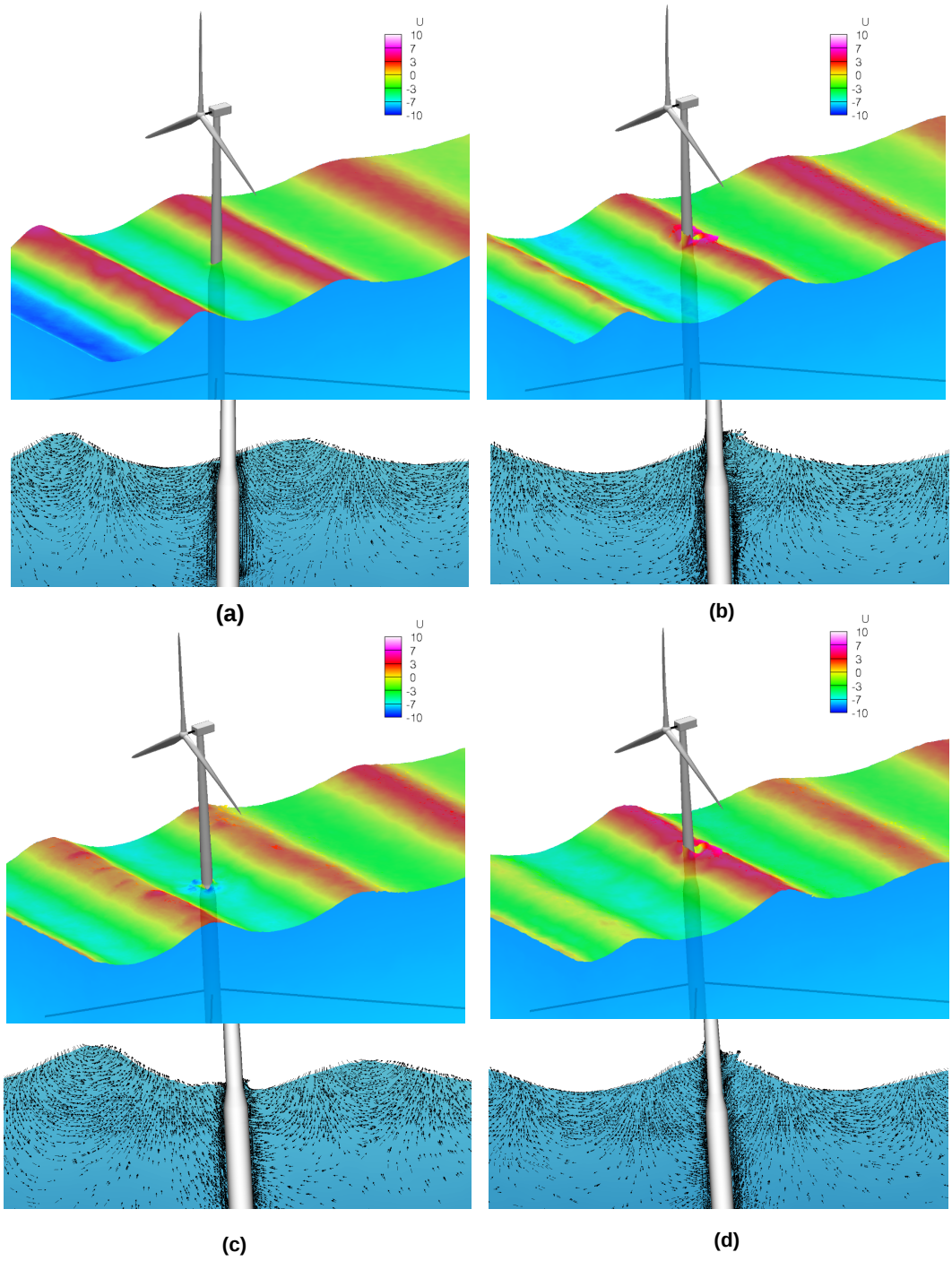

Figure 6.41: Snapshots of the free surface colored by streamwise velocity (m/s), and velocity vectors superposed on the water-domain current configuration at different times: (a) t = 0.4 s; (b) t = 6.73 s; (c) t = 10.35 s; and (d) t = 14.35 s. Plots correspond to Wave II conditions

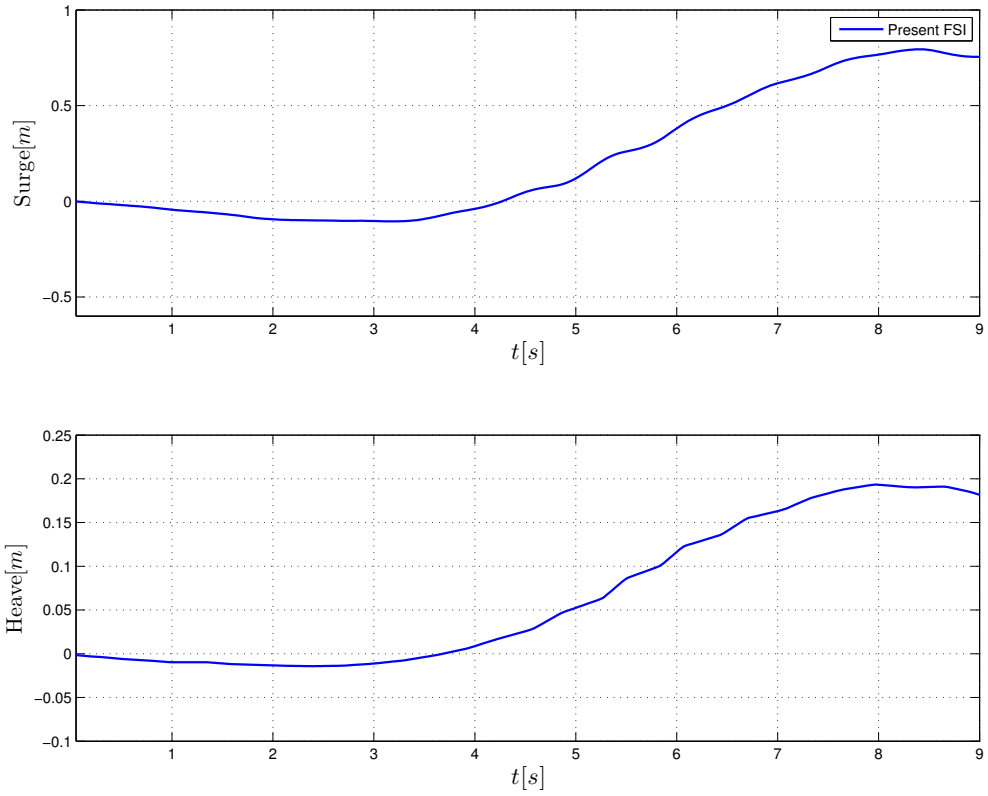

Figure 6.42: Displacements of center of mass of the platform under Water I

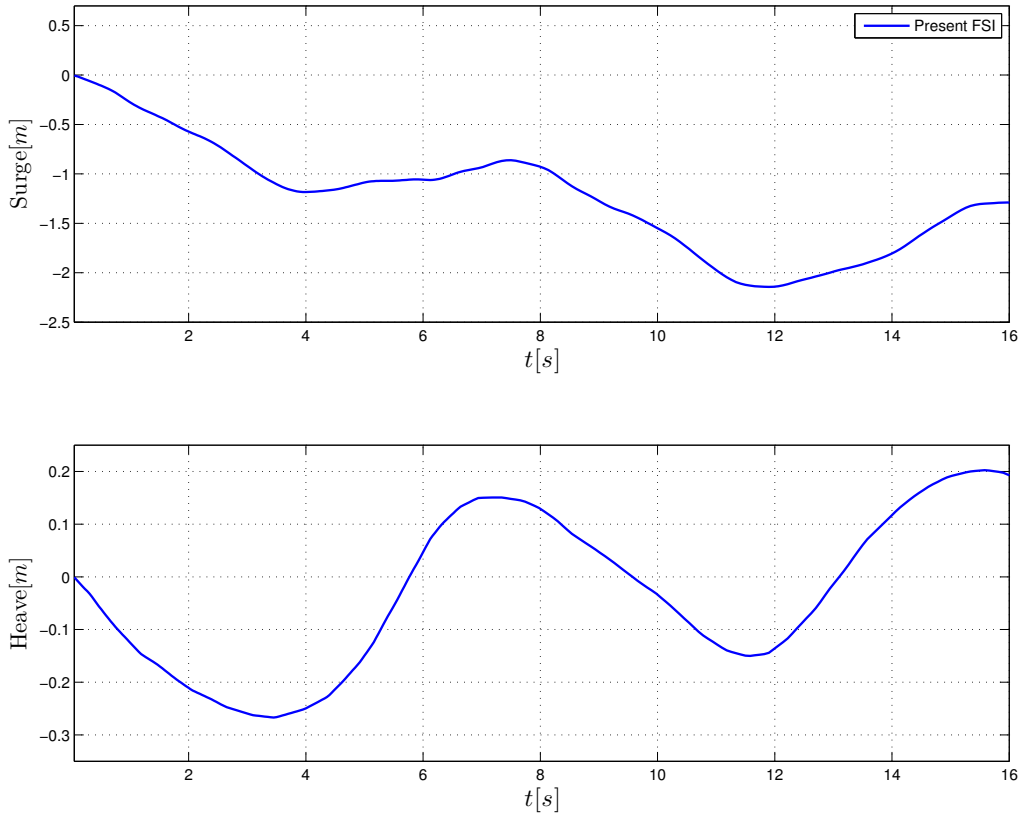

Figure 6.43: Displacements of center of mass of the platform under Water II

and wave height.

Two wave profiles at t = 10.8 s (Fig. 6.39 (top))and t = 36 s (Figure 6.39 (bottom)) are extracted from the wave tank simulation and used as the initial conditions for the floating wind turbine FSI simulations. The first profile (denoted by Wave I in what follows) is akin to a solitary wave with a height of about 10.2 m. The second profile (denoted by Wave II in what follows) consists of several peaks and troughs with a maximum wave height of 18.1 m. The wave profiles computed on the wave-tank mesh are transferred to the wind-turbine mesh to carry out the FSI simulations. The FSI-simulation mesh design follows that of the wave tank case, with the inserted wind turbine mesh (from the Airy-wave simulation presented earlier) and a refined region around. The total number of fluid nodes and elements in the FSI-simulation mesh are 2,600,630 and 15,163,124, respectively.

Figure 6.40 shows the wave surface colored by the stream-wise velocity for the Wave I case. The figure also shows a zoom on the region where the tower crosses the free surface and displays the velocity vectors in the water domain at a span-wise cut in the domain center to illustrate the hydrodynamic complexity simulated as the wave peak is passing the spar buoy. Figure 6.41 shows a series of similar snapshots for Wave II. Some splashing is observed in the case of Wave II, which also leads to a more pronounced structural response than Wave I.

Time histories of surge and heave displacements of the platform center of mass are plotted in Figure 6.42 for Wave I and Figure 6.43 Wave II. For Wave II, we also plot the time history of the blade tip displacement for all three blades in Figure 6.45 (See Figure 6.29 for blade numbering.) While the displacement time histories of blades 2 and 3 are very similar, and relatively low in magnitude, blade 1, whose tip is at the highest point on the wind-turbine structure (over 90 m higher than the tips of blades 2 and 3!), undergoes displacement with a more complex time history and much larger magnitude. The tip displacement time histories reveal the following behavior. When the first wave peak reaches the turbine, the spar buoy changes its direction of motion at a time instant of 3.7 s. The change in the direction of motion of the tips of blades 2 and 3 occurs at about 4.5 s, while blade 1 changes direction at about 4.8 s. This pattern repeats for other wave peaks, demonstrating the elasto-dynamic

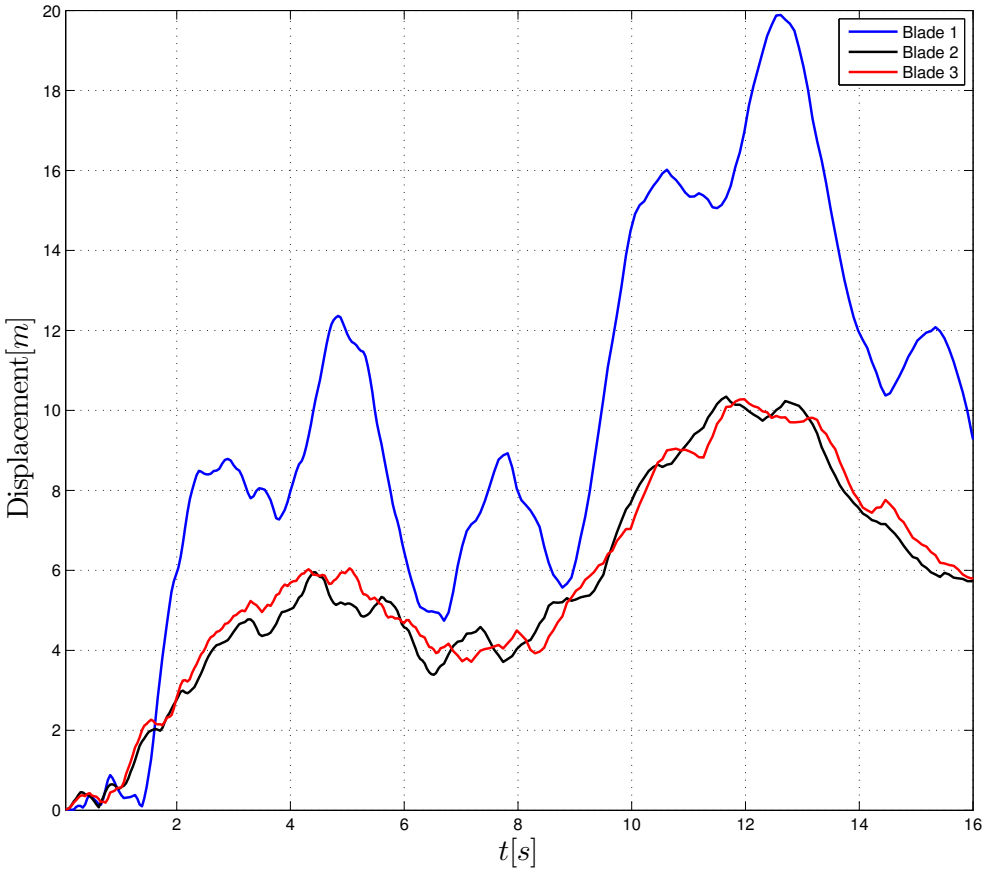

Figure 6.44: Absolute tip displacements of three blades under Water II (The beams and cables are not visualized)

effects. The floating wind turbine configuration at two different time instants for the Wave II case are visualized together in Figure 6.44 to better illustrate the structure range of motion.

6.3 Acknowledgement

This chapter, in part, is a reprint of the materials as they appear in : "Computational free-surface fluid-structure interaction with applications on offshore floating wind turbines" (with A. Korobenko, X. Deng, Y. Bazilevs) *Computers and Fluids*, 2016, " Experimental and numerical FSI study of compliant hydrofoils" (with B. Augier, A. Korobenko, J. Czarnowski,

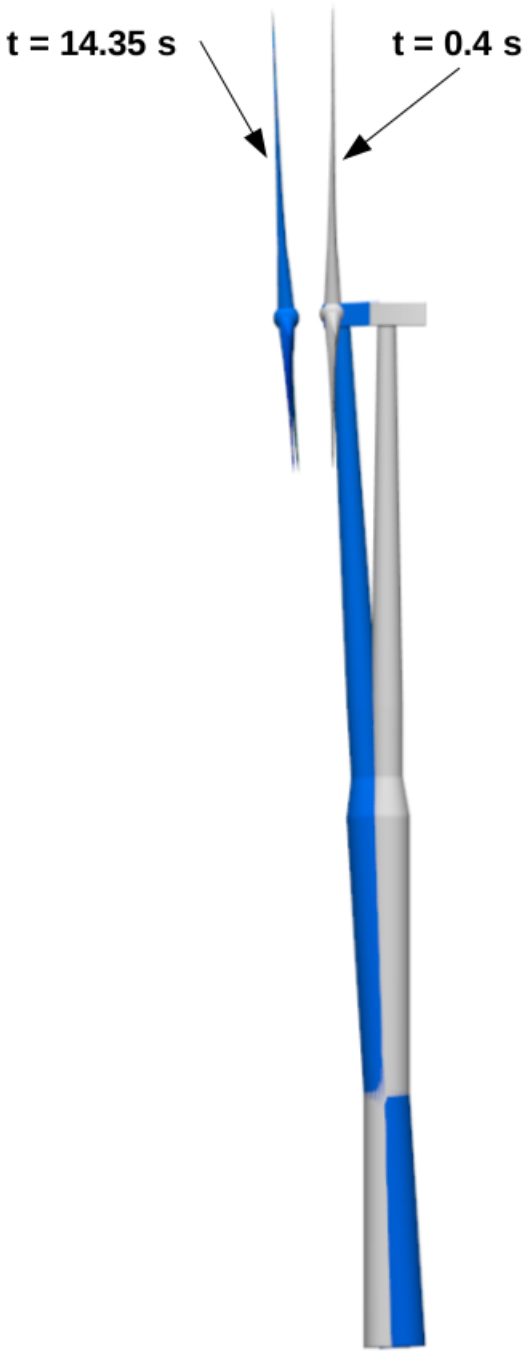

Figure 6.45: Snapshot of floating wind turbine configuration at different time under Water II

G. Ketterman, Y. Bazilevs) *Computational Mechanics*, 2016 and " FSI modeling of a propulsion system based on compliant hydrofoils in a tandem configuration" (with B. Augier, A. Korobenko, J. Czarnowski, G. Ketterman, Y. Bazilevs) *Computers and Fluids*, 2016. The dissertation author is the primary investigator and author of these papers.

Chapter 7

Conclusions

In this dissertation, a multi-scale, multi-physics free-surface fluid-structure interaction framework is developed. This framework proposes and integrates the most advanced computational free-surface FSI techniques. We utilize two-fluid Navier-Stokes equations and level-set method to track the evolution of air-water interface. The free-surface flows are solved by FEM-based ALE-VMS enhanced with weak enforcement of essential boundary conditions. Additional level set techniques including re-distancing and mass balancing are proposed. Sliding interface technique compatible with Navier-Stokes, level set convection and re-distancing is developed to handle the flow around objects in relative motion. Isogeometric rotation-free shell, beam/cable formulation is utilized to model the structures. To deal with the large added mass effect, quasi-direct coupling and flexible GMRES solver with matrix-free techniques are developed. Such framework enables 3D, time-dependent large scale free-surface FSI simulations. We apply the method on several challenging problems, namely, ocean wave modeling, offshore wind/tidal energy and bio-inspired engineering.

This work is a first step in the direction of using advanced free-surface FSI methods for the analysis of large scale marine structures in harsh environment. The free-surface FSI simulations performed in the paper make use of the most advanced representation of the geometry, materials, and mechanical phenomena than previously existed for the application considered, and present the state-of-the-art. We feel that the initial success of the proposed framework will pave the way for future advanced FSI modeling and simulation of large

scale structures, such as offshore floating wind turbines, tidal turbines and other naval architectures, in an effort to better understand the combined hydrodynamic and aerodynamic loading on these machines, and to improve their efficiency and survivability in often harsh environments.

Bibliography

[1] Sea generation, ltd. http://www.seageneration.co.uk/.

[2] Verdant power, inc. http://www.verdantpower.com/.

[3] I. Akkerman, Y. Bazilevs, D. J. Benson, M. W. Farthing, and C. E. Kees. Free-surface flow and fluid–object interaction modeling with emphasis on ship hydrodynamics. *Journal of Applied Mechanics*, 79:010905, 2012.

[4] I. Akkerman, Y. Bazilevs, C. E. Kees, and M. W. Farthing. Isogeometric analysis of free-surface flow. *Journal of Computational Physics*, 230:4137–4152, 2011.

[5] I. Akkerman, J. Dunaway, J. Kvandal, J. Spinks, and Y. Bazilevs. Toward free-surface modeling of planing vessels: simulation of the Fridsma hull using ALE-VMS. *Computational Mechanics*, 50:719–727, 2012.

[6] Douglas N Arnold, Franco Brezzi, Bernardo Cockburn, and L Donatella Marini. Unified analysis of discontinuous galerkin methods for elliptic problems. *SIAM journal on numerical analysis*, 39(5):1749–1779, 2002.

[7] B. Augier, J. Yan, A. Korobenko, J. Czarnowski, G. Ketterman, and Y. Bazilevs. Experimental and numerical FSI study of compliant hydrofoils. *Computational Mechanics*, 55:1079–1090, 2015.

[8] AS Bahaj, WMJ Batten, and G McCann. Experimental verifications of numerical predictions for the hydrodynamic performance of horizontal axis marine current turbines. *Renewable Energy*, 32(15):2479–2490, 2007.

[9] AS Bahaj, AF Molland, JR Chaplin, and WMJ Batten. Power and thrust measurements of marine current turbines under various hydrodynamic flow conditions in a cavitation tunnel and a towing tank. *Renewable energy*, 32(3):407–426, 2007.

[10] AS Bahaj and LE Myers. Fundamentals applicable to the utilisation of marine current turbines for energy production. *Renewable energy*, 28(14):2205–2211, 2003.

[11] X Bai, EJ Avital, A Munjiza, and JJR Williams. Numerical simulation of a marine current turbine in free surface flow. *Renewable Energy*, 63:715–723, 2014.

[12] J Baltazar and JAC Falcao De Campos. Hydrodynamic analysis of a horizontal axis marine current turbine with a boundary element method. *Journal of Offshore Mechanics and Arctic Engineering*, 133(4):041304, 2011.

[13] WMJ Batten, AS Bahaj, AF Molland, and JR Chaplin. Hydrodynamics of marine current turbines. *Renewable energy*, 31(2):249–256, 2006.

[14] WMJ Batten, AS Bahaj, AF Molland, and JR Chaplin. The prediction of the hydrodynamic performance of marine current turbines. *Renewable energy*, 33(5):1085–1096, 2008.

[15] WMJ Batten, AS Bahaj, AF Molland, JR Chaplin, Sustainable Energy Research Group, et al. Experimentally validated numerical method for the hydrodynamic design of horizontal axis tidal turbines. *Ocean Engineering*, 34(7):1013–1020, 2007.

[16] Y. Bazilevs and I. Akkerman. Large eddy simulation of turbulent Taylor–Couette flow using isogeometric analysis and the residual–based variational multiscale method. *Journal of Computational Physics*, 229:3402–3414, 2010.

[17] Y. Bazilevs, V. M. Calo, J. A. Cottrell, T. J. R. Hughes, A. Reali, and G. Scovazzi. Variational multiscale residual-based turbulence modeling for large eddy simulation of incompressible flows. *Computer Methods in Applied Mechanics and Engineering*, 197:173–201, 2007.

[18] Y. Bazilevs, V. M. Calo, T. J. R. Hughes, and Y. Zhang. Isogeometric fluid–structure interaction: theory, algorithms, and computations. *Computational Mechanics*, 43:3–37, 2008.

[19] Y. Bazilevs, V. M. Calo, Y. Zhang, and T. J. R. Hughes. Isogeometric fluid–structure interaction analysis with applications to arterial blood flow. *Computational Mechanics*, 38:310–322, 2006.

[20] Y Bazilevs, X Deng, A Korobenko, F Lanza di Scalea, MD Todd, and SG Taylor. Isogeometric fatigue damage prediction in large-scale composite structures driven by dynamic sensor data. *Journal of Applied Mechanics*, 82(9):091008, 2015.

[21] Y Bazilevs, X Deng, A Korobenko, F Lanza di Scalea, MD Todd, and SG Taylor. Isogeometric fatigue damage prediction in large-scale composite structures driven by dynamic sensor data. *Journal of Applied Mechanics*, 82(9):091008, 2015.

[22] Y. Bazilevs, J. R. Gohean, T. J. R. Hughes, R. D. Moser, and Y. Zhang. Patient-specific isogeometric fluid–structure interaction analysis of thoracic aortic blood flow due to implantation of the Jarvik 2000 left ventricular assist device. *Computer Methods in Applied Mechanics and Engineering*, 198:3534–3550, 2009.

[23] Y. Bazilevs, M.-C. Hsu, I. Akkerman, S. Wright, K. Takizawa, B. Henicke, T. Spielman, and T. E. Tezduyar. 3D simulation of wind turbine rotors at full scale. Part I:

Geometry modeling and aerodynamics. *International Journal for Numerical Methods in Fluids*, 65:207–235, 2011.

[24] Y Bazilevs, M-C Hsu, I Akkerman, S Wright, K Takizawa, B Henicke, T Spielman, and TE Tezduyar. 3d simulation of wind turbine rotors at full scale. part i: geometry modeling and aerodynamics. *International Journal for Numerical Methods in Fluids*, 65(1-3):207–235, 2011.

[25] Y. Bazilevs, M.-C. Hsu, D. Benson, S. Sankaran, and A. Marsden. Computational fluid–structure interaction: Methods and application to a total cavopulmonary connection. *Computational Mechanics*, 45:77–89, 2009.

[26] Y Bazilevs, M-C Hsu, J Kiendl, R Wüchner, and K-U Bletzinger. 3d simulation of wind turbine rotors at full scale. part ii: Fluid–structure interaction modeling with composite blades. *International Journal for Numerical Methods in Fluids*, 65(1-3):236–253, 2011.

[27] Y. Bazilevs, M.-C. Hsu, J. Kiendl, R. Wüchner, and Kai-Uwe Bletzinger. 3D simulation of wind turbine rotors at full scale. Part II: Fluid–structure interaction modeling with composite blades. *International Journal for Numerical Methods in Fluids*, 65:236–253, 2011.

[28] Y. Bazilevs, M.-C. Hsu, K. Takizawa, and T. E. Tezduyar. ALE-VMS and ST-VMS methods for computer modeling of wind-turbine rotor aerodynamics and fluid–structure interaction. *Mathematical Models and Methods in Applied Sciences*, 22(supp02):1230002, 2012.

[29] Y. Bazilevs, M.-C. Hsu, Y. Zhang, W. Wang, T. Kvamsdal, S. Hentschel, and J. Isaksen. Computational fluid–structure interaction: Methods and application to cerebral aneurysms. *Biomechanics and Modeling in Mechanobiology*, 9:481–498, 2010.

[30] Y. Bazilevs, M.-C. Hsu, Y. Zhang, W. Wang, X. Liang, T. Kvamsdal, R. Brekken, and J. Isaksen. A fully-coupled fluid–structure interaction simulation of cerebral aneurysms. *Computational Mechanics*, 46:3–16, 2010.

[31] Y. Bazilevs, Ming-Chen Hsu, and M. A. Scott. Isogeometric fluid–structure interaction analysis with emphasis on non-matching discretizations, and with application to wind turbines. *Computer Methods in Applied Mechanics and Engineering*, 249-252:28–41, 2012.

[32] Y. Bazilevs and T. J. R. Hughes. Weak imposition of Dirichlet boundary conditions in fluid mechanics. *Computers and Fluids*, 36:12–26, 2007.

[33] Y. Bazilevs and T. J. R. Hughes. NURBS-based isogeometric analysis for the computation of flows about rotating components. *Computational Mechanics*, 43:143–150, 2008.

[34] Y. Bazilevs, A Korobenko, X. Deng, and J. Yan. Novel structural modeling and mesh moving techniques for advanced FSI simulation of wind turbines. *International Journal for Numerical Methods in Engineering*, 102:766–783, 2015.

[35] Y Bazilevs, A Korobenko, X Deng, and J Yan. Fluid–structure interaction modeling for fatigue-damage prediction in full-scale wind-turbine blades. *Journal of Applied Mechanics*, 83(6):061010, 2016.

[36] Y. Bazilevs, A. Korobenko, X. Deng, J. Yan, M. Kinzel, and J. O. Dabiri. FSI modeling of vertical-axis wind turbines. *Journal of Applied Mechanics*, 81:081006, 2014.

[37] Y. Bazilevs, A. Korobenko, J. Yan, A. Pal, S. M. I. Gohari, and S. Sarkar. Ale–vms formulation for stratified turbulent incompressible flows with applications. *Mathematical Models and Methods in Applied Sciences*, 25:1540011, 2015.

[38] Y. Bazilevs, C. Michler, V. M. Calo, and T. J. R. Hughes. Isogeometric variational multiscale modeling of wall-bounded turbulent flows with weakly enforced boundary conditions on unstretched meshes. *Computer Methods in Applied Mechanics and Engineering*, 199:780–790, 2010.

[39] Y Bazilevs, C Michler, VM Calo, and TJR Hughes. Weak dirichlet boundary conditions for wall-bounded turbulent flows. *Computer Methods in Applied Mechanics and Engineering*, 196(49):4853–4862, 2007.

[40] Y. Bazilevs, K. Takizawa, and T. E. Tezduyar. *Computational fluid-structure interaction: Methods and applications*. Wiley, 2013.

[41] Y Bazilevs, J Yan, M de Stadler, and S Sarkar. Computation of the flow over a sphere at re= 3700: a comparison of uniform and turbulent inflow conditions. *Journal of Applied Mechanics*, 81(12):121003, 2014.

[42] Yuri Bazilevs, L Beirao da Veiga, J Austin Cottrell, Thomas JR Hughes, and Giancarlo Sangalli. Isogeometric analysis: approximation, stability and error estimates for h-refined meshes. *Mathematical Models and Methods in Applied Sciences*, 16(07):1031–1090, 2006.

[43] Yuri Bazilevs, Ming-Chen Hsu, Kenji Takizawa, and Tayfun E Tezduyar. Ale-vms and st-vms methods for computer modeling of wind-turbine rotor aerodynamics and fluid–structure interaction. *Mathematical Models and Methods in Applied Sciences*, 22(supp02):1230002, 2012.

[44] M. Behr, A. Johnson, J. Kennedy, S. Mittal, and T. Tezduyar. Computation of incompressible flows with implicit finite element implementations on the Connection Machine. *Computer Methods in Applied Mechanics and Engineering*, 108:99–118, 1993.

[45] M Behr and T Tezduyar. The shear-slip mesh update method. *Computer Methods in Applied Mechanics and Engineering*, 174(3):261–274, 1999.

[46] M. Behr and T. Tezduyar. Shear-slip mesh update in 3D computation of complex flow problems with rotating mechanical components. *Computer Methods in Applied Mechanics and Engineering*, 190:3189–3200, 2001.

[47] T. Belytschko, W. K. Liu, and B. Moran. *Nonlinear Finite Elements for Continua and Structures*. Wiley, 2000.

[48] J. Bennett. The effect of mass and web spacing on the loads and structural response of increasing wind turbine blade size. *MS Thesis, Royal Institute of Technology, Sweden*, 2012.

[49] Roger H Charlier. A sleeper awakes: tidal current power. *Renewable and Sustainable Energy Reviews*, 7(6):515–529, 2003.

[50] R. Chow and C.P. Dam. Verification of computational simulations of the NREL 5 MW rotor with a focus on inboard flow separation. *Wind Energy*, 15(8):967–981, 2012.

[51] J. Chung and G. M. Hulbert. A time integration algorithm for structural dynamics with improved numerical dissipation: The generalized-α method. *Journal of Applied Mechanics*, 60:371–75, 1993.

[52] J. A. Cottrell, T. J. R. Hughes, and Y. Bazilevs. *Isogeometric Analysis. Toward Integration of CAD and FEA*. Wiley, 2009.

[53] J. A. Cottrell, A. Reali, Y. Bazilevs, and T. J. R. Hughes. Isogeometric analysis of structural vibrations. *Computer Methods in Applied Mechanics and Engineering*, 195(41):5257–5296, 2006.

[54] John O Dabiri. Potential order-of-magnitude enhancement of wind farm power density via counter-rotating vertical-axis wind turbine arrays. *Journal of Renewable and Sustainable Energy*, 3(4):043104, 2011.

[55] X. Deng, A. Korobenko, J. Yan, and Y. Bazilevs. Isogeometric analysis of continuum damage in rotation-free composite shells. *Computer Methods in Applied Mechanics and Engineering*, 284:349–372, 2015.

[56] F.E. Fish. Performance constraints on the maneuverability of flexible and rigid biological systems. In *International Synposium on Unmanned Unthethered Submersible Technology*, pages 394–406. University of New Hampshire-Marine Systems, 1999.

[57] PL Fraenkel. Marine current turbines: pioneering the development of marine kinetic energy converters. *Proceedings of the Institution of Mechanical Engineers, Part A: Journal of Power and Energy*, 221(2):159–169, 2007.

[58] J. A. French. Wave uplift pressures on horizontal platforms. 1969.

[59] Roozbeh Golshan, Andrés E Tejada-Martínez, Mario Juha, and Yuri Bazilevs. Large-eddy simulation with near-wall modeling using weakly enforced no-slip boundary conditions. *Computers & Fluids*, 118:172–181, 2015.

[60] Jai N Goundar and M Rafiuddin Ahmed. Design of a horizontal axis tidal current turbine. *Applied Energy*, 111:161–174, 2013.

[61] D. T. Griffith and T. D. Ashwill. The Sandia 100-meter all-glass baseline wind turbine blade: SNL100-00. *Sandia Report SAND2011-3779*, 2011.

[62] Peter Hansbo and Joakim Hermansson. Nitsche's method for coupling non-matching meshes in fluid-structure vibration problems. *Computational Mechanics*, 32(1-2):134–139, 2003.

[63] Isaac Harari and Thomas JR Hughes. What are c and h?: Inequalities for the analysis and design of finite element methods. *Computer Methods in Applied Mechanics and Engineering*, 97(2):157–192, 1992.

[64] Magnus Rudolph Hestenes and Eduard Stiefel. Methods of conjugate gradients for solving linear systems. 1952.

[65] M. C. Homola, M. S. Virk, P. J. Nicklasson, and P. A. Sundsbø. Performance losses due to ice accretion for a 5 MW wind turbine. *Wind Energy*, 15(3):379–389, 2012.

[66] M.-C. Hsu, I. Akkerman, and Y. Bazilevs. High-performance computing of wind turbine aerodynamics using isogeometric analysis. *Computers & Fluids*, 49:93–100, 2011.

[67] M.-C. Hsu, I. Akkerman, and Y. Bazilevs. High-performance computing of wind turbine aerodynamics using isogeometric analysis. *Computers and Fluids*, 49:93–100, 2011.

[68] M.-C. Hsu, I. Akkerman, and Y. Bazilevs. Wind turbine aerodynamics using ALE–VMS: Validation and the role of weakly enforced boundary conditions. 50:499–511, 2012. doi:10.1007/s00466-012-0686-x.

[69] M.-C. Hsu, I. Akkerman, and Y. Bazilevs. Wind turbine aerodynamics using ALE-VMS: Validation and role of weakly enforced boundary conditions. *Computational Mechanics*, 50:499–511, 2012.

[70] M.-C. Hsu, I. Akkerman, and Y. Bazilevs. Finite element simulation of wind turbine aerodynamics: Validation study using NREL Phase VI experiment. *Wind Energy*, 17:461–481, 2014.

[71] M.-C. Hsu and Y. Bazilevs. Blood vessel tissue prestress modeling for vascular fluid–structure interaction simulations. *Finite Elements in Analysis and Design*, 47:593–599, 2011.

[72] M.-C. Hsu and Y. Bazilevs. Fluid–structure interaction modeling of wind turbines: Simulating the full machine. *Computational Mechanics*, 50:821–833, 2012.

[73] M.-C. Hsu and Y. Bazilevs. Fluid–structure interaction modeling of wind turbines: simulating the full machine. *Computational Mechanics*, 50:821–833, 2012.

[74] Ming-Chen Hsu, Ido Akkerman, and Yuri Bazilevs. Finite element simulation of wind turbine aerodynamics: validation study using nrel phase vi experiment. *Wind Energy*, 17(3):461–481, 2014.

[75] T. J. R. Hughes, J. A. Cottrell, and Y. Bazilevs. Isogeometric analysis: CAD, finite elements, NURBS, exact geometry, and mesh refinement. *Computer Methods in Applied Mechanics and Engineering*, 194:4135–4195, 2005.

[76] T. J. R. Hughes, W. K. Liu, and T. K. Zimmermann. Lagrangian–Eulerian finite element formulation for incompressible viscous flows. *Computer Methods in Applied Mechanics and Engineering*, 29:329–349, 1981.

[77] K. E. Jansen, C. H. Whiting, and G. M. Hulbert. A generalized-α method for integrating the filtered Navier–Stokes equations with a stabilized finite element method. *Computer Methods in Applied Mechanics and Engineering*, 190(3):305–319, 2000.

[78] A. A. Johnson and T. E. Tezduyar. Mesh update strategies in parallel finite element computations of flow problems with moving boundaries and interfaces. *Computer Methods in Applied Mechanics and Engineering*, 119:73–94, 1994.

[79] J. Jonkman, S. Butterfield, W. Musial, and G. Scott. Definition of a 5-MW reference wind turbine for offshore system development. Technical Report NREL/TP-500-38060, National Renewable Energy Laboratory, 2009.

[80] J. Jonkman and W. Musial. Offshore code comparison collaboration (OC3) for IEA task 23 offshore wind technology and deployment. *NREL Technical Report*, 2010.

[81] J. M. Jonkman. Dynamics of offshore floating wind turbines – model development and verification. *Wind Energy*, 12(5):459–492, 2009.

[82] J. M. Jonkman. *Definition of the Floating System for Phase IV of OC3*. National Renewable Energy Laboratory Golden, CO, USA, 2010.

[83] J.M. Jonkman and D. Matha. Dynamics of offshore floating wind turbines – analysis of three concepts. *Wind Energy*, 14(4):557–569, 2011.

[84] G. Karypis and V. Kumar. Multilevel k-way partioning scheme for irregular graphs. Technical Report 95-064, Department of Computer Science, University of Minnesota, 1995.

[85] G. Karypis and V. Kumar. A fast and high quality multilevel scheme for partitioning irregular graphs. *SIAM Journal of Scientific Computing*, 20:359–392, 1998.

[86] C. E. Kees, I. Akkerman, M. W. Farthing, and Y. Bazilevs. A conservative level set method suitable for variable-order approximations and unstructured meshes. *Journal of Computational Physics*, 230:4536–4558, 2011.

[87] MJ Khan, G Bhuyan, MT Iqbal, and JE Quaicoe. Hydrokinetic energy conversion systems and assessment of horizontal and vertical axis turbines for river and tidal applications: A technology status review. *Applied Energy*, 86(10):1823–1835, 2009.

[88] J. Kiendl, Y. Bazilevs, M.-C. Hsu, R. Wüchner, and Kai-Uwe Bletzinger. The bending strip method for isogeometric analysis of Kirchhoff–Love shell structures comprised of multiple patches. *Computer Methods in Applied Mechanics and Engineering*, 199:2403–2416, 2010.

[89] J. Kiendl, K.-U. Bletzinger, J. Linhard, and R. Wüchner. Isogeometric shell analysis with Kirchhoff–Love elements. *Computer Methods in Applied Mechanics and Engineering*, 198(49):3902–3914, 2009.

[90] Nitin Kolekar and Arindam Banerjee. Performance characterization and placement of a marine hydrokinetic turbine in a tidal channel under boundary proximity and blockage effects. *Applied Energy*, 148:121–133, 2015.

[91] Manoochehr M Koochesfahani. Vortical patterns in the wake of an oscillating airfoil. *AIAA journal*, 27(9):1200–1205, 1989.

[92] A. Korobenko, M.-C. Hsu, I. Akkerman, and Y. Bazilevs. Aerodynamic simulation of vertical-axis wind turbines. *Journal of Applied Mechanics*, 81(2), 021011, 2013.

[93] A. Korobenko, M.-C. Hsu, I. Akkerman, and Y. Bazilevs. Aerodynamic simulation of vertical-axis wind turbines. *Journal of Applied Mechanics*, 81:021011, 2013.

[94] A. Korobenko, M.-C. Hsu, I. Akkerman, J. Tippmann, and Y. Bazilevs. Structural mechanics modeling and FSI simulation of wind turbines. *Mathematical Models and Methods in Applied Sciences*, 23:249–272, 2013.

[95] A. Korobenko, M.C. Hsu, I. Akkerman, J. Tippmann, and Y. Bazilevs. Structural mechanics modeling and fsi simulation of wind turbines. *Mathematical Models and Methods in Applied Science*, 23:249–272, 2013.

[96] M. A. Lackner. An investigation of variable power collective pitch control for load mitigation of floating offshore wind turbines. *Wind Energy*, 16(4):519–528, 2013.

[97] M. A. Lackner and M. A. Rotea. Passive structural control of offshore wind turbines. *Wind energy*, 14(3):373–388, 2011.

[98] S.JC Lai and MF Platzer. Jet characteristics of a plunging airfoil. *AIAA journal*, 37(12):1529–1537, 1999.

[99] Michael J Lawson, Ye Li, and Danny C Sale. Development and verification of a computational fluid dynamics model of a horizontal-axis tidal current turbine. In *ASME 2011 30th International Conference on Ocean, Offshore and Arctic Engineering*, pages 711–720. American Society of Mechanical Engineers, 2011.

[100] Ju Hyun Lee, Sunho Park, Dong Hwan Kim, Shin Hyung Rhee, and Moon-Chan Kim. Computational methods for performance analysis of horizontal axis tidal stream turbines. *Applied Energy*, 98:512–523, 2012.

[101] A Leroyer and M Visonneau. Numerical methods for ranse simulations of a self-propelled fish-like body. *Journal of Fluids and Structures*, 20(7):975–991, 2005.

[102] Ye Li and Sander M Calisal. Three-dimensional effects and arm effects on modeling a vertical axis tidal current turbine. *Renewable energy*, 35(10):2325–2334, 2010.

[103] Pengfei Liu and Neil Bose. Prototyping a series of bi-directional horizontal axis tidal turbines for optimum energy conversion. *Applied Energy*, 99:50–66, 2012.

[104] C. C. Long, M.-C. Hsu, Y. Bazilevs, J. A. Feinstein, and A. L. Marsden. Fluid–structure interaction simulations of the Fontan procedure using variable wall properties. *International Journal for Numerical Methods in Biomedical Engineering*, 28:512–527, 2012.

[105] CC Long, M-C Hsu, Y Bazilevs, JA Feinstein, and AL Marsden. Fluid–structure interaction simulations of the fontan procedure using variable wall properties. *International journal for numerical methods in biomedical engineering*, 28(5):513–527, 2012.

[106] R Malki, AJ Williams, TN Croft, M Togneri, and I Masters. A coupled blade element momentum–computational fluid dynamics model for evaluating tidal stream turbine performance. *Applied Mathematical Modelling*, 37(5):3006–3020, 2013.

[107] A. L. Marsden, I. E. Vignon-Clementel, F. Chan, J. A. Feinstein, and C. A. Taylor. Effects of exercise and respiration on hemodynamic efficiency in CFD simulations of the total cavopulmonary connection. *Annals of Biomedical Engineering*, 35:250–263, 2007.

[108] Ian Masters, JC Chapman, MR Willis, and JAC Orme. A robust blade element momentum theory model for tidal stream turbines including tip and hub loss corrections. *Journal of Marine Engineering & Technology*, 10(1):25–35, 2011.

[109] M. E. McCormick. *Ocean engineering mechanics with applications*. Cambridge University Press, 2009.

[110] M. E. Moghadam, Y. Bazilevs, Tain-Yen Hsia, I. E. Vignon-Clementel, A. L. Marsden, and Modeling of Congenital Hearts Alliance (MOCHA). A comparison of outlet boundary treatments for prevention of backflow divergence with relevance to blood flow simulations. *Computational Mechanics*, 48:277–291, 2011.

[111] A.M. Mountcastle and T.L. Daniel. Aerodynamic and functional consequences of wing compliance. *Experiments in fluids*, 46(5):873–882, 2009.

[112] Joachim Nitsche. Über ein variationsprinzip zur lösung von dirichlet-problemen bei verwendung von teilräumen, die keinen randbedingungen unterworfen sind. In *Abhandlungen aus dem mathematischen Seminar der Universität Hamburg*, volume 36, pages 9–15. Springer, 1971.

[113] S. Osher and R. Fedkiw. *Level set methods and dynamic implicit surfaces*, volume 153. Springer Science and Business Media, 2006.

[114] S. Osher and J. A. Sethian. Fronts propagating with curvature-dependent speed: algorithms based on Hamilton-Jacobi formulations. *Journal of Computational Physics*, 79(1):12–49, 1988.

[115] S. B. Raknes, X. Deng, Y. Bazilevs, D.J. Benson, K.M. Mathisen, and T. Kvamsdal. Isogeometric rotation-free bending-stabilized cables: Statics, dynamics, bending strips and coupling with shells. *Computer Methods in Applied Mechanics and Engineering*, 263:127–143, 2013.

[116] Douglas A Read, FS Hover, and MS Triantafyllou. Forces on oscillating foils for propulsion and maneuvering. *Journal of Fluids and Structures*, 17(1):163–183, 2003.

[117] Fergal O Rourke, Fergal Boyle, and Anthony Reynolds. Tidal energy update 2009. *Applied Energy*, 87(2):398–409, 2010.

[118] Y. Saad and M. Schultz. GMRES: A generalized minimal residual algorithm for solving nonsymmetric linear systems. *SIAM Journal of Scientific and Statistical Computing*, 7:856–869, 1986.

[119] T. Sarpkaya and M. Isaacson. *Mechanics of wave forces on offshore structures*. van Nostrand Reinhold company, 1981.

[120] L. Schouveiler, FS Hover, and MS Triantafyllou. Performance of flapping foil propulsion. *Journal of Fluids and Structures*, 20(7):949–959, 2005.

[121] T. Sebastian and M.A. Lackner. Characterization of the unsteady aerodynamics of offshore floating wind turbines. *Wind Energy*, 16(3):339–352, 2013.

[122] W. Shyy, H. Aono, SK Chimakurthi, P. Trizila, C.K. Kang, CES Cesnik, and H. Liu. Recent progress in flapping wing aerodynamics and aeroelasticity. *Progress in Aerospace Sciences*, 46(7):284–327, 2010.

[123] K Stein, T Tezduyar, and R Benney. Mesh moving techniques for fluid-structure interactions with large displacements. *Journal of Applied Mechanics*, 70(1):58–63, 2003.

[124] Hiroshi Suito, Kenji Takizawa, Viet QH Huynh, Daniel Sze, and Takuya Ueda. Fsi analysis of the blood flow and geometrical characteristics in the thoracic aorta. *Computational Mechanics*, 54(4):1035–1045, 2014.

[125] K. Takizawa. Computational engineering analysis with the new-generation space–time methods. *Computational Mechanics*, 54:193–211, 2014.

[126] K. Takizawa. Computational engineering analysis with the new-generation space-time methods. *Computational Mechanics*, 2014.

[127] K. Takizawa, Y. Bazilevs, and T. E. Tezduyar. Space–time and ALE-VMS techniques for patient-specific cardiovascular fluid–structure interaction modeling. *Archives of Computational Methods in Engineering*, 19:171–225, 2012.

[128] K. Takizawa, B. Henicke, D. Montes, T. E. Tezduyar, M.-C. Hsu, and Y. Bazilevs. Numerical-performance studies for the stabilized space–time computation of wind-turbine rotor aerodynamics. *Computational Mechanics*, 48:647–657, 2011.

[129] K. Takizawa, B. Henicke, A. Puntel, N. Kostov, and T. E. Tezduyar. Computer modeling techniques for flapping-wing aerodynamics of a locust. *Computers & Fluids*, 85:125–134, 2013.

[130] K. Takizawa, B. Henicke, T. E. Tezduyar, M.-C. Hsu, and Y. Bazilevs. Stabilized space–time computation of wind-turbine rotor aerodynamics. *Computational Mechanics*, 48:333–344, 2011.

[131] K. Takizawa, D. Montes, M. Fritze, S. McIntyre, J. Boben, and T. E. Tezduyar. Methods for FSI modeling of spacecraft parachute dynamics and cover separation. *Mathematical Models and Methods in Applied Sciences*, 23:307–338, 2013.

[132] K. Takizawa, T. Spielman, and T. E. Tezduyar. Space–time FSI modeling and dynamical analysis of spacecraft parachutes and parachute clusters. *Computational Mechanics*, 48:345–364, 2011.

[133] K. Takizawa, H. Takagi, T. E. Tezduyar, and R. Torii. Estimation of element-based zero-stress state for arterial FSI computations. *Computational Mechanics*, 54:895–910, 2014.

[134] K. Takizawa and T. E. Tezduyar. Computational methods for parachute fluid–structure interactions. *Archives of Computational Methods in Engineering*, 19:125–169, 2012.

[135] K. Takizawa and T. E. Tezduyar. Space–time computation techniques with continuous representation in time (ST-C). *Computational Mechanics*, 53:91–99, 2014.

[136] K. Takizawa, T. E. Tezduyar, C. Boswell, R. Kolesar, and K. Montel. FSI modeling of the reefed stages and disreefing of the Orion spacecraft parachutes. *Computational Mechanics*, 54:1203–1220, 2014.

[137] K. Takizawa, T. E. Tezduyar, A Buscher, and S. Asada. Space–time fluid mechanics computation of heart valve models. *Computational Mechanics*, 54:973–986, 2014.

[138] K. Takizawa, T. E. Tezduyar, A Buscher, and S. Asada. Space–time interface-tracking with topology change (ST-TC). *Computational Mechanics*, 54:955–971, 2014.

[139] K. Takizawa, T. E. Tezduyar, R. Kolesar, C. Boswell, T. Kanai, and K. Montel. Multiscale methods for gore curvature calculations from FSI modeling of spacecraft parachutes. *Computational Mechanics*, 54:1461–1476, 2014.

[140] K. Takizawa, T. E. Tezduyar, and N. Kostov. Sequentially-coupled space–time FSI analysis of bio-inspired flapping-wing aerodynamics of an MAV. *Computational Mechanics*, 54:213–233, 2014.

[141] K. Takizawa, T. E. Tezduyar, T. Kuraishi, S. Tabata, and H. Takagi. Computational thermo-fluid analysis of a disk brake. *Computational Mechanics*, published online, DOI: 10.1007/s00466-016-1272-4, February 2016.

[142] K. Takizawa, T. E. Tezduyar, S. McIntyre, N. Kostov, R. Kolesar, and C. Habluetzel. Space–time VMS computation of wind-turbine rotor and tower aerodynamics. *Computational Mechanics*, 53:1–15, 2014.

[143] K. Takizawa, T. E. Tezduyar, H. Mochizuki, H. Hattori, S. Mei, L. Pan, and K. Montel. Space–time VMS method for flow computations with slip interfaces (ST-SI). *Mathematical Models and Methods in Applied Sciences*, 25:2377–2406, 2015.

[144] K. Takizawa, R. Torii, H. Takagi, T. E. Tezduyar, and X. Y. Xu. Coronary arterial dynamics computation with medical-image-based time-dependent anatomical models and element-based zero-stress state estimates. *Computational Mechanics*, 54:1047–1053, 2014.

[145] K. Takizawa, S. Wright, C. Moorman, and T. E. Tezduyar. Fluid–structure interaction modeling of parachute clusters. *International Journal for Numerical Methods in Fluids*, 65:286–307, 2011.

[146] Kenji Takizawa, Yuri Bazilevs, and Tayfun E Tezduyar. Space–time and ale-vms techniques for patient-specific cardiovascular fluid–structure interaction modeling. *Archives of Computational Methods in Engineering*, 19(2):171–225, 2012.

[147] Kenji Takizawa, Bradley Henicke, Darren Montes, Tayfun E Tezduyar, Ming-Chen Hsu, and Yuri Bazilevs. Numerical-performance studies for the stabilized space–time computation of wind-turbine rotor aerodynamics. *Computational Mechanics*, 48(6):647–657, 2011.

[148] Kenji Takizawa, Darren Montes, Matthew Fritze, Spenser McIntyre, Joseph Boben, and Tayfun E Tezduyar. Methods for fsi modeling of spacecraft parachute dynamics and cover separation. *Mathematical Models and Methods in Applied Sciences*, 23(02):307–338, 2013.

[149] T. Tezduyar, S. Aliabadi, M. Behr, A. Johnson, V. Kalro, and M. Litke. Flow simulation and high performance computing. *Computational Mechanics*, 18:397–412, 1996.

[150] T. E. Tezduyar. Finite element methods for flow problems with moving boundaries and interfaces. *Archives of Computational Methods in Engineering*, 8:83–130, 2001.

[151] T. E. Tezduyar. Interface-tracking, interface-capturing and enhanced solution techniques. In *Proceedings of the First South-American Congress on Computational Mechanics (CD-ROM)*, Santa Fe–Parana, Argentina, 2002.

[152] T. E. Tezduyar, M. Behr, S. Mittal, and A. A. Johnson. Computation of unsteady incompressible flows with the finite element methods – space–time formulations, iterative strategies and massively parallel implementations. In *New Methods in Transient Analysis*, PVP-Vol.246/AMD-Vol.143, pages 7–24, New York, 1992. ASME.

[153] T. E. Tezduyar and S. Sathe. Modeling of fluid–structure interactions with the space–time finite elements: Solution techniques. *International Journal for Numerical Methods in Fluids*, 54:855–900, 2007.

[154] T. E. Tezduyar, S. Sathe, R. Keedy, and K. Stein. Space–time techniques for finite element computation of flows with moving boundaries and interfaces. In S. Gallegos, I. Herrera, S. Botello, F. Zarate, and G. Ayala, editors, *Proceedings of the III International Congress on Numerical Methods in Engineering and Applied Science*. CD-ROM, Monterrey, Mexico, 2004.

[155] T. E. Tezduyar, S. Sathe, R. Keedy, and K. Stein. Space–time finite element techniques for computation of fluid–structure interactions. *Computer Methods in Applied Mechanics and Engineering*, 195:2002–2027, 2006.

[156] T. E. Tezduyar, K. Takizawa, T. Brummer, and P. R. Chen. Space–time fluid–structure interaction modeling of patient-specific cerebral aneurysms. *International Journal for Numerical Methods in Biomedical Engineering*, 27:1665–1710, 2011.

[157] Tayfun Tezduyar, Shahrouz Aliabadi, Marek Behr, Andrew Johnson, and Sanjay Mittal. Parallel finite-element computation of 3d flows. *Computer*, 26(10):27–36, 1993.

[158] Tayfun E Tezduyar and Sunil Sathe. Modelling of fluid–structure interactions with the space–time finite elements: solution techniques. *International Journal for Numerical Methods in Fluids*, 54(6-8):855–900, 2007.

[159] Tayfun E Tezduyar, Sunil Sathe, and Keith Stein. Solution techniques for the fully discretized equations in computation of fluid–structure interactions with the space–time formulations. *Computer Methods in Applied Mechanics and Engineering*, 195(41):5743–5753, 2006.

[160] R. Torii, M. Oshima, T. Kobayashi, K. Takagi, and T. E. Tezduyar. Computation of cardiovascular fluid–structure interactions with the DSD/SST method. In *Proceedings of the 6th World Congress on Computational Mechanics (CD-ROM)*, Beijing, China, 2004.

[161] Chenglong Wang, Michael CH Wu, Fei Xu, Ming-Chen Hsu, and Yuri Bazilevs. Modeling of a hydraulic arresting gear using fluid–structure interaction and isogeometric analysis. *Computers & Fluids*, 2015.

[162] Y. Wang, D. J. Benson, and A. P. Nagy. A multi-patch nonsingular isogeometric boundary element method using trimmed elements. *Computational Mechanics*, pages 1–19, 2015.

[163] Y. J. Wang and D. J. Benson. Multi-patch nonsingular isogeometric boundary element analysis in 3d. *Computer Methods in Applied Mechanics and Engineering*, 293:71–91, 2015.

[164] J. Yan, B. Augier, A. Korobenko, J. Czarnowski, G. Ketterman, and Y. Bazilevs. FSI modeling of a propulsion system based on compliant hydrofoils in a tandem configuration. *Computers and Fluids*, 2015. Published online. doi:10.1016/j.compfluid.2015.07.013.

[165] J Yan, Y Bazilevs, A Korobenko, A Tejada-Martinez, and R Golshan. A new multiscale residual-based turbulence modeling and les simulations of stratified flows. *Computers & Fluids*, 2016.

[166] J Yan, A Korobenko, X Deng, and Y Bazilevs. Computational free-surface fluid–structure interaction with application to floating offshore wind turbines. *Computers & Fluids*, 2016.

[167] Y. Zhang, Y. Bazilevs, S. Goswami, C. Bajaj, and T. J. R. Hughes. Patient-specific vascular nurbs modeling for isogeometric analysis of blood flow. *Computer Methods in Applied Mechanics and Engineering*, 196:2943–2959, 2007.

[168] Y. Zhang, W. Wang, X. Liang, Y. Bazilevs, M.-C. Hsu, T. Kvamsdal, R. Brekken, and J. Isaksen. High-fidelity tetrahedral mesh generation from medical imaging data for fluid-structure interaction analysis of cerebral aneurysms. *Computer Modeling in Engineering and Sciences*, 42:131–150, 2009.